8-2013

Analysis and Optimization of Unsteady Flow Past a Circular Cylinder Using a Harmonic Balance Method

Emily Buckman Clark
ebuckman@utk.edu

To the Graduate Council:

I am submitting herewith a thesis written by Emily Buckman Clark entitled "Analysis and Optimization of Unsteady Flow Past a Circular Cylinder Using a Harmonic Balance Method." I have examined the final electronic copy of this thesis for form and content and recommend that it be accepted in partial fulfillment of the requirements for the degree of Master of Science, with a major in Aerospace Engineering.

Kivanc Ekici, Major Professor

We have read this thesis and recommend its acceptance:

Rao V. Arimilli, Vasilios Alexiades

Accepted for the Council:
Carolyn R. Hodges

Vice Provost and Dean of the Graduate School

(Original signatures are on file with official student records.)

Analysis and Optimization of Unsteady Flow Past a Circular Cylinder Using a Harmonic Balance Method

A Thesis Presented for the
Master of Science
Degree
The University of Tennessee, Knoxville

Emily Buckman Clark
August 2013

Dedication

To my parents, who have always loved me and believed in my ability to succeed: Thank you for teaching me the value of hard work.

To my loving husband, John, for his unwavering support as my constant companion: May we have a lifetime of adventures together.

Acknowledgements

I would like to express the utmost gratitude to my advisor and mentor, Dr. Kivanc Ekici, who acknowledged my potential and encouraged me to pursue a graduate education. This work would not have been possible without his guidance. I would also like to thank Dr. Rao Arimilli and Dr. Vasilios Alexiades for not only acting as my committee members, but also for teaching the most valuable and challenging classes of my graduate education. Special thanks to Dr. Gary V. Smith, whose recommendation helped me discover the challenges and the rewards of teaching.

This work was partially supported by the National Science Foundation under Grant No: CBET-1150332. Additional support was provided by the Mechanical, Aerospace and Biomedical Engineering Department at the University of Tennessee, Knoxville, and by funds from the ASEE Summer Faculty Fellowship Program. Thanks again to Dr. Kivanc Ekici for giving me the opportunity to participate in the SFFP program. Thank you to Dr. Philip Beran for mentoring me during my stay at Wright Patterson Air Force Base. I would also like to thank Dr. Arnold Lumsdaine from Oak Ridge National Laboratory for his support in the last few months of my M.S. education. I would not be continuing my education as a Bredesen Center Fellow without his encouragement towards the pursuit of a doctorate degree.

Lastly, I would like to thank my closest friends and peers: Zeke Stannard, Michael Merriweather and Jordan Sawyer. Our time together has created memories that will never be forgotten.

Abstract

Two-dimensional laminar flow over a circular cylinder was investigated in this work. Three cases were considered in which the cylinder was either stationary, in constant rotation, or in periodic rotation. The purpose of this work was to investigate the effects of a rotating cylinder for lift enhancement, drag reduction, and the suppression of vortex shedding. The governing coupled nonlinear Navier-Stokes equations were solved using a finite difference discretization and Newton's method. In this way, three flow solvers were developed for this research: a steady solver, an unsteady time-accurate solver, and an unsteady harmonic balance solver. The force coefficients were of prime interest in this study. Favorable results were obtained using rotation as an active control for the flow over the cylinder. The cylinder in constant rotation resulted in lift enhancement, drag reduction and vortex suppression for increasing rotational speeds. Lift enhancement and drag reduction were also noted for a rotationally oscillating cylinder. The trade-offs for these goals were discussed. Lastly, a finite difference sensitivity analysis was performed for a rotationally oscillating cylinder with the harmonic balance solver. The mean drag coefficient was taken as the objective function, and the Strouhal number was the investigated design variable. The goal was to use the sensitivity analysis to determine a forcing frequency, which minimized the mean drag coefficient. Two iterative techniques were investigated, but neither converged to a minimum drag coefficient with the harmonic balance solver. It was determined that a minimum drag coefficient occurs near the boundary between the lock-on and non lock-on regions or in the non lock-on region, where the harmonic balance solver does not converge.

Table of Contents

List of Tables

List of Figures

Nomenclature

A_n, B_n	nth temporal Fourier coefficients
C_D	coefficient of drag
C_{DF}	drag component due to friction forces
C_{DP}	drag component due to pressure
C_{D0}	stationary mean drag coefficient
C_L	coefficient of lift
C_{LF}	lift component due to friction forces
C_{LP}	lift component due to pressure
d	diameter
D	drag force per unit cylinder length
D	pseudo-spectral operator
E,**E**$^{-1}$	discrete inverse Fourier and Fourier transformation matrices
f	transformed streamfunction
f_f	forcing frequency
f_0	natural vortex shedding frequency
F	friction force
FD	finite difference
HB	harmonic balance
I	identity matrix
k	pointer system index
L	lift force per unit cylinder length
N_H	number of harmonics
O	"order of"
P	pressure
r	radius, radial coordinate
R	relaxation factor
R^2	coefficient of determination
Re	Reynolds number

$\mathbf{S}$	streamfunction equation
St_d	Strouhal number
St_0	non-dimensional natural vortex shedding frequency
t	time
T	period
$\mathbf{u}$	local velocity vector
U_∞	free stream velocity
u_{rot}	imposed rotational speed on the cylinder
u_r, u_θ	polar velocities
$\mathbf{V}$	vorticity equation

α	steady flow rotational parameter
ϵ	small perturbation
η	radial transformation variable
θ	angular coordinate
$\dot{\theta}$	angular velocity
ν	kinematic viscosity
ξ	angular transformation variable
ρ	density
ψ	streamfunction
ω	vorticity
$\boldsymbol{\omega}^*$	vorticity at all sub-time levels
$\tilde{\boldsymbol{\omega}}$	Fourier coefficients for vorticity
Ω	unsteady flow rotational parameter

Chapter 1: Introduction

The flow around a bluff body is a common occurrence in the fields of science and engineering. Examples of such external flows include the flow past airplanes, automobiles and submarines or the wind flowing past buildings, bridges and wind turbines[1]. Vortex shedding occurs in the near wake behind a bluff body for flow past a critical Reynolds number and persists over a wide range of Reynolds numbers. As the Reynolds number increases, the vortices become more complex and turbulent[2]. The fluctuating forces associated with vortex shedding can cause structural vibrations and acoustic noise or resonance, which in some cases can lead to structural failure or enhanced mixing in the wake[3]. Thus, control of the vortex shedding is important for practical engineering applications. Many efforts have been made for controlling the wake behind a bluff body. Such works include passive and active controls including splitter plates, suboptimal blowing and suction, linear oscillations, and rotary oscillations[4]. In this work, rotation will be used as an active control for unsteady flow.

Flow past a circular cylinder has widely been accepted as the fundamental problem for understanding vortex dynamics and controlling vortex shedding in the bluff body wake. An understanding of the necessary strategies to control flows past rotating bluff bodies could be applied to many areas such as lift enhancement, drag reduction, and noise and vibration control[5]. In general, three flow regimes exist for the flow over a circular cylinder: the steady laminar regime, the unsteady laminar two-dimensional vortex shedding regime, and the unsteady regime where three-dimensional vortex structures are observed. The boundaries of these regions are well-known for the flow over a stationary cylinder. However, they are a function of the forcing parameters for rotating cylinders[6]. In the past, many investigators have studied the effect of rotation on a circular cylinder for both constant and periodic angular velocities. Much of the focus has been directed towards three main goals: suppression of vortex shedding, lift enhancement, and drag reduction. Ingham and Tang[7], and Badr, Dennis and Young[8] investigated the steady flow over a circular cylinder in constant rotation for low Reynolds numbers. They concluded that rotation will

delay and even prevent boundary layer separation. Steady flow solutions are not physical for higher Reynolds numbers as they cannot capture the unsteadiness of the flow field. Thus, unsteady flow over a rotating cylinder has been the focus of many research efforts. Badr et al.[8] studied the flow over a cylinder in constant rotation for Reynolds numbers of 60, 100, and 200. In these cases, the flow did not tend to a steady state, rather a periodic vortex shedding pattern developed. Kang et al.[3] studied fully developed vortex shedding for various Reynolds numbers. They determined a critical rotation rate beyond which vortex shedding is suppressed. Additionally, they showed favorable results concerning the goals of lift enhancement and drag reduction. According to their study, increasing rotation rates result in an increase of the mean lift coefficient and a decrease in the average drag coefficient. Mittal and Kumar[9] considered the flow past a spinning cylinder for a Reynolds number of 200. They investigated higher rotation rates than the critical value beyond which vortex shedding is suppressed. They found a small range of higher rotation rates for which stronger flow instabilities are experienced. After this small range, the flow becomes steady and vortex shedding ceases again. Mittal and Kumar[9] also saw successful lift enhancement and drag reduction. Very large lift coefficients were obtained for high rotation rates, while the mean drag coefficient was reduced beneath the stationary value for all investigated rotational speeds.

Rotary oscillation has also been considered as a route for flow control. Taneda[10] investigated the flow past a rotationally oscillating cylinder for a wide range of Reynolds numbers and forcing frequencies using flow visualization. The results showed complete vortex suppression for very high forcing frequencies. Tokumaru and Dimotakis[11] used flow visualization and wake profile measurements to examine the efficacy of forced rotary oscillations at a Reynolds number of 1.5×10^4, for the purpose of controlling the unsteady wake. They estimated a drag reduction by a factor of six beneath the stationary value. Shiels and Leonard[12] performed numerical simulations to investigate the experimental drag reduction seen by Tokumaru and Dimotakis[11]. Significant drag reduction was observed in this study, but it was determined that the mechanism for reduced drag was only effective at higher Reynolds numbers. Cheng et al.[13] performed numerical simulations

of flow past a rotationally oscillating cylinder for a Reynolds number of 200. They saw drag reduction beneath the stationary value for a wide range of frequencies in the non lock-on region. Baek and Sung[14] scrutinized the temporal behavior of vortex formation over a wide range of the forcing parameters. A lift enhancement was noted for various rotation speeds; it was determined that the maximum lift coefficient occurs at lower forcing frequencies for higher rotation rates. In another work, Choi et al.[4] studied the effects of rotary oscillation on the unsteady laminar flow past a cylinder. They investigated the flow field for various forcing frequencies and rotation rates to determine the boundary between the lock-on and non lock-on regions. They saw the greatest drag reduction near this boundary, and the amount of drag reduction was determined to be strongly Reynolds number dependent.

While there is a large body of work concerning the flow over a rotating cylinder, most of the previous works have used time-accurate methods for their solutions. The unsteady flow over a rotationally oscillating cylinder is temporally periodic when the vortex shedding frequency "locks-on" to the forcing frequency of oscillation. For such time-periodic problems the use of a harmonic balance method offers an efficient alternative to the time-accurate methods for the solution of the unsteady flow field. In the past, time-linearized and nonlinear time-accurate methods were used to model unsteady flows. The drawbacks of these methods resulted in a blend of time and frequency domain techniques[15]. Hall et al.[16] developed a harmonic balance method for temporally periodic flows. In this mixed time and frequency domain technique, one makes use of the temporal periodicity of the flow in order to solve the flow field at certain snapshots in time. These snapshots are represented by a number of sub-time levels that are equally spaced over one period. Rather than marching the solution from one physical time step to the next, all sub-time levels are computed simultaneously over a single period. The sub-time levels are coupled to each other through a pseudo-spectral operator, which is used to approximate the time derivative in the governing equations. There are many advantages associated with the harmonic balance method[17]. By using a pseudo-spectral operator, the problem can be treated as mathematically steady, and convergence acceleration techniques can be applied. Furthermore, a key advantage to the harmonic balance method is its reduced

computational cost. The computational cost of the harmonic balance approach was shown to scale nearly linearly with the number of sub-time levels used in the solution[15,17,18].

Two-dimensional laminar flow over a circular cylinder is investigated in this work. Three cases are considered in which the cylinder is either stationary, in constant rotation, or under periodic rotation. An unsteady time-accurate solver and an unsteady harmonic balance solver were developed to determine the effect of rotation on the lift enhancement, drag reduction, and suppression of vortex shedding. Lastly, a finite difference sensitivity analysis is performed for the rotationally oscillating cylinder with the goal of determining a value of the forcing frequency that reduces the mean drag coefficient.

Chapter 2: A Cylinder in Cross-Flow

2.1 Governing Equations

The flow around a circular cylinder was considered in this work. Three cases were analyzed in which the cylinder was either stationary, in steady rotation, or in unsteady rotation. The flow geometry is shown in Figure 1.

This fundamental problem is governed by the two-dimensional, incompressible, unsteady laminar Navier-Stokes equations, which can be written in the vorticity-streamfunction form given as

$$\nabla^2\psi = -\omega \tag{1}$$

$$\frac{\partial\omega}{\partial t} + \boldsymbol{u}\cdot\nabla\omega = \frac{1}{Re}\nabla^2\omega \tag{2}$$

where ω is the vorticity, ψ is the streamfunction, Re is the Reynolds number, and $\boldsymbol{u}$ is the local velocity vector. These equations can be conveniently expressed in polar coordinates such that

$$\frac{\partial^2\psi}{\partial r^2} + \frac{1}{r}\frac{\partial\psi}{\partial r} + \frac{1}{r^2}\frac{\partial^2\psi}{\partial\theta^2} = -\omega \tag{3}$$

$$\frac{\partial\omega}{\partial t} + u_r\frac{\partial\omega}{\partial r} + u_\theta\frac{1}{r}\frac{\partial\omega}{\partial\theta} = \frac{1}{Re}\left[\frac{\partial^2\omega}{\partial r^2} + \frac{1}{r}\frac{\partial\omega}{\partial r} + \frac{1}{r^2}\frac{\partial^2\omega}{\partial\theta^2}\right] \tag{4}$$

$$u_r = \frac{1}{r}\frac{\partial\psi}{\partial\theta}\ ,\ u_\theta = -\frac{\partial\psi}{\partial r} \tag{5}$$

where u_r and u_θ are the polar velocities.

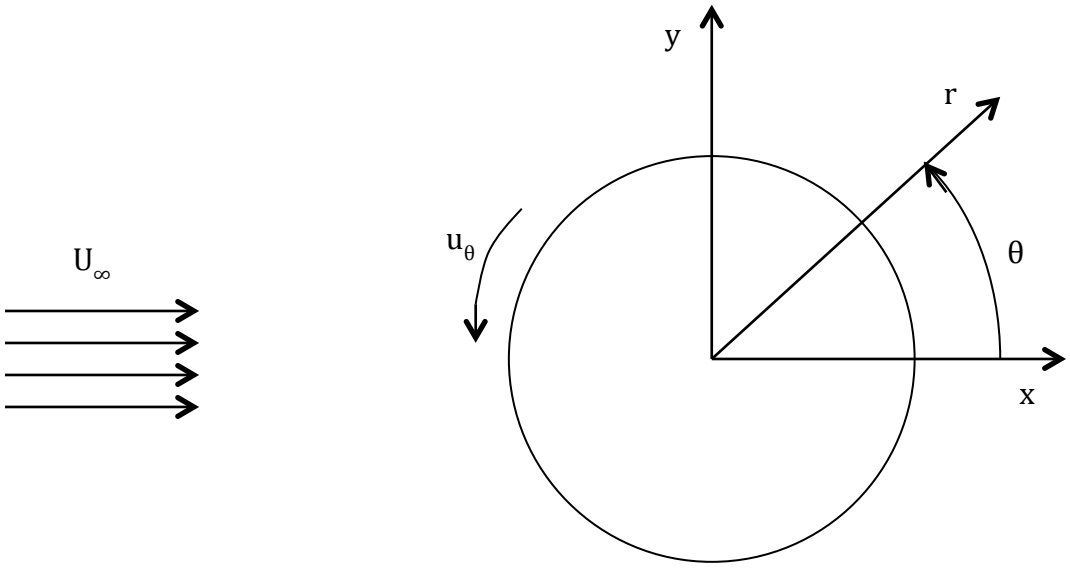

Figure 1: Flow geometry and polar coordinate system for a cylinder in cross-flow.

2.2 Coordinate Transformation

Following Ingham and Tang[7], a new dependent variable f is defined such that

$$\psi = rf + y = rf + r\sin\theta \tag{6}$$

which simplifies the specification of the boundary conditions.

The governing streamfunction equation can be modified with this new dependent variable by taking the appropriate partial derivatives. The first order partial derivatives are expressed by

$$\frac{\partial\psi}{\partial r} = \frac{\partial}{\partial r}(rf + r\sin\theta) = f + r\frac{\partial f}{\partial r} + \sin\theta \tag{7}$$

$$\frac{\partial\psi}{\partial\theta} = \frac{\partial}{\partial\theta}(rf + r\sin\theta) = r\frac{\partial f}{\partial\theta} + r\cos\theta \tag{8}$$

The second order derivatives are found in the same fashion to be

$$\frac{\partial^2 \psi}{\partial r^2} = 2\frac{\partial f}{\partial r} + r\frac{\partial^2 f}{\partial r^2} \tag{9}$$

$$\frac{\partial^2 \psi}{\partial \theta^2} = r\frac{\partial^2 f}{\partial \theta^2} - r\sin\theta \tag{10}$$

By substitution, the streamfunction equation becomes

$$r\frac{\partial^2 f}{\partial r^2} + 3\frac{\partial f}{\partial r} + \frac{1}{r}f + \frac{1}{r}\frac{\partial^2 f}{\partial \theta^2} = -\omega \tag{11}$$

In previous works, difficulties arose in the determination of the boundary condition at large distances[7]. Although many methods of approximating the far-field boundary condition had been proposed, it was not clear which approach was the most appropriate. A new technique was developed to avoid numerical errors by obtaining exact boundary conditions at infinity[7]. New independent variables, η and ξ, were introduced and were used to transform the original independent variables (θ and r) from the physical domain ($1 \le r \le \infty$, $0 \le \theta \le 2\pi$) to a computational domain ($0 \le \eta \le 1$, $0 \le \xi \le 1$). The initial physical domain is shown in Figure 2. In this domain, the radius is defined by the range $1 \le r \le \infty$, where the surface of the cylinder is located at $r=1$ and the far-field condition is at $r=\infty$. Similarly, the angle ranges from $0 \le \theta \le 2\pi$.

The new independent variables are taken to be

$$\begin{aligned} \eta &= \frac{1}{r},\ 0 \le \eta \le 1 \\ \xi &= \frac{\theta}{2\pi},\ 0 \le \xi \le 1 \end{aligned} \tag{12}$$

The physical domain is transformed into a finite rectangular region[7]. The computational grid is mapped from the surface of the cylinder to the far-field. As can be seen in Figure 3, the far-field is mapped to $\eta=0$ while the cylinder surface corresponds to $\eta=1$ whereas the periodic cuts are placed at $\xi=0$ and $\xi=1$. This mapping is beneficial as it allows the far-field

boundary condition to be placed at infinity (η=0). Additionally, the rectangular computational domain allows the governing equations to be discretized on a uniform grid using a finite difference scheme.

The new independent variables are used to complete the transformation of the governing equations. The use of the chain rule gives that

$$\frac{\partial f}{\partial r} = \frac{\partial f}{\partial \eta}\frac{\partial \eta}{\partial r} = -\frac{1}{r^2}\frac{\partial f}{\partial \eta} \tag{13}$$

$$\frac{\partial f}{\partial \theta} = \frac{\partial f}{\partial \xi}\frac{\partial \xi}{\partial \theta} = \frac{1}{2\pi}\frac{\partial f}{\partial \xi} \tag{14}$$

The higher order partial derivatives can be found in the same fashion, and substitution of these derivatives yields the following transformed Navier-Stokes equations

$$\eta^3 \frac{\partial^2 f}{\partial \eta^2} - \eta^2 \frac{\partial f}{\partial \eta} + \frac{\eta}{4\pi^2}\frac{\partial^2 f}{\partial \xi^2} + \eta f = -\omega \tag{15}$$

$$\begin{aligned} \frac{\partial \omega}{\partial t} - \eta^2\left(\frac{1}{2\pi}\frac{\partial f}{\partial \xi} + \cos(2\pi\xi)\right)\frac{\partial \omega}{\partial \eta} - \frac{\eta}{2\pi}\left(f - \eta\frac{\partial f}{\partial \eta} + \sin(2\pi\xi)\right)\frac{\partial \omega}{\partial \xi} \\ = \frac{1}{Re}\left(\eta^4\frac{\partial^2 \omega}{\partial \eta^2} + \eta^3\frac{\partial \omega}{\partial \eta} + \frac{\eta^2}{4\pi^2}\frac{\partial^2 \omega}{\partial \xi^2}\right) \end{aligned} \tag{16}$$

As can be seen, the resulting governing equations are coupled, and the vorticity equation has an unsteady term ($\frac{\partial \omega}{\partial t}$). The solution of these equations is traditionally simplified by lagging the nonlinear terms in the vorticity equation by a time step. This approach results in an explicit solution of the governing equations, which simplifies the time integration. However, when the nonlinear terms are lagged by a time step, the governing equations become uncoupled, and a very small time step is needed for an acceptable solution. Therefore, the coupled system is solved using an implicit approach in this work.

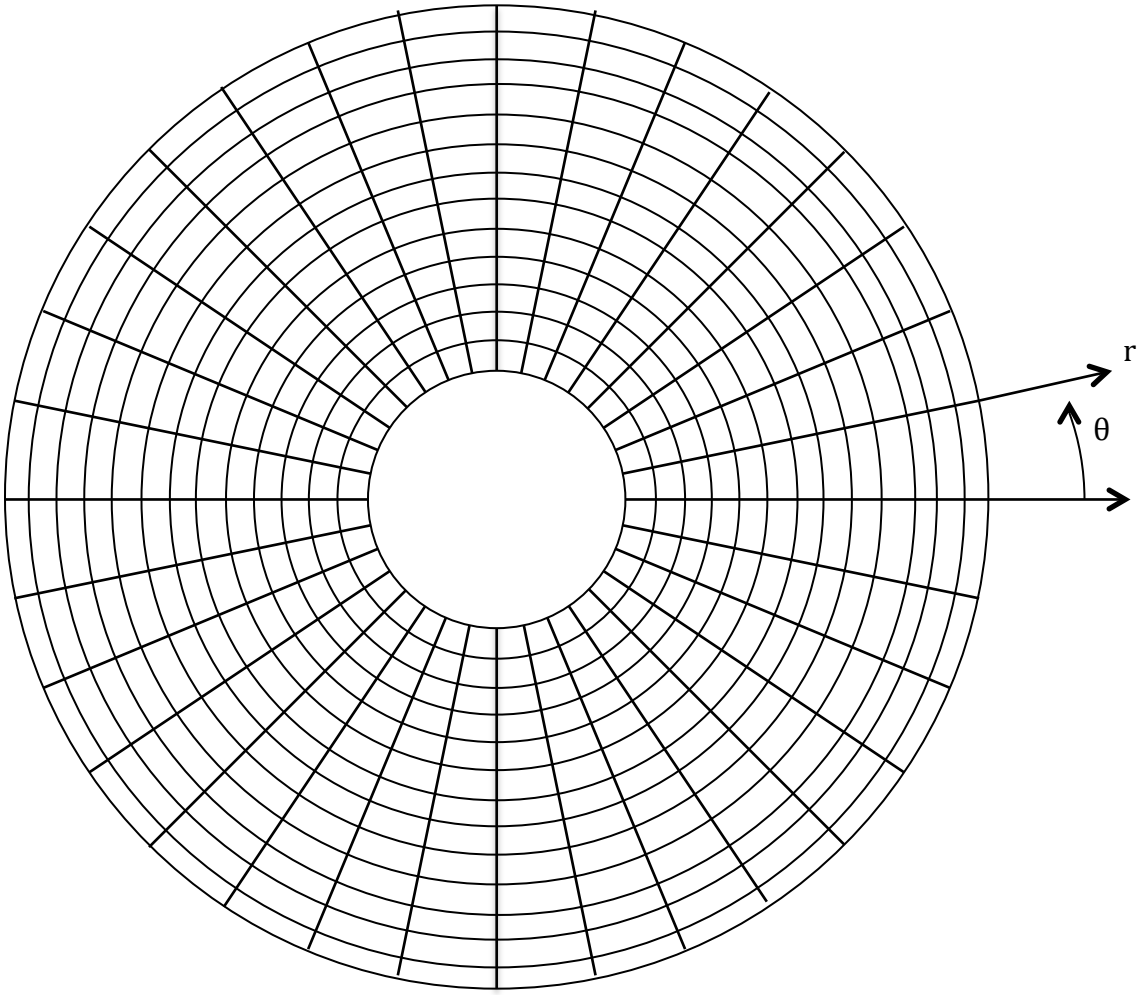

Figure 2: Initial physical domain in polar coordinates.

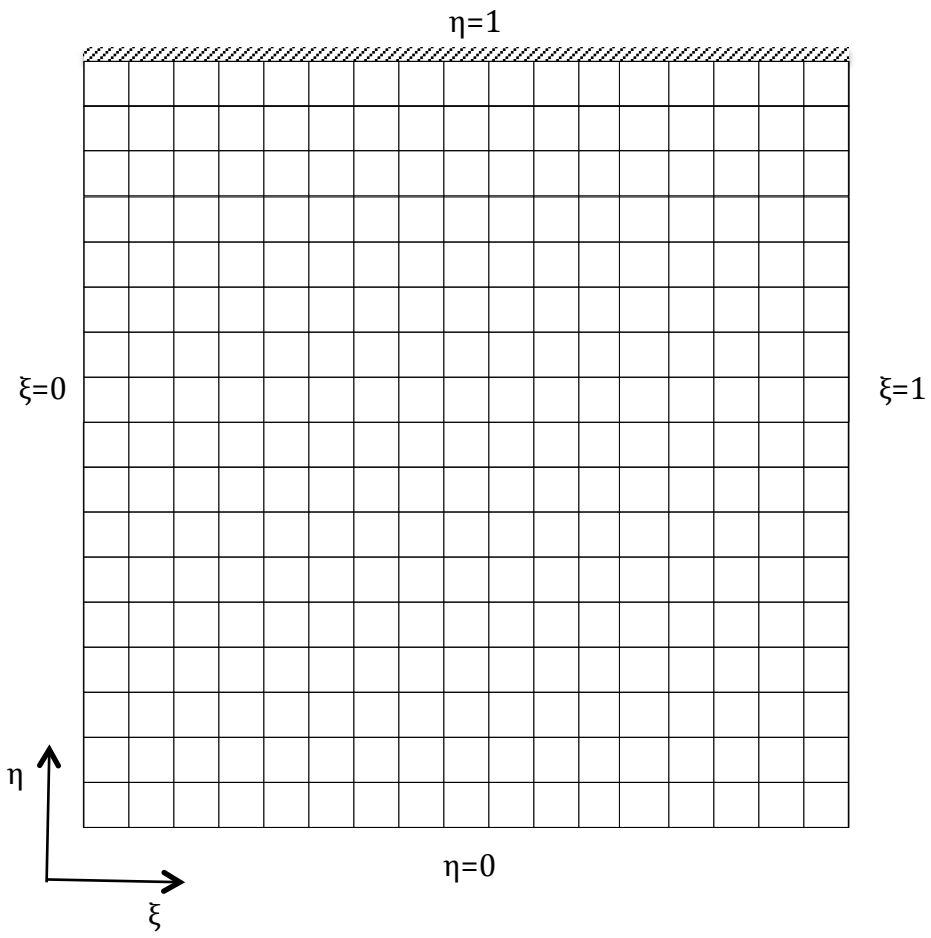

Figure 3: Resulting computational domain from coordinate transformation.

Chapter 3: Numerical Methods

3.1 Steady Cylinder

The transformed governing equations for the flow over a circular cylinder were presented in Section 2.2. As mentioned earlier, the vorticity equation (see Eq. (16)) includes an unsteady term, which is neglected for steady flow. This simplifies the discussion of the discretization and linearization of the governing equations. Thus, the steady flow over a cylinder will be considered for the development of the numerical method.

3.1.1 Discretization

The discretization of the governing equations was the initial step completed in the numerical method. The governing equations for flow over a circular cylinder are shown as Eq. (15) and (16). The steady process is resolved by the exclusion of the unsteady term in Eq. (16). The transformed equations were discretized on a uniform computational grid such as one shown in Figure 4.

The domain is defined by

$$\begin{aligned} \xi_{i,j} &= \Delta\xi \cdot (\mathrm{i} - 1),\ \mathrm{i} = 1{:}N \\ \eta_{i,j} &= \Delta\eta \cdot (j - 1),\ j = 1{:}M \end{aligned} \tag{17}$$

where N and M are the maximum number of points in the ξ and η directions, respectively. The spacings are determined according to the following relations

$$\begin{aligned} \Delta\xi &= \frac{1.0}{N-1} \\ \Delta\eta &= \frac{1.0}{M-1} \end{aligned} \tag{18}$$

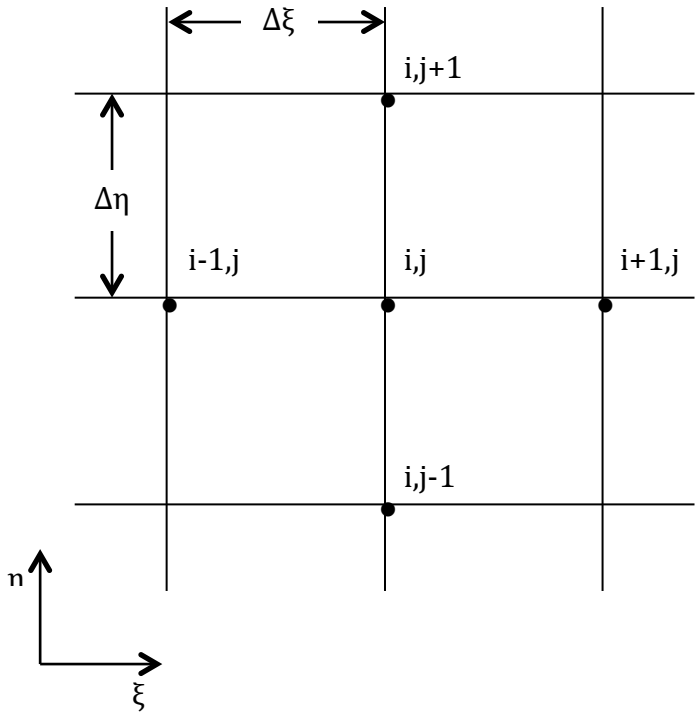

Figure 4: Uniform computational grid (Δη=Δξ).

A pointer system was adapted to simplify the discretization. The pointer system is shown in Figure 5. In this system, each (*i,j*) point from Fig. 4 is represented as *k*, and the surrounding points are given by

$$\begin{aligned} k_1 &= k + 1 \\ k_2 &= k + N \\ k_3 &= k - 1 \\ k_4 &= k - N \end{aligned} \tag{19}$$

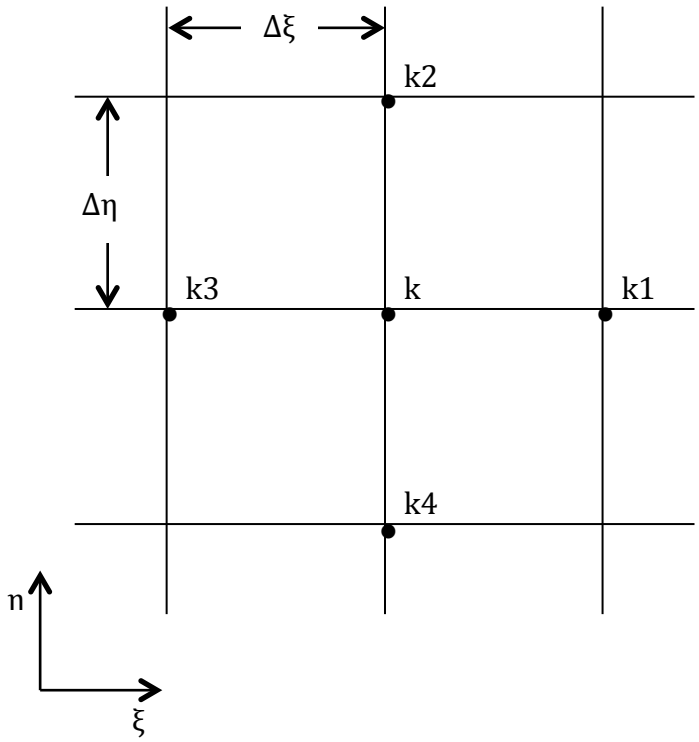

Figure 5: Pointer system for the computational domain.

The discretization was performed using second order central differences for the partial derivatives. The finite difference approximations for the derivatives are determined from a Taylor series approach. Hoffman[19] goes into great detail about this method. Consider a computational domain D(ξ) as shown in Figure 6. The domain is discretized with equally spaced points in the ξ direction using the adopted pointer system. The partial derivatives of the streamfunction and vorticity with respect to ξ can be derived from the Taylor series for a function of a single variable[19]. The finite difference approximations for the derivatives can be determined with linear combinations of the Taylor series for

appropriate points. The finite difference approximation for the second derivative of the streamfunction (f) with respect to ξ was found in the following manner.

Consider the computational domain in Fig. 6. Point k is chosen as the base point, and the Taylor series for f_{k1} and f_{k3} are written as follows

$$f_{k1} = f_k + \left.\frac{\partial f}{\partial \xi}\right|_k \Delta\xi + \left.\frac{\partial^2 f}{\partial \xi^2}\right|_k \frac{\Delta\xi^2}{2!} + \left.\frac{\partial^3 f}{\partial \xi^3}\right|_k \frac{\Delta\xi^3}{3!} + \cdots + \left.\frac{\partial^n f}{\partial \xi^n}\right|_k \frac{\Delta\xi^n}{n!} \tag{20}$$

$$f_{k3} = f_k - \left.\frac{\partial f}{\partial \xi}\right|_k \Delta\xi + \left.\frac{\partial^2 f}{\partial \xi^2}\right|_k \frac{\Delta\xi^2}{2!} - \left.\frac{\partial^3 f}{\partial \xi^3}\right|_k \frac{\Delta\xi^3}{3!} + \cdots + \left.\frac{\partial^n f}{\partial \xi^n}\right|_k \frac{\Delta\xi^n}{n!} \tag{21}$$

Adding Eq. (23) and (24) gives

$$f_{k1} + f_{k3} = 2f_k + \left.\frac{\partial^2 f}{\partial \xi^2}\right|_k \Delta\xi^2 + O(\Delta\xi^4) \tag{22}$$

Solving for the second derivative yields the second order central difference approximation

$$\left.\frac{\partial^2 f}{\partial \xi^2}\right|_k = \frac{f_{k1} - 2f_k + f_{k3}}{\Delta\xi^2} + O(\Delta\xi^2) \tag{23}$$

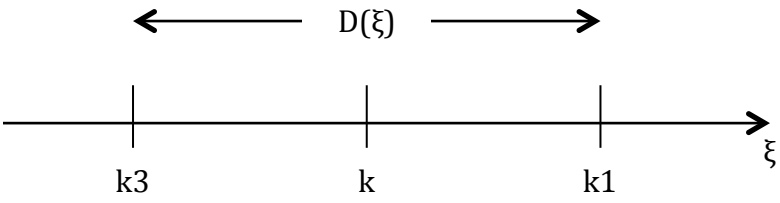

Figure 6: Computational domain D(ξ) with equally spaced points using the adopted pointer system.

The remaining derivatives in Eq. (16) and (17) can be found in a similar fashion. The resulting discretized governing equations are determined to be

$$\eta_k^3 \frac{f_{k2}-2f_k+f_{k4}}{\Delta\eta^2} - \eta_k^2 \frac{f_{k2}-f_{k4}}{2\Delta\eta} + \frac{\eta_k}{4\pi^2} \frac{f_{k1}-2f_k+f_{k3}}{\Delta\xi^2} + \eta_k f_k = -\omega_k \tag{24}$$

$$-\eta_k^2 \left(\frac{1}{2\pi} \frac{f_{k1}-f_{k3}}{2\Delta\xi} + \cos(2\pi\xi_k)\right) \frac{\omega_{k2}-\omega_{k4}}{2\Delta\eta} - \frac{\eta_k}{2\pi}\left(f_k - \eta_k \frac{f_{k2}-f_{k4}}{2\Delta\eta} + \sin(2\pi\xi_k)\right) \frac{\omega_{k1}-\omega_{k3}}{2\Delta\xi} \tag{25}$$
$$= \frac{1}{Re}\left(\eta_k^4 \frac{\omega_{k2}-2\omega_k+\omega_{k4}}{\Delta\eta^2} + \eta_k^3 \frac{\omega_{k2}-\omega_{k4}}{2\Delta\eta} + \frac{\eta_k^2}{4\pi^2} \frac{\omega_{k1}-2\omega_k+\omega_{k3}}{\Delta\xi^2}\right)$$

where ω_k, ω_{k1}, ω_{k2}, … , f_k, f_{k1}, f_{k2}, … are the dependent variables defined on the computational nodes. It should be noted that Eq. (24) and (25) are valid for the interior grid points. Boundary conditions must be applied to the boundary grid points. These conditions will be discussed in Section 3.1.3.

For convenience, let these equations be expressed as

$$\begin{aligned} \mathbf{S}(\boldsymbol{f}, \boldsymbol{\omega}) &= 0 \\ \mathbf{V}(\boldsymbol{f}, \boldsymbol{\omega}) &= 0 \end{aligned} \tag{26}$$

where **S** and **V** represent the streamfunction and vorticity equations in Eq. (24) and (25), respectively. Additionally, $\boldsymbol{f}$ and $\boldsymbol{\omega}$ represent the vectors of the dependent variables at all nodes of the computational domain. As one can see in Eq. (25), the discrete vorticity equation is nonlinear due to the products of dependent variables that appear through the expansion of the terms. The system of nonlinear equations given by Eq. (26) can be solved using Newton's method.

3.1.2 Newton's Method

Newton's method is a well-known iterative technique used for the solution of nonlinear equations. The method can be extended to systems of nonlinear equations[19]. Fornberg[20] discusses the advantages of using Newton's method for the steady cylinder. The convergence is quadratic and is guaranteed to occur for approximations "sufficiently close" to an isolated solution. The quadratic convergence eliminates the possibility of physical instabilities being carried over through the iterations. However, a linear system must be solved for each iteration, and this results in increased computational cost[20].

The equations in the governing nonlinear system (Eq. (26)) are linearized using a small perturbation assumption; the result is a linear system composed of the Jacobian matrix, the known right-hand sides, and the unknown changes in the functions of interest. For the steady solver, the linear system is iterated on until the changes in the transformed streamfunction and vorticity are within the given tolerance.

The linearization is performed using the following perturbation assumption

$$\begin{aligned} f_k^{n+1} &= f_k^n + \delta f_k \\ \omega_k^{n+1} &= \omega_k^n + \delta \omega_k \end{aligned} \tag{27}$$

Eq. (27) was substituted into Eq. (24) to give the linearized streamfunction

$$\begin{aligned} &\eta_k^3 \frac{\delta f_{k2} - 2\delta f_k + \delta f_{k4}}{\Delta\eta^2} - \eta_k^2 \frac{\delta f_{k2} - \delta f_{k4}}{2\Delta\eta} + \frac{\eta_k}{4\pi^2} \frac{\delta f_{k1} - 2\delta f_k + \delta f_{k3}}{\Delta\xi^2} + \eta_k \delta f_k + \delta\omega_k \\ &= -\eta_k^3 \frac{f_{k2}^n - 2f_k^n + f_{k4}^n}{\Delta\eta^2} + \eta_k^2 \frac{f_{k2}^n - f_{k4}^n}{2\Delta\eta} - \frac{\eta_k}{4\pi^2} \frac{f_{k1}^n - 2f_k^n + f_{k3}^n}{\Delta\xi^2} - \eta_k f_k^n - \omega_k^n \end{aligned} \tag{28}$$

The vorticity equation was linearized in the same fashion. The resulting unknowns from the linearization are the changes in the dependent variables ($\delta f_k, \delta f_{k1}, \cdots, \delta\omega_k, \delta\omega_{k1}, \cdots$), and the resulting known values are the streamfunction and vorticity from the previous iteration ($f_k^n, f_{k1}^n, \cdots, \omega_k^n, \omega_{k1}^n, \cdots$). If the unknown terms are collected, the linearized governing equations become

$$\left(-\frac{2\eta_k^3}{\Delta\eta^2}-\frac{2\eta_k}{4\pi^2\Delta\xi^2}+\eta_k\right)\delta f_k+\left(\frac{\eta_k}{4\pi^2\Delta\xi^2}\right)\delta f_{k1}+\left(\frac{\eta_k^3}{\Delta\eta^2}-\frac{\eta_k^2}{2\Delta\eta}\right)\delta f_{k2}+\left(\frac{\eta_k}{4\pi^2\Delta\xi^2}\right)\delta f_{k3} \tag{29}$$
$$+\left(\frac{\eta_k^3}{\Delta\eta^2}+\frac{\eta_k^2}{2\Delta\eta}\right)\delta f_{k4}+\delta\omega_k=-\eta_k^3\frac{f_{k2}^n-2f_k^n+f_{k4}^n}{\Delta\eta^2}$$
$$+\eta_k^2\frac{f_{k2}^n-f_{k4}^n}{2\Delta\eta}-\frac{\eta_k}{4\pi^2}\frac{f_{k1}^n-2f_k^n+f_{k3}^n}{\Delta\xi^2}-\eta_k f_k^n-\omega_k^n$$

$$\left(-\frac{\eta_k}{2\pi}\frac{\omega_{k1}^n-\omega_{k3}^n}{2\Delta\xi}\right)\delta f_k+\left(-\frac{\eta_k^2}{4\pi\Delta\xi}\frac{\omega_{k2}^n-\omega_{k4}^n}{2\Delta\eta}\right)\delta f_{k1}+\cdots+\left[\frac{2}{Re}\left(\frac{\eta_k^4}{\Delta\eta^2}+\frac{\eta_k^2}{4\pi^2\Delta\xi^2}\right)\right]\delta\omega_k \tag{30}$$
$$+\left[-\frac{\eta_k}{4\pi\Delta\xi}\left(f_k^n-\eta_k\frac{f_{k2}^n-f_{k4}^n}{2\Delta\eta}+\sin(2\pi\xi_k)\right)-\frac{\eta_k^2}{4\pi^2\Delta\xi^2Re}\right]\delta\omega_{k1}+\cdots$$
$$=\frac{\eta_k}{2\pi}\left(f_k^n-\eta_k\frac{f_{k2}^n-f_{k4}^n}{2\Delta\eta}+\sin(2\pi\xi_k)\right)\frac{\omega_{k1}^n-\omega_{k3}^n}{2\Delta\xi}+\eta_k^2\left(\frac{1}{2\pi}\frac{f_{k1}^n-f_{k3}^n}{2\Delta\xi}+\cos(2\pi\xi_k)\right)\frac{\omega_{k2}^n-\omega_{k4}^n}{2\Delta\eta}$$
$$+\frac{1}{Re}\left(\eta_k^4\frac{\omega_{k2}^n-2\omega_k^n+\omega_{k4}^n}{\Delta\eta^2}+\eta_k^3\frac{\omega_{k2}^n-\omega_{k4}^n}{2\Delta\eta}+\frac{\eta_k^2}{4\pi^2}\frac{\omega_{k1}^n-2\omega_k^n+\omega_{k3}^n}{\Delta\xi^2}\right)$$

Using the convenient form represented by Eq. (26), the discrete linearized governing equations can be represented as a system of linear equations given as

$$\begin{bmatrix}\frac{\partial\mathbf{S}}{\partial\boldsymbol{f}} & \frac{\partial\mathbf{S}}{\partial\boldsymbol{\omega}}\\ \frac{\partial\mathbf{V}}{\partial\boldsymbol{f}} & \frac{\partial\mathbf{V}}{\partial\boldsymbol{\omega}}\end{bmatrix}_n\begin{bmatrix}\Delta\boldsymbol{f}\\ \Delta\boldsymbol{\omega}\end{bmatrix}=\begin{bmatrix}-\mathbf{S}\\ -\mathbf{V}\end{bmatrix}_n \tag{31}$$

where $\Delta\boldsymbol{f}$ and $\Delta\boldsymbol{\omega}$ are the changes of the streamfunction and vorticity that are used to update the solution such that

$$\begin{aligned}\boldsymbol{f}^{n+1}&=\boldsymbol{f}^n+\Delta\boldsymbol{f}\\ \boldsymbol{\omega}^{n+1}&=\boldsymbol{\omega}^n+\Delta\boldsymbol{\omega}\end{aligned} \tag{32}$$

Note that the coefficient matrix in Eq. (31) is the Jacobian arising from Newton's method and that the unknowns in the linear system are the changes in the streamfunction and vorticity. The solution of the linear system in Eq. (31) results in a very large, sparse matrix. Iterative methods are generally preferred for this type of system because they do not

require that the Jacobian matrix be built and stored. However, basic iterative methods require diagonal dominance for guaranteed convergence, and the sparse system resulting from Eq. (31) is not diagonally dominant. Therefore, for simplicity, the linear system was solved using a direct method in this work. The use of direct methods requires the storage of the very large Jacobian matrix, which significantly increases the computational cost.

3.1.3 Boundary Conditions and Force Coefficients

The numerical solution of flow over a circular cylinder is dependent on the boundary conditions chosen[7,20,21]. Fornberg[20] recognized the "extreme sensitivity of the final solution to small errors in these conditions." Many previous investigators elected to use the Oseen approximation for boundary conditions at large distances from the cylinder[8]. Fornberg[21] showed that even for a symmetrical flow, the Oseen boundary condition can only be expected to be accurate at very small Reynolds numbers. Because of the dependency on the boundary conditions, a new numerical technique was developed to avoid the problems with satisfying the boundary conditions at large distances[7]. This technique required the coordinate transformation discussed in Section 2.2. The boundary conditions are applied in the computational domain defined by (ξ, η). Conditions for the streamfunction and vorticity are applied at the surface of the cylinder and at the far-field, η=1 and η=0, respectively. Additionally, there are periodic boundary conditions at the cut in the physical grid (ξ=0, ξ=1), which must be taken into consideration.

Streamfunction Boundary Conditions

There are two conditions on the cylinder surface (η=1) for the streamfunction.

$$\psi = 0 \tag{33}$$

$$\frac{\partial \psi}{\partial r} = -u_\theta = -u_{rot} \tag{34}$$

Eq. (33) represents the assumption that the streamfunction is zero on the surface, and Eq. (34) is a no-slip condition in which the rotational component of the velocity matches the rotational speed of the cylinder.

Inserting the transformation variables given by Eq. (12) into Eq. (6) yields

$$\psi = \frac{f+\sin(2\pi\xi)}{\eta} \tag{35}$$

or

$$f = \psi\eta - \sin(2\pi\xi) \tag{36}$$

Substituting the first surface condition into Eq. (36) yields the transformed streamfunction at the surface

$$f(\xi, 1) = -\sin(2\pi\xi) \tag{37}$$

The no-slip condition can be transformed to the new variables in the following manner. First, the partial derivative of the streamfunction with respect to the radial direction can be determined by substituting Eq. (12) and (13) into Eq. (7), which yields

$$\frac{\partial\psi}{\partial r} = f - \eta\frac{\partial f}{\partial\eta} + \sin(2\pi\xi) \tag{38}$$

The transformed no-slip condition is then determined to be

$$u_{rot} = u_\theta = -\left(f - \eta\frac{\partial f}{\partial\eta} + \sin(2\pi\xi)\right) \tag{39}$$

Noting that η=1 at the surface and rearranging Eq. (39) gives

$$u_{rot} = -(f(\xi, 1) + \sin(2\pi\xi)) + \left.\frac{\partial f}{\partial\eta}\right|_{\eta=1} \tag{40}$$

Making use of the transformed streamfunction surface condition, the rotation speed becomes

$$u_{rot} = \left.\frac{\partial f}{\partial \eta}\right|_{\eta=1} \tag{41}$$

This fact will be revisited in the determination of the surface vorticity condition.

The condition for the streamfunction at the far-field can be determined in a similar way[7]. Revisiting Eq. (6) and rearranging for the transformed streamfunction gives

$$f = \frac{\psi - y}{r} = \eta(\psi - y) \tag{42}$$

At infinity (η=0), the condition for the transformed streamfunction at the far-field becomes

$$f(\xi, 0) = 0 \tag{43}$$

This approach matches the boundary conditions mentioned in viscous flow literature[2].

Vorticity Boundary Conditions

It has been suggested that the choice of a boundary condition for the vorticity is not as sensitive as the condition for the streamfunction[7]. Filon[22] showed that the vorticity at large distances from the cylinder was approximately zero. This results in a far-field boundary condition for the vorticity such that

$$\omega(\xi, 0) = 0 \tag{44}$$

It is equally necessary to specify the vorticity at the surface of the cylinder. Consider the transformed streamfunction given by Eq. (15) at the cylinder surface (η=1)

$$\left.\frac{\partial^2 f}{\partial \eta^2}\right|_{\eta=1} - \left.\frac{\partial f}{\partial \eta}\right|_{\eta=1} + \frac{1}{4\pi^2}\left.\frac{\partial^2 f}{\partial \xi^2}\right|_{\eta=1} + f(\xi,1) = -\omega(\xi,1) \tag{45}$$

Using the surface streamfunction condition given by Eq. (37), the second order partial derivative with respect to ξ is determined to be

$$\left.\frac{\partial^2 f}{\partial \xi^2}\right|_{\eta=1} = 4\pi^2 \sin(2\pi\xi) \tag{46}$$

Substituting this derivative into Eq. (45) along with algebraic simplifications yields

$$\left.\frac{\partial^2 f}{\partial \eta^2}\right|_{\eta=1} - \left.\frac{\partial f}{\partial \eta}\right|_{\eta=1} = -\omega(\xi,1) \tag{47}$$

The second derivative in Eq. (45) was approximated using second order one-sided finite differences. The finite difference equations can be determined using the Taylor series approach once again. Consider the computational domain shown in Figure 7. The base point is f_0 or (ξ,1), and the Taylor series can be written for the other points as follows

$$f_1 = f_0 - \left.\frac{\partial f}{\partial \eta}\right|_0 \Delta\eta + \frac{1}{2}\left.\frac{\partial^2 f}{\partial \eta^2}\right|_0 \Delta\eta^2 - \frac{1}{6}\left.\frac{\partial^3 f}{\partial \eta^3}\right|_0 \Delta\eta^3 + O(\Delta\eta^4) \tag{48}$$

$$f_2 = f_0 - 2\left.\frac{\partial f}{\partial \eta}\right|_0 \Delta\eta + 2\left.\frac{\partial^2 f}{\partial \eta^2}\right|_0 \Delta\eta^2 - \frac{8}{6}\left.\frac{\partial^3 f}{\partial \eta^3}\right|_0 \Delta\eta^3 + O(\Delta\eta^4) \tag{49}$$

An appropriate linear combination of Eq. (48) and (49) is used to eliminate the third derivative term. This process yields the following relation

$$8f_1 - f_2 = 7f_0 - 6\left.\frac{\partial f}{\partial \eta}\right|_0 \Delta\eta + 2\left.\frac{\partial^2 f}{\partial \eta^2}\right|_0 \Delta\eta^2 + O(\Delta\eta^4) \tag{50}$$

Thus, the second order partial derivative is approximated by

$$\left.\frac{\partial^2 f}{\partial \eta^2}\right|_{\eta=1} = -\frac{7f(\xi,1)-8f(\xi,1-\Delta\eta)+f(\xi,1-2\Delta\eta)}{2\Delta\eta^2} + \frac{3}{\Delta\eta}\left.\frac{\partial f}{\partial \eta}\right|_{\eta=1} + O(\Delta\eta^2) \tag{51}$$

where the values of the streamfunction are determined from the previous iteration.

It should be noted that Eq. (51) is a function of the no-slip condition represented by Eq. (41) in the previous section. Substitution of the no-slip condition yields

$$\left.\frac{\partial^2 f}{\partial \eta^2}\right|_{\eta=1} = -\frac{7f(\xi,1)-8f(\xi,1-\Delta\eta)+f(\xi,1-2\Delta\eta)}{2\Delta\eta^2} + \frac{3u_{rot}}{\Delta\eta} + O(\Delta\eta^2) \tag{52}$$

Lastly, the vorticity on the surface of the cylinder is determined by substituting Eq. (52) into Eq. (47).

$$\omega(\xi,1) = \frac{7f(\xi,1)-8f(\xi,1-\Delta\eta)+f(\xi,1-2\Delta\eta)}{2\Delta\eta^2} - \left(\frac{3}{\Delta\eta}-1\right)u_{rot} \tag{53}$$

Eq. (53) can be used to approximate the surface vorticity for both steady or unsteady rotation in which the rotational speed is given. For a stationary cylinder, the rotational velocity is zero, and the equation is simplified.

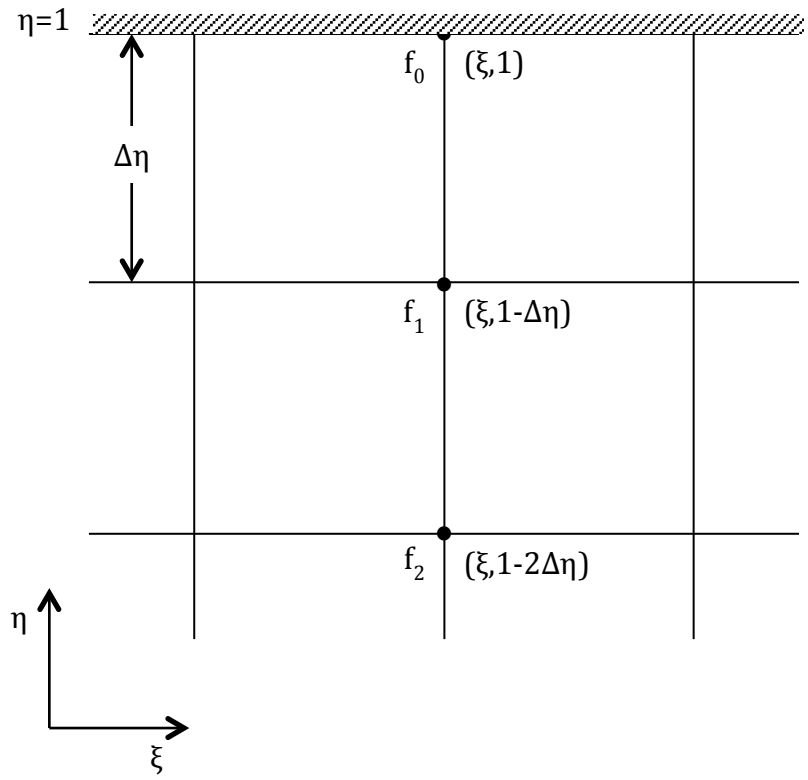

Figure 7: Discrete domain for the surface vorticity condition.

Periodic Boundary Conditions

Periodic cuts (ξ=0, ξ=1) result from the coordinate transformation between the physical and the computational domain (See Fig. 4 and Fig. 5). The nodes at these ξ-locations are essentially the same points. If the computational domain was wrapped around the cylinder, these are the locations where the grid would make contact with itself. Because of this process, periodic boundary conditions must also be applied. The periodic conditions are as follows

$$f(0,\eta) = f(1,\eta) \tag{54}$$

$$\omega(0,\eta) = \omega(1,\eta) \tag{55}$$

The equations for these conditions are found in the same manner as the discrete governing equations (Eq. (24) and (25)). Consider the computational domain shown in Figure 8. Let *k* be the point of interest on the periodic cut. The surrounding points are once again defined in the pointer system discussed in Section 3.1.1. However, there is a different treatment of the point to the west of *k* as it is on the boundary of the computational domain. The periodic conditions show that the point of interest at ξ=0 equals the point at the same η-location at ξ=1. Therefore, the west point is taken from the identical point at ξ=1. This results in a different set of equations for the pointer system than was previously given for the interior nodes:

$$\begin{aligned} k_1 &= k + 1 \\ k_2 &= k + N \\ k_3 &= k + N - 2 \\ k_4 &= k - N \end{aligned} \tag{56}$$

The same process is completed for the other periodic cut, as shown in Figure 9. The locations of the neighboring points can be determined using

$$\begin{aligned} k_1 &= k - N + 2 \\ k_2 &= k + N \\ k_3 &= k - 1 \\ k_4 &= k - N \end{aligned} \tag{57}$$

The streamfunction and vorticity at the periodic cuts can then be determined using the discrete governing equations given by Eq. (24) and (25).

It should be noted that the boundary conditions at the periodic cuts must be linearized in the same fashion as the discrete governing equations in order to have the

same variables for solution. A discussion of this linearization process can be re-visited in Section 3.1.2.

Force Coefficients

The force coefficients are determined using a formulation from previous works[7]. The lift and drag coefficients are defined respectively as

$$C_L = \frac{L}{\rho U_\infty^2 r}, \qquad C_D = \frac{D}{\rho U_\infty^2 r} \tag{58}$$

where L and D are the lift and drag forces per unit cylinder length. Each force coefficient consists of components due to friction forces and the pressure, which can be written as

$$C_L = C_{LF} + C_{LP}, \qquad C_D = C_{DF} + C_{DP} \tag{59}$$

Integration of the forces over the cylinder yields

$$C_{DF} = -\frac{2}{Re}\int_0^{2\pi} \omega|_{\eta=1} \sin(\theta)\, d\theta, \qquad C_{LF} = -\frac{2}{Re}\int_0^{2\pi} \omega|_{\eta=1} \cos(\theta)\, d\theta \tag{60}$$

$$C_{DP} = -\frac{1}{2}\int_0^{2\pi} P|_{\eta=1} \cos(\theta)\, d\theta, \qquad C_{LP} = \frac{1}{2}\int_0^{2\pi} P|_{\eta=1} \sin(\theta)\, d\theta \tag{61}$$

where P is the non-dimensional pressure of the cylinder[7]. The following relationship exists on the cylinder surface[8]

$$\frac{\partial P}{\partial \theta} = -\frac{4}{Re}\frac{\partial \omega}{\partial \eta}\Big|_{\eta=1} \tag{62}$$

The friction components given in Eq. (60) can be evaluated directly, while the pressure components are evaluated with integration by parts[7,8]. With integration by parts, the pressure components in Eq. (61) become

$$C_{DP} = -\frac{2}{Re}\int_0^{2\pi} \left.\frac{\partial \omega}{\partial \eta}\right|_{\eta=1} \sin(\theta)\, d\theta, \qquad C_{LP} = -\frac{2}{Re}\int_0^{2\pi} \left.\frac{\partial \omega}{\partial \eta}\right|_{\eta=1} \cos(\theta)\, d\theta \tag{63}$$

The derivative of the vorticity at the surface seen in Eq. (63) was approximated using the following third-order accurate backward difference

$$\left.\frac{\partial \omega}{\partial \eta}\right|_{\eta=1} \approx \frac{11\,\omega(i,j) - 18\,\omega(i,j-1) + 9\,\omega(i,j-2) - 2\,\omega(i,j-3)}{6\Delta\eta} + \mathcal{O}(\Delta\eta^3) \tag{64}$$

The force coefficients were calculated for each iteration, and the integrals seen in Eq. (60) and (63) were evaluated using the Trapezoidal rule.

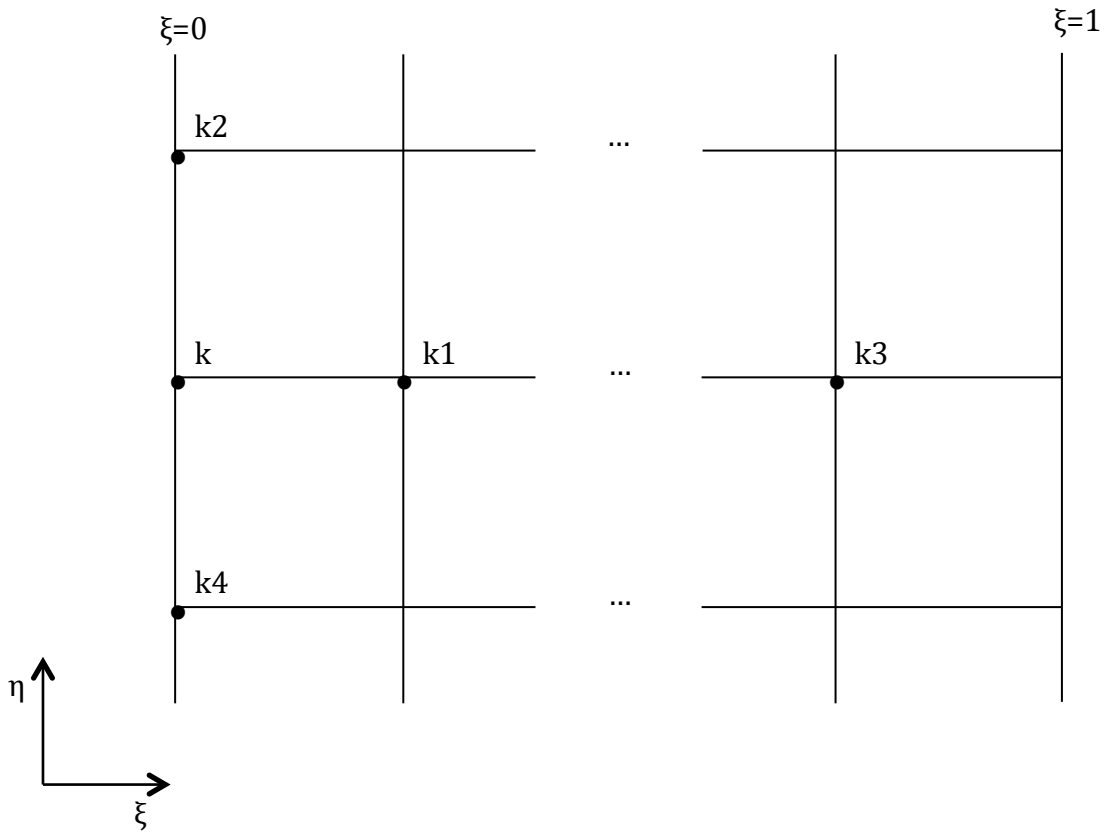

Figure 8: Discrete domain for the periodic boundary condition at $\xi=0$.

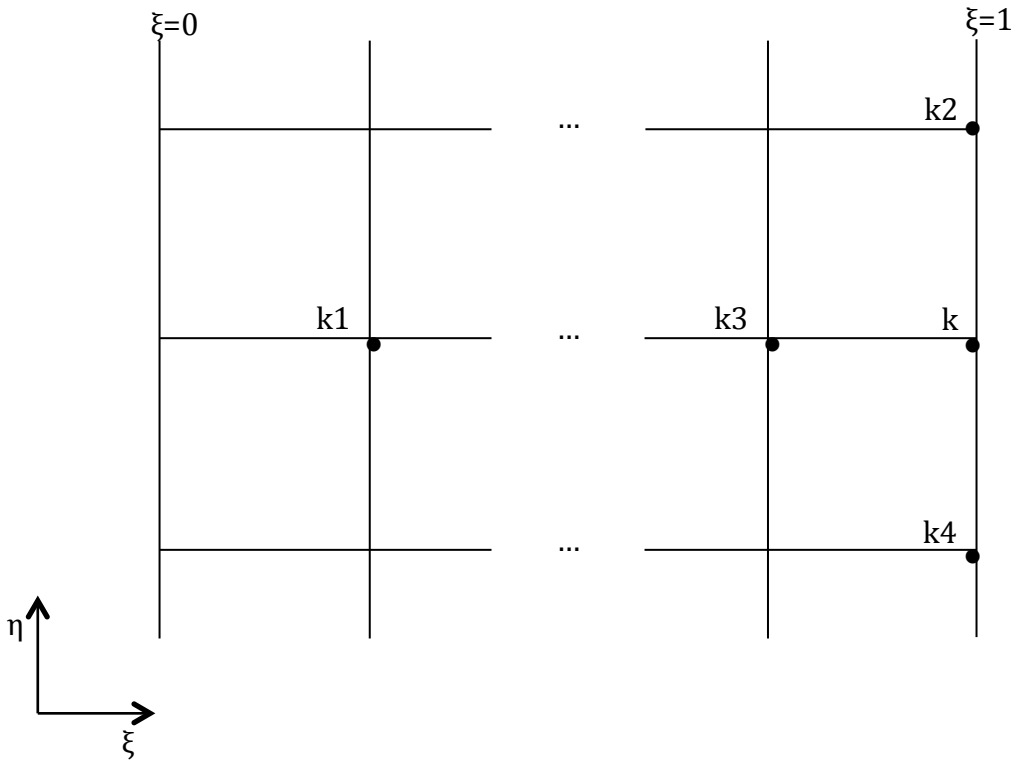

Figure 9: Discrete domain for the periodic boundary condition at ξ=1.

3.2 Unsteady Cylinder

3.2.1 Time-Accurate Method

The linearized governing equations and boundary conditions for steady flow over a circular cylinder were discussed in great detail in Section 3.1. Now consider the unsteady flow over a cylinder in cross-flow. The governing equations can be written in the convenient form seen in Eq. (26)

$$\begin{aligned} \frac{\partial \boldsymbol{\omega}}{\partial t} + \mathbf{V}(\boldsymbol{\omega}, \boldsymbol{f}) &= 0 \\ \mathbf{S}(\boldsymbol{\omega}, \boldsymbol{f}) &= 0 \end{aligned} \tag{65}$$

where the unsteadiness in the flow field is represented by the time derivative in the vorticity equation. The governing equations are integrated in time using a second-order backward difference approximation, which results in an implicit scheme. The finite difference approximation can once again be determined using the Taylor series approach. The Taylor series can be written for two points in the backwards direction such that

$$\omega^m = \omega^{m+1} - \frac{\partial \omega}{\partial t}\Delta t + \frac{1}{2}\frac{\partial^2 \omega}{\partial t^2}\Delta t^2 - \frac{1}{6}\frac{\partial^3 \omega}{\partial t^3}\Delta t^3 + O(\Delta t^4) \tag{66}$$

$$\omega^{m-1} = \omega^{m+1} - 2\frac{\partial \omega}{\partial t}\Delta t + 2\frac{\partial^2 \omega}{\partial t^2}\Delta t^2 - \frac{8}{6}\frac{\partial^3 \omega}{\partial t^3}\Delta t^3 + O(\Delta t^4) \tag{67}$$

An appropriate linear combination of Eq. (66) and (67) is used to eliminate the second derivative term. This process yields the following relation

$$-4\omega^m + \omega^{m-1} = -3\omega^{m+1} + 2\frac{\partial \omega}{\partial t}\Delta t + O(\Delta t^3) \tag{68}$$

Thus, the time derivative is approximated by the following second order backward difference approximation

$$\frac{\partial \omega}{\partial t} = \frac{3\omega^{m+1} - 4\omega^{m} + \omega^{m-1}}{2\Delta t} + O(\Delta t^2) \tag{69}$$

The resulting scheme is not self-starting, and a first order backward difference is used in the first iteration. The semi-discrete governing equations are given as

$$\begin{gathered} \frac{3\boldsymbol{\omega}^{m+1} - 4\boldsymbol{\omega}^{m} + \boldsymbol{\omega}^{m-1}}{2\Delta t} + \mathbf{V}(\boldsymbol{\omega}^{m+1}, \boldsymbol{f}^{m+1}) = 0 \\ \mathbf{S}(\boldsymbol{\omega}^{m+1}, \boldsymbol{f}^{m+1}) = 0 \end{gathered} \tag{70}$$

where (m+1) indicates the solution at the next physical time step. The solution is simplified by linearizing the implicit terms in Eq. (70). This is accomplished with the use of a Taylor series expansion about the previous time level for the implicit terms such that

$$\begin{aligned} \mathbf{V}(\boldsymbol{\omega}^{m+1}, \boldsymbol{f}^{m+1}) &\approx \mathbf{V}(\boldsymbol{\omega}^{m}, \boldsymbol{f}^{m}) + \left.\frac{\partial \mathbf{V}}{\partial \boldsymbol{\omega}}\right|_m (\boldsymbol{\omega}^{m+1} - \boldsymbol{\omega}^{m}) + \left.\frac{\partial \mathbf{V}}{\partial \boldsymbol{f}}\right|_m (\boldsymbol{f}^{m+1} - \boldsymbol{f}^{m}) \\ \mathbf{S}(\boldsymbol{\omega}^{m+1}, \boldsymbol{f}^{m+1}) &\approx \mathbf{S}(\boldsymbol{\omega}^{m}, \boldsymbol{f}^{m}) + \left.\frac{\partial \mathbf{S}}{\partial \boldsymbol{\omega}}\right|_m (\boldsymbol{\omega}^{m+1} - \boldsymbol{\omega}^{m}) + \left.\frac{\partial \mathbf{S}}{\partial \boldsymbol{f}}\right|_m (\boldsymbol{f}^{m+1} - \boldsymbol{f}^{m}) \end{aligned} \tag{71}$$

$$\begin{aligned} \Delta\boldsymbol{\omega}^{m+1} &= \boldsymbol{\omega}^{m+1} - \boldsymbol{\omega}^{m} \\ \Delta\boldsymbol{f}^{m+1} &= \boldsymbol{f}^{m+1} - \boldsymbol{f}^{m} \end{aligned} \tag{72}$$

By substituting Eq. (71) into (70) and with some rearranging of the time derivative term, the semi-discrete governing equations for the unsteady flow around a cylinder become

$$\begin{gathered} \frac{3}{2\Delta t}\Delta\boldsymbol{\omega}^{m+1} - \frac{1}{2\Delta t}\Delta\boldsymbol{\omega}^{m} + \mathbf{V}(\boldsymbol{\omega}^{m}, \boldsymbol{f}^{m}) + \left.\frac{\partial \mathbf{V}}{\partial \boldsymbol{\omega}}\right|_m \Delta\boldsymbol{\omega}^{m+1} + \left.\frac{\partial \mathbf{V}}{\partial \boldsymbol{f}}\right|_m \Delta\boldsymbol{f}^{m+1} = 0 \\ \mathbf{S}(\boldsymbol{\omega}^{m}, \boldsymbol{f}^{m}) + \left.\frac{\partial \mathbf{S}}{\partial \boldsymbol{\omega}}\right|_m \Delta\boldsymbol{\omega}^{m+1} + \left.\frac{\partial \mathbf{S}}{\partial \boldsymbol{f}}\right|_m \Delta\boldsymbol{f}^{m+1} = 0 \end{gathered} \tag{73}$$

Eq. (73) can be represented as a system of linear equations such that

$$\begin{bmatrix} \frac{\partial \mathbf{S}}{\partial \boldsymbol{f}} & \frac{\partial \mathbf{S}}{\partial \boldsymbol{\omega}} \\ \frac{\partial \mathbf{V}}{\partial \boldsymbol{f}} & \frac{3}{2\Delta t}\mathrm{I} + \frac{\partial \mathbf{V}}{\partial \boldsymbol{\omega}} \end{bmatrix}_m \begin{bmatrix} \Delta \boldsymbol{f} \\ \Delta \boldsymbol{\omega} \end{bmatrix}_{m+1} = \begin{bmatrix} -\mathbf{S} \\ -\mathbf{V} + \frac{1}{2\Delta t}\Delta \boldsymbol{\omega} \end{bmatrix}_m \tag{74}$$

Eq. (74) is very similar to its steady counterpart seen in Eq. (31), and the system is solved in the same fashion. It should also be noted that the boundary conditions derived in Section 3.1.3 are still valid for the unsteady case and are applied in the same manner.

3.2.2 Harmonic Balance Method

The ability to efficiently predict unsteady flow fields improves the fundamental understanding of the complex flow physics coupled with a reduction in development and design time[18]. In the past, time-linearized and nonlinear time-accurate methods were used to model such unsteady flows[15]. The time-linearized method assumes that the unsteady disturbances in the flow field are harmonic in time at a certain frequency and that they are small when compared to the mean flow. These assumptions lead to linearized governing equations about a mean operating condition, which can be solved efficiently. However, this method lacks the ability to model the nonlinear effect that may be profound for certain unsteady flow problems. Nonlinear time-accurate methods are traditionally considered for the solution of unsteady flow fields. As opposed to the time-linearized methods, the time-accurate approaches do not make any assumptions concerning the size of the unsteady disturbances. Thus, the time-accurate solvers have the ability to dynamically model the nonlinear effects in the flow field. Unfortunately, time-accurate methods are generally very computationally expensive; they can be multiple orders of magnitude more expensive than the frequency domain techniques[15]. The drawbacks of these methods resulted in a blend of the time and frequency domain techniques. Hall et al.[16] developed a harmonic balance method for temporally periodic flows. In this mixed time and frequency domain technique,

one makes use of the temporal periodicity of the flow in order to solve the flow field at certain snapshots in time. These snapshots are represented by a number of sub-time levels that are equally spaced over one period. In this case, the dependent variables are the conservation variables of the flow field. Rather than marching the solution from one physical time step to the next, all sub-time levels are computed simultaneously over a single period. The sub-time levels are only coupled to each other through a pseudo-spectral operator, which is used to approximate the time derivatives. There are many advantages with the harmonic balance technique[17]. By approximating the time derivatives, the problem can be treated as mathematically steady, and convergence acceleration techniques can be applied. Harmonic balance codes are well-suited for adjoint sensitivity analysis which can help with efficient design optimization[17]. Lastly, a key advantage of the harmonic balance method is its reduced computational cost. The computational cost of the harmonic balance approach was shown to scale nearly linearly with the number of sub-time levels used in the solution[15,17,18].

The harmonic balance method has been applied to many unsteady aerodynamics problems[17]. Previous investigators have studied problems such as multistage turbomachinery analysis[15] and unsteady flows about helicopter rotors in forward-flight[23], to name a few. Future applications could include the analysis and design of micro air vehicles, such as micro rotorcraft or micro flappers, since the unsteady flow about these vehicles is temporally periodic. The method would not be limited to low-speed flows as it could be applied for the analysis and design of hypersonic vehicles as well.

Harmonic Balance Application

Once again consider the unsteady flow over a circular cylinder, which is governed by the following set of equations

$$\begin{aligned} \frac{\partial \boldsymbol{\omega}}{\partial t} + \mathbf{V}(\boldsymbol{\omega}, \boldsymbol{f}) &= 0 \\ \mathbf{S}(\boldsymbol{\omega}, \boldsymbol{f}) &= 0 \end{aligned} \tag{75}$$

Clearly, the governing equations are coupled, and an unsteady term exists for the vorticity. The governing equations are traditionally integrated using time-accurate time-domain techniques[24]. However, if the unsteady flow field is periodic in time with a frequency f_f, the flow variables can be represented as a Fourier series with spatially varying coefficients[17]. With this consideration, the vorticity may be expressed as

$$\boldsymbol{\omega}^*(\xi,\eta,t_i) = A_0(\xi,\eta) + \sum_{n=1}^{N_H}\left[A_n(\xi,\eta)\cos\left(nf_f t_i\right) + B_n(\xi,\eta)\sin\left(nf_f t_i\right)\right];\ \text{i=1:2N}_\text{H}\text{+1} \quad (76)$$

where A_0, A_n, and B_n are the Fourier coefficients for the vorticity, i is the sub-time level, and N_H is the number of harmonics. The streamfunction can be represented in a similar fashion. Therefore, the vorticity and the streamfunction can be computed and stored at $2N_H$+1 equally spaced sub-time levels over a single period. Eq. (76) indicates that the Fourier coefficients and the sub-time level solutions are related through a pair of discrete transformations given by[17]

$$\underbrace{\begin{bmatrix}\omega_1\\ \omega_2\\ \vdots\\ \omega_{2N+1}\end{bmatrix}}_{\omega^*} = \underbrace{\begin{bmatrix}1 & \cos\left(f_f t_1\right) & \cdots & \sin\left(f_f t_1\right) & \cdots\\ 1 & \cos\left(f_f t_2\right) & \cdots & \sin\left(f_f t_2\right) & \cdots\\ \vdots & \vdots & \cdots & \vdots & \cdots\\ 1 & \cos\left(f_f t_{2N+1}\right) & \cdots & \sin\left(f_f t_{2N+1}\right) & \cdots\end{bmatrix}}_{\boldsymbol{E}^{-1}}\underbrace{\begin{bmatrix}A_0\\ A_1\\ \vdots\\ B_1\\ \vdots\end{bmatrix}}_{\widetilde{\omega}} \quad (77)$$

$$\begin{aligned}\omega^* &= \boldsymbol{E}^{-1}\widetilde{\omega}\\ \widetilde{\omega} &= \boldsymbol{E}\omega^*\end{aligned} \quad (78)$$

Once the flow variables are represented as a Fourier series, the governing equations can be written at all sub-time levels such that

$$\begin{aligned}\frac{\partial \boldsymbol{\omega}^*}{\partial t} + \mathbf{V}^*(\boldsymbol{\omega}^*, \boldsymbol{f}^*) &= 0\\ \mathbf{S}^*(\boldsymbol{\omega}^*, \boldsymbol{f}^*) &= 0\end{aligned} \quad (79)$$

Thus, the governing equations at all sub-time levels seen in Eq. (79) have $2N_H$+1 equations that are coupled only by the time derivative term. This unsteady term is approximated by a pseudo-spectral operator, **D**, given by

$$\frac{\partial \omega^*}{\partial t} = \mathbf{D}\omega^* \tag{80}$$

where

$$\mathbf{D} = \frac{\partial \boldsymbol{E}^{-1}}{\partial t}\boldsymbol{E} \tag{81}$$

Eq. (80) is known as the source term for the harmonic balance method. Substitution of the source term into the governing equations (Eq. (79)) yields the mathematically steady harmonic balance equations for the unsteady cylinder in cross-flow

$$\begin{gathered} \mathbf{D}\boldsymbol{\omega}^* + \mathbf{V}^*(\boldsymbol{\omega}^*, \boldsymbol{f}^*) = 0 \\ \mathbf{S}^*(\boldsymbol{\omega}^*, \boldsymbol{f}^*) = 0 \end{gathered} \tag{82}$$

Harmonic Balance Stability

Previous investigators[25,26] have studied the effect of the source term discretization on the stability of the harmonic balance solution. Woodgate and Barakos[25] discuss the differences between an explicit and implicit discretization of the source term. For an explicit source term, the solutions at each time level are only coupled by the residual of the discretized system. This occurs because an explicit source term only uses values based on a previous iteration. An explicit treatment of the source term has less computational requirements. However, this discretization limits the timestep, which can result in stability issues. An implicit source term couples the solutions at each sub-time level, while reducing the stability issues. The drawback for this treatment is the increased computational cost incurred[25]. Thomas et al.[26] determined that an explicit treatment of the source term allows the harmonic balance method to be applied to implicit flow solvers with few modifications to the implicit code. However, as discussed previously, this explicit treatment results in

unstable schemes. Thomas et al.[26] present a preconditioning technique, which stabilizes the harmonic balance equations with an explicit source term. This preconditioning method results in an unconditionally stable source term and presents a favorable alternative to the use of an implicit source term. Stability is achieved without the massive additional cost and complexity introduced with an implicit treatment of the source term. Thus, the harmonic balance equations seen in Eq. (82) were stabilized using the preconditioning technique developed by Thomas et al. The details of the technique can be found in Ref. [26].

3.3 Sensitivity Analysis

The goal of sensitivity analysis is to determine the sensitivity of a chosen objective function with respect to design variables[24]. Sensitivity information is particularly useful in computational fluid dynamics (CFD) as it can be used for design optimization, mesh adaptation and flow control[27]. The finite difference method and the adjoint method are two well-known sensitivity analysis techniques. One advantage of the harmonic balance technique is that the resulting CFD code is well-suited for adjoint sensitivity analysis, which can lead to efficient design optimization[17]. Unfortunately, due to time constraints, the adjoint method was not applied in this present work. Instead, a finite difference sensitivity analysis was conducted with the harmonic balance solver for a periodically oscillating cylinder. The finite difference approach is popular due to its simple implementation[28], but it is generally accompanied with higher computational costs than adjoint methods[29] when the number of design variables is large.

In this work, the mean coefficient of drag is chosen as the objective function, and the Strouhal number is the investigated design variable. Two iterative methods are implemented with the goal of using finite difference sensitivity analysis to determine a value of the Strouhal number, which minimizes the mean drag coefficient. The first is the following Newton's method

$$St_{new} = St_d - R\frac{C_d'}{C_d''} \tag{83}$$

where R is a relaxation variable. Second order central difference approximations were used to approximate the derivatives in Eq. (83). These finite difference approximations are shown below

$$\begin{aligned} C_d' &= \frac{\partial C_d}{\partial St_d} = \frac{C_d(St_d+\epsilon)-C_d(St_d-\epsilon)}{2\epsilon} \\ C_d'' &= \frac{\partial^2 C_d}{\partial St_d^2} = \frac{C_d(St_d+\epsilon)-2C_d(St_d)+C_d(St_d-\epsilon)}{\epsilon^2} \end{aligned} \tag{84}$$

where ϵ is a small perturbation applied to the Strouhal number for the harmonic balance solution.

The second iterative method used for the sensitivity analysis is the steepest descent approach given by

$$St_{new} = St_d - RC_d' \tag{85}$$

This method is very similar to Newton's method (see Eq. (83)) except that the second derivative is not used to calculate the next value of the Strouhal number.

The general process for an optimization problem based on the finite difference sensitivity analysis is shown in Figure 10. The Strouhal number and rotational speed (Ω) are the chosen input parameters for the harmonic balance solver. The Strouhal number is taken as the design variable, and the mean drag coefficient is the variable of interest from the harmonic balance solution. An initial harmonic balance solution is obtained from the chosen input parameters. The design variable is then perturbed by a small amount in both the forward and backward directions, and new harmonic balance solutions are obtained with these perturbed Strouhal numbers. The mean drag coefficients from the three solutions are then used to determine a new Strouhal number via Eq. (83) or Eq. (85). The process should be continued until the drag coefficient is minimized ($C_d' \approx 0$). Note that Eq.

(83) and Eq. (85) can converge on a local maximum, where the first derivative of the drag coefficient is also zero.

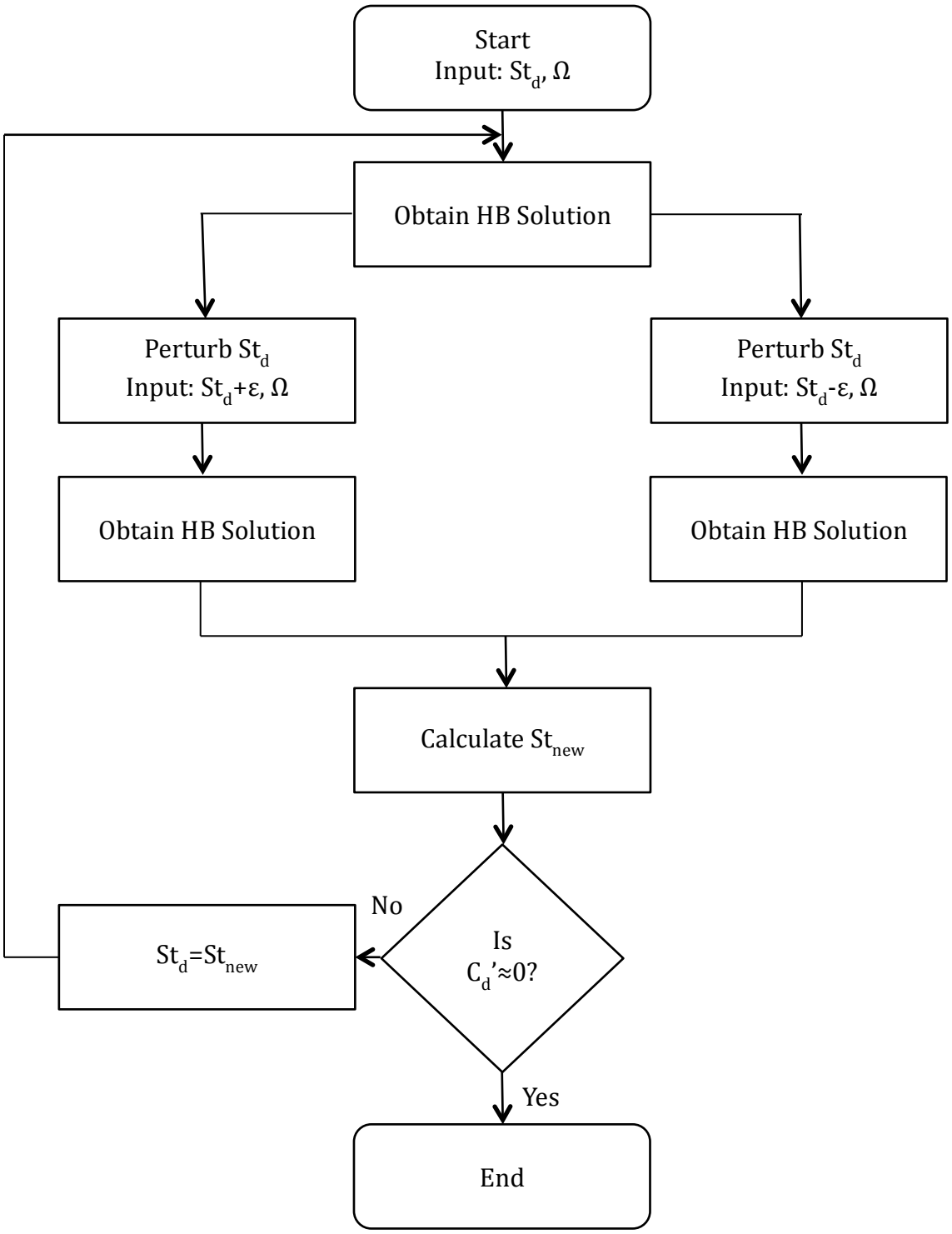

Figure 10: Finite difference sensitivity analysis process for a rotationally oscillating cylinder.

Chapter 4: Results

4.1 Steady Cylinder

4.1.1 Stationary Cylinder

In general, three flow regimes can be defined for flow over a stationary cylinder: the steady laminar regime ($Re<47$), the unsteady laminar two-dimensional vortex shedding regime ($47 \leq Re < 200$), and the unsteady three-dimensional vortex shedding regime ($Re>200$)[6]. At low Reynolds numbers in the steady laminar regime, the wake behind the cylinder has a steady circulation region with two symmetric vortices attached to the cylinder, whose size increases with increasing Reynolds number. Flow instabilities due to a large fluctuating pressure causes vortex shedding to occur in the wake behind the cylinder in the unsteady laminar regime. As the Reynolds number increases beyond the unsteady laminar regime, the flow behind the cylinder becomes three-dimensional and turbulent, with complex vortex shedding patterns[3]. To correctly determine the flow field, an unsteady flow solver should be used when $Re \geq 47$. While the steady cylinder problem is not physical for higher Reynolds numbers, it provides a good initial solution for the unsteady solvers developed. Thus, the higher Reynolds numbers have been investigated using the steady solver. The stationary cylinder was investigated for multiple Reynolds numbers using a 181x181 grid, and the streamlines and vorticity contours for three of those cases are presented in Figures 11, 12 and 13. The figures show the characteristics expected from the steady laminar regime. Each figure has two symmetric vortices attached to the cylinder, and the size of these vortices grows as the Reynolds number increases. Figure 13 is not a physical solution. A Reynolds number of 100 falls within the unsteady laminar regime, and a steady solver is incapable of capturing the unsteady nature of the flow field. However, this solution is important as it is used as a baseline solution for the unsteady solver developed in this work.

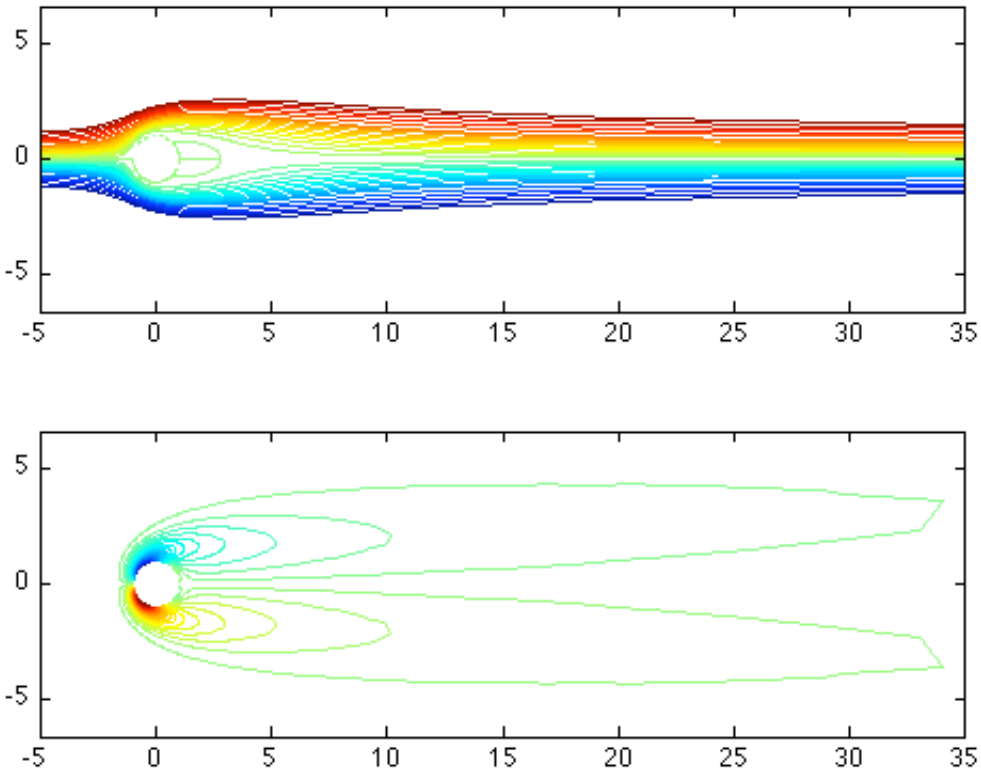

Figure 11: Steady flow over a stationary cylinder for Re=20. Top to bottom: streamlines, vorticity contours.

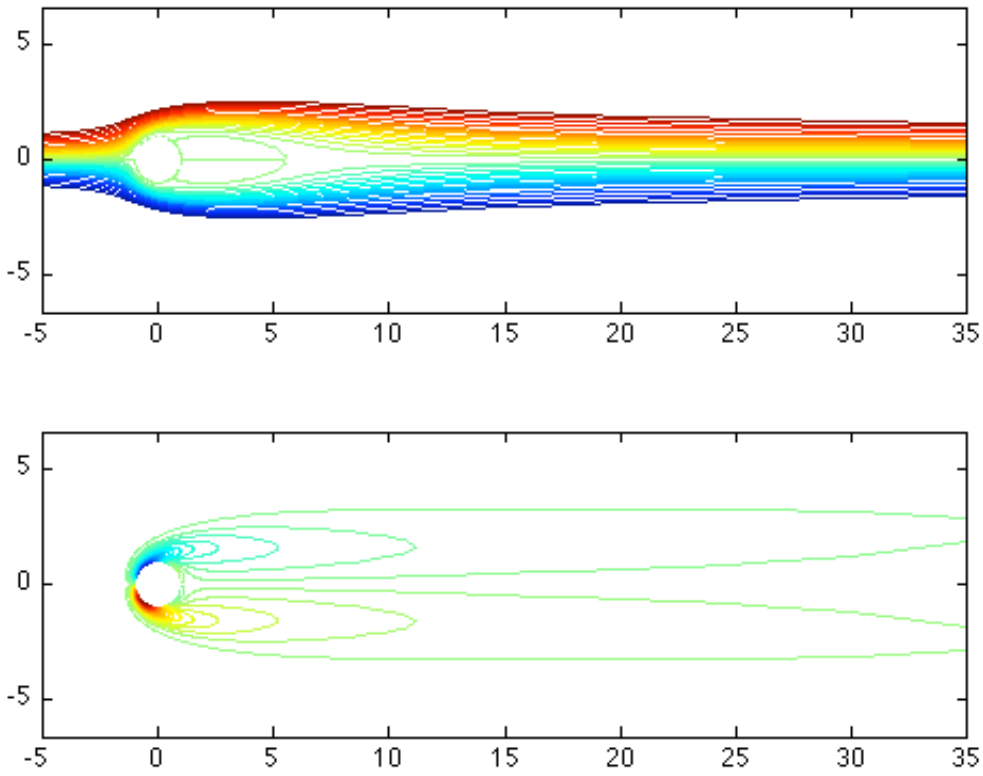

Figure 12: Steady flow over a stationary cylinder for Re=40. Top to bottom: streamlines, vorticity contours.

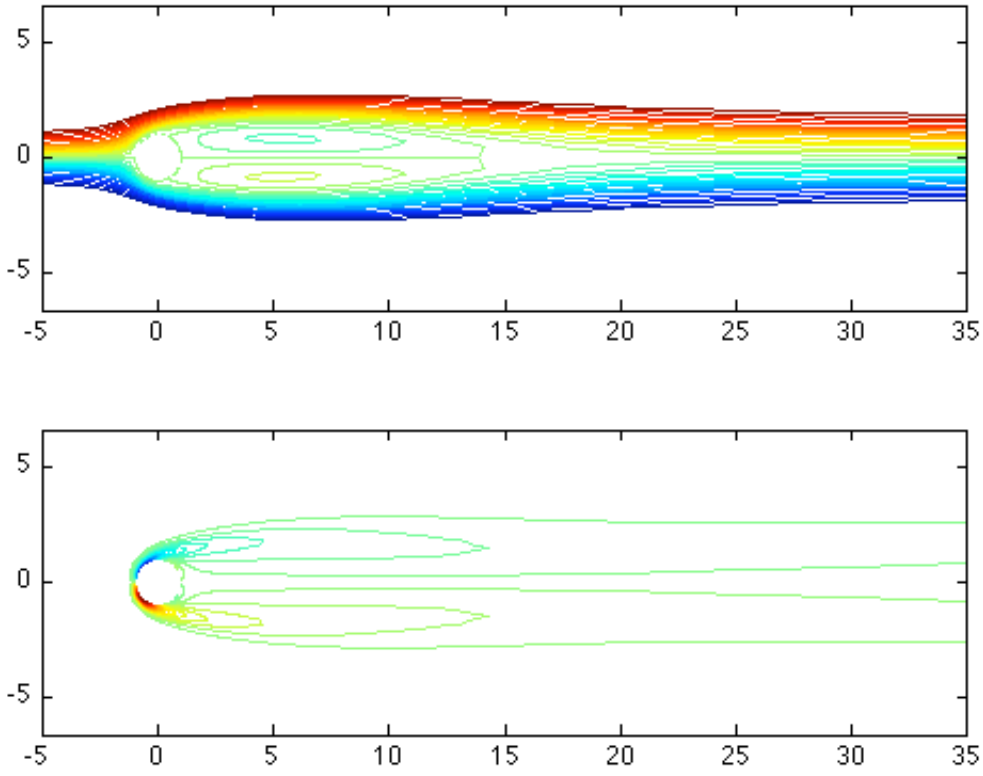

Figure 13: Non-physical solution of steady flow over a stationary cylinder for Re=100. Top to bottom: streamlines, vorticity contours.

4.1.2 Constant Rotation

Ingham and Tang[7] conducted a numerical investigation of steady flow past a rotating cylinder. Their results were used in the validation of the steady solver. The parameters for the steady cylinder in constant rotation are the Reynolds number and the rotational parameter α

$$Re = \frac{2rU_\infty}{\nu} \tag{86}$$

$$\alpha = \frac{r\dot{\theta}}{U_\infty} \tag{87}$$

where r is the radius of the cylinder, U_∞ is the free stream velocity, $\dot{\theta}$ is the angular velocity and ν is the kinematic viscosity. Ingham and Tang[7] show a cylinder in steady rotation for Re=20 with a variety of rotational parameters and contour levels for a 41x41 computational grid. For comparison, multiple cases were run in the steady solver using the same parameters and contour levels. However, the chosen mesh of 181x181 for the steady solver was much finer than the literature.

A comparison of the lift and drag coefficients are presented in Table 1. The results match the previous work[7] qualitatively. An increase in the rotation rate yields higher lift coefficients and slightly lower drag coefficients. Quantitatively, the results are close with the highest percent difference equal to approximately 13%. The coefficients of lift are in fair agreement, as the max percent difference is less than 5%. The drag coefficients are in even better agreement with the exception of the higher rotation rates—especially that of α=2. This increase in error for higher rotation rates is consistent with previous works[7]. The steady solver developed in this work consistently predicts higher lift coefficients than Ingham and Tang[7], while predicting smaller drag coefficients. These discrepancies led to an investigation of the numerical methods used to determine the lift and drag coefficients. The current solver uses Trapezoidal integration to calculate the force coefficients, while Ingham and Tang[7] use Simpson's rule. A simple change to the numerical integration in the current solver made no difference in the resulting coefficients of lift and drag. To determine whether round-off errors could be the explanation for the differences, the current solver was run with single precision variables instead of the normal double precision process. This made no difference in the resulting lift and drag coefficients. This led to further investigation of previous works. Badr et al.[8] also conducted a study of steady flow past a rotating cylinder for low Reynolds numbers. Comparison of the lift and drag coefficients to these previous works is shown in Figures 14 and 15, respectively. The steady solver gives lift coefficients that are bounded by the previous work. While C_L is slightly higher than that of Ingham and Tang[7], it is slightly lower than Badr et al.[8] The drag coefficient results are in good agreement with the previous works, with slight differences for the higher rotation rates. The drag coefficients are lower than the previous works[7,8] for the higher rotation

rates. This is shown clearly in Fig. 14 and Fig. 15. The inconsistencies in the results can be attributed to the difference in the computational grid. The previous works used a much coarser mesh (41x41) than the present work (181x181). Ingham[7] even suggests that previous works "severely underestimate" the lift coefficient due to their use of a coarse mesh, though this does not explain the discrepancy between their results and Badr et al.[8] To investigate this effect, the steady solver was run for a mesh size of 41x41. The results are shown in Table 2. The coarser mesh yields lift coefficients that are closer to the previous results[7], especially for the higher rotation rates. However, the coarser mesh also gives larger differences for the drag coefficient with the exception of the higher rotation rates. Stojkovic et al.[6] note that previous works could be in error for the higher rotation rates. Large gradients occur in the flow field for higher rotation rates, and these cannot be accurately detected for a coarse grid[6]. The current results are based on a finer mesh, which yields better resolution than that of the previous works.

While there are discrepancies between the predicted lift and drag coefficients, the flow pattern around the cylinder nearly matches those of Ingham and Tang[7]. The comparison of the streamlines are shown in Figure 16. Ingham and Tang[7] noticed the same phenomenon. Their coefficients of lift and drag varied from previous works at the time, but their flow patterns were "graphically indistinguishable"[7]. Stojkovic et al.[6] noticed this result as well. They note that "there is a large scatter among the different authors concerning the predicted drag and lift coefficient" for steady laminar flow[6]. They also suspect that these variations are due to the coarse mesh sizes used by the previous authors.

Table 1: Comparison of coefficients in steady rotation to previous works[7]. Re=20. 181x181 grid.

α	C_L	C_L Ref.[7]	C_L % Diff.	C_D	C_D Ref.[7]	C_D % Diff.
0.1	0.265	0.254	4.331	1.995	1.995	0.000
0.2	0.531	0.514	3.307	1.990	1.992	0.100
0.4	1.065	1.024	4.004	1.970	1.979	0.455
0.5	1.333	1.283	3.897	1.955	1.973	0.912
1	2.709	2.617	3.515	1.832	1.925	4.831
2	5.783	5.719	1.119	1.406	1.627	13.583

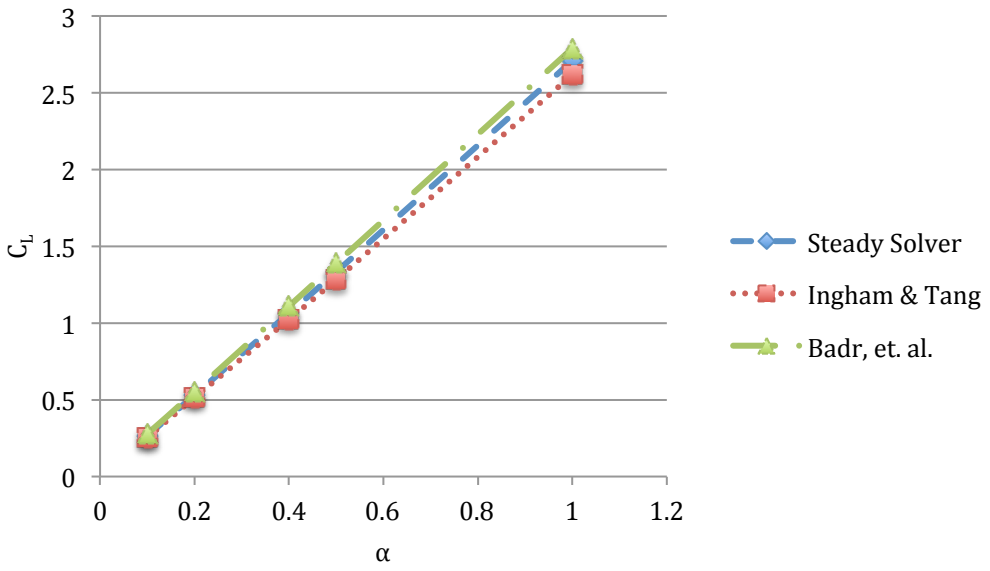

Figure 14: Lift coefficient as a function of the rotation rate for steady flow with constant rotation. *Re*=20.

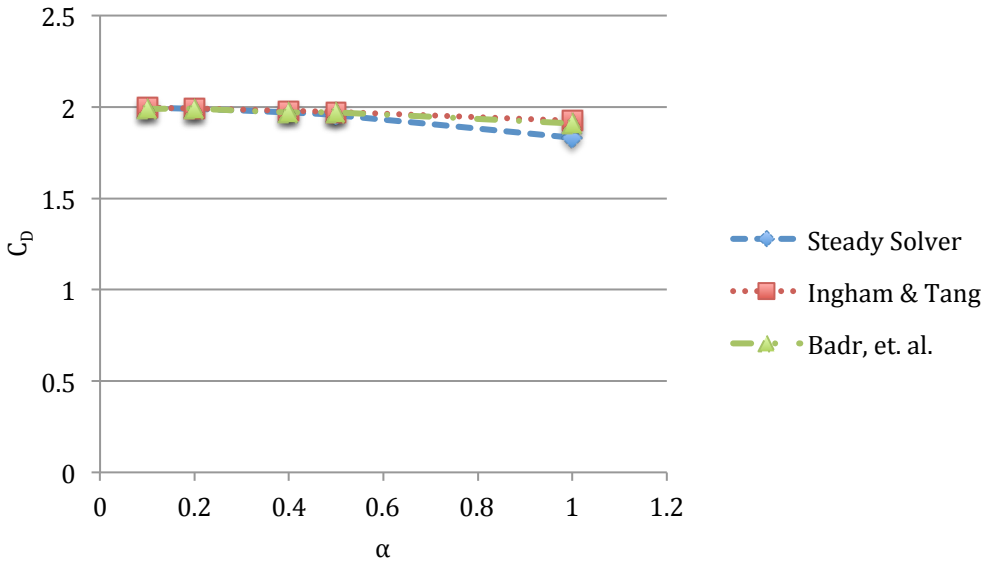

Figure 15: Drag coefficient as a function of the rotation rate for steady flow with constant rotation. *Re*=20.

Table 2: Effect of coarser mesh on steady solver compared to previous works[7]. *Re*=20. 41x41 grid.

α	C_L	C_L Ref.[7]	C_L % Diff.	C_D	C_D Ref.[7]	C_D % Diff.
0.1	0.265	0.254	4.331	2.049	1.995	2.707
0.2	0.529	0.514	2.918	2.042	1.992	2.530
0.4	1.016	1.024	0.781	2.016	1.979	1.860
0.5	1.316	1.283	2.572	1.997	1.973	1.216
1	2.639	2.617	0.841	1.865	1.925	3.117
2	5.693	5.719	0.455	1.450	1.627	10.879

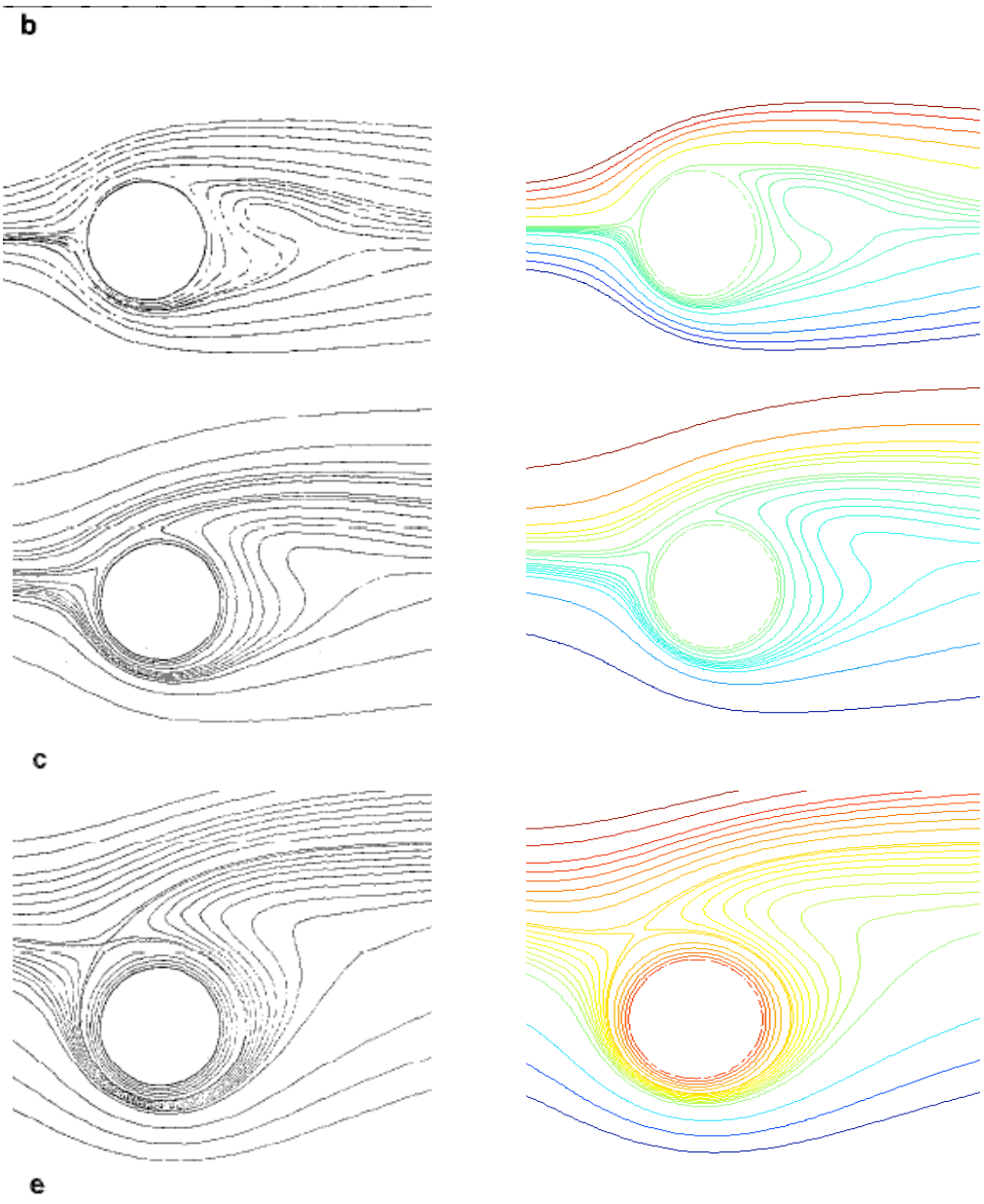

Figure 16: Validation of steady solver for the cylinder in steady rotation. *Re*=20. Left: Previous results (see Ref.[7]). Right: Steady solver results. From top to bottom the rotational parameter is α=0.1, 0.5, 2.

Previous works have also determined a linear relationship between the coefficient of lift and the rotation rate for low rotational speeds[6,7]. Stojkovic et al.[6] found that the coefficient of lift is a linear function of the rotational parameter for $\alpha \leq 2$. However at higher rotational speeds, an increasing lift coefficient results from an increasing Reynolds number[6]. This relationship has been investigated using results from the current steady solver. Figure 17 shows the lift coefficient as a function of the rotation rate ($0 \leq \alpha \leq 2$). A linear trendline was added to the plot along with the coefficient of determination (R^2). The R^2 value is used to determine how well a line fits the data[29]. The coefficient of determination ranges from 0 to 1. A R^2 close to 0 indicates that the line does not fit the data well; whereas a coefficient of determination close to 1 shows that the linear fit is good. The R^2 for the lift coefficient as a function of $\alpha \leq 2$ is 0.999, which agrees with the results of previous works. The fit is even closer when the rotation range is $0 \leq \alpha \leq 1$, and it is slightly worse when the range includes higher rotation rates ($\alpha \leq 3$).

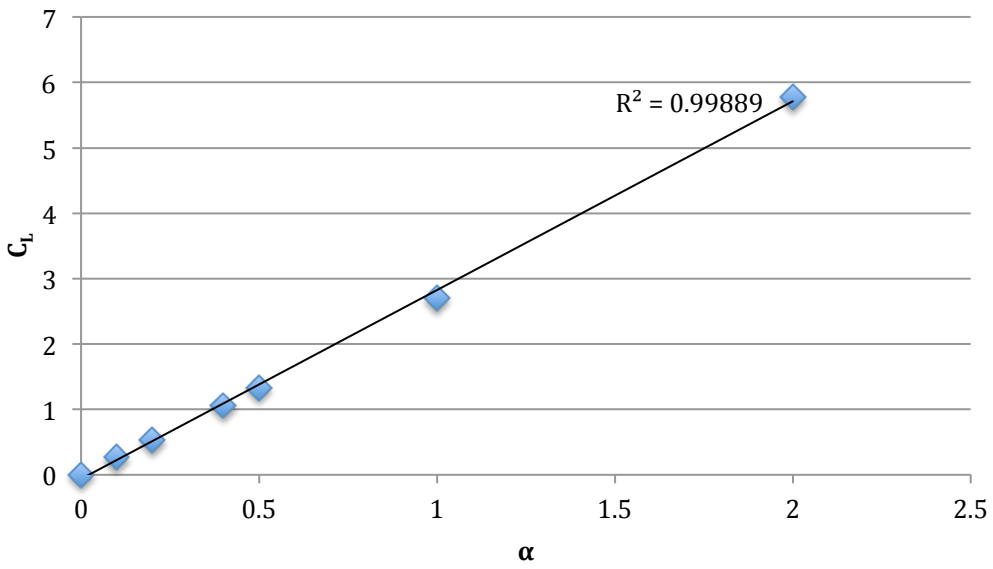

Figure 17: Linear relationship between the lift coefficient and the rotation rate for steady flow with constant rotation. R^2 indicates the fit of the trendline. *Re*=20.

4.2 Unsteady Cylinder

4.2.1 Time-Accurate Results

The time-accurate solver was validated for two different classifications: constant rotation and oscillatory periodic rotation. The results of the cylinder in constant rotation are visited first.

Constant Rotation

There have been many investigations of flow past a cylinder rotating with a constant angular velocity[3,6,8,9,30]. Similar to the steady flow in constant rotation, this flow is dependent on two non-dimensional parameters—the Reynolds number and the rotational speed. The Reynolds number is still defined by Eq. (86), and the rotational speed is defined as

$$\Omega = \frac{\dot{\theta} d}{2U_\infty} \tag{88}$$

where $\dot{\theta}$ is the angular velocity of the cylinder, d is the diameter, and U_∞ is the free-stream velocity.

The unsteady time-accurate solver was validated for multiple Reynolds numbers by comparing the results to those of previous investigators[8,30]. These investigators studied low Reynolds number cases at low rotation speeds. For these rotation rates, the flow develops a periodic vortex shedding pattern also known as the Karman vortex street[30]. The lift coefficient eventually reaches a periodic state, which is shown Figure 18. The temporal variation of the lift coefficient agrees with previous works[8]. However, the solver has lower peaks than those of Badr et al.[8] Their work has higher initial peaks around t=8 for all rotation rates. The temporal variation of both the lift and drag coefficients were investigated for Re=100 and Ω=1. This is shown in Figure 19. Once again, the initial peaks

are lower with the current results, and the coefficients seem to be slightly lower than the previous work. Ingham and Tang[7] mention this result in their work as well. They note that the lift coefficients estimated by Badr et al.[8] are a little higher than those obtained by all of the previous investigators[30]. Previous works have espoused the importance of the conditions imposed at large distances[30]. The far-field boundary conditions discussed in Section 3.1.3 were implemented in all the flow solvers in this work. The differences between the current results as those of Badr et al.[8] could likely be due to the difference in the condition set at infinity. While the solvers from this work use the condition discussed by Ingham and Tang[7], Badr et al.[8] used the asymptotic Oseen solution for their far-field condition. As with the steady solver, there is once again a discrepancy in the grid size. The current results are determined from a much finer mesh than the previous works; the cases shown in Fig. 18 and Fig. 19 were run with a 181x181 mesh.

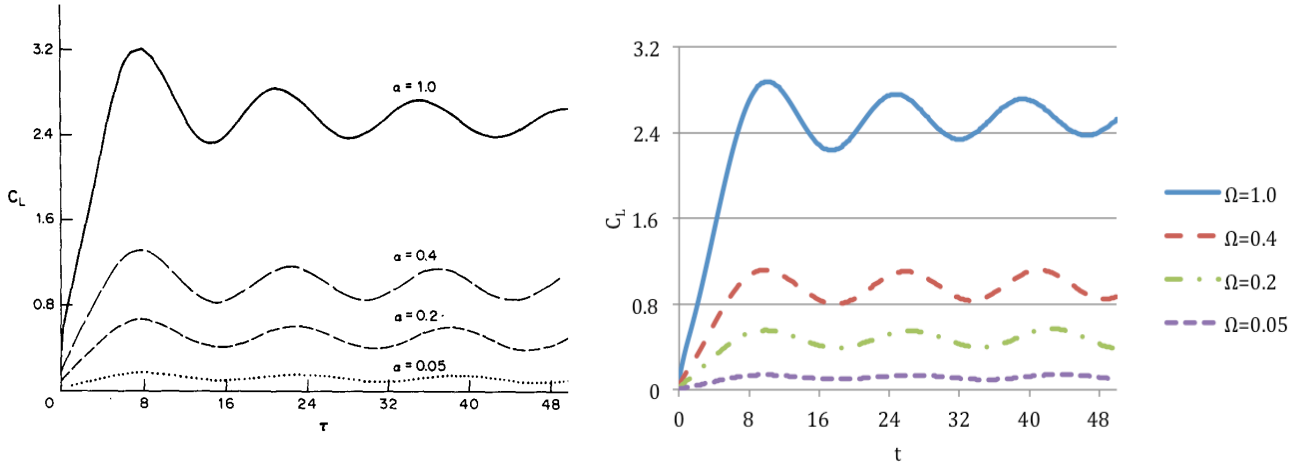

Figure 18: Temporal variation of the lift coefficient for unsteady flow with constant rotation. *Re*=60. Left: Fig. 13, Ref. [8]. Right: Current work.

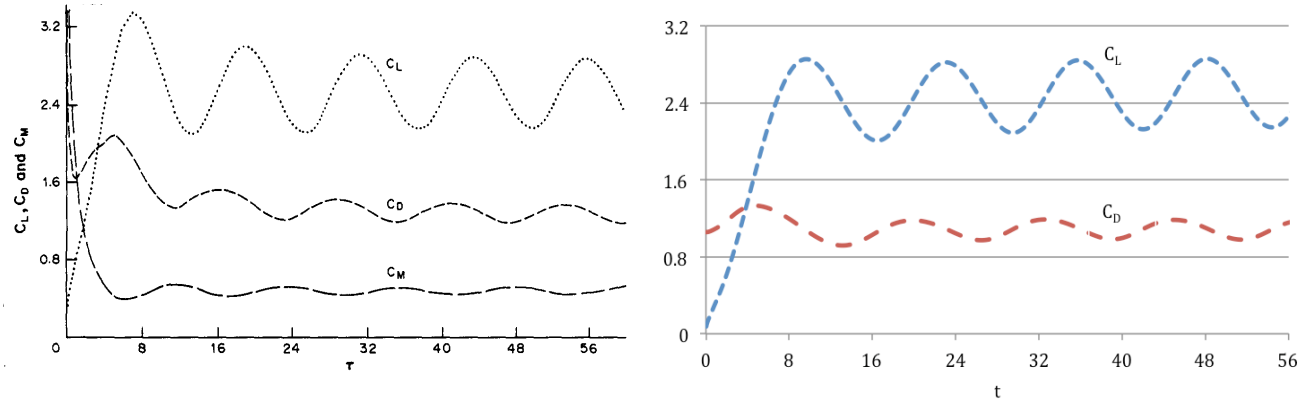

Figure 19: Temporal variation of the lift and drag coefficients for unsteady flow with constant rotation. *Re*=100. Ω=1. Left: Fig. 15, Ref. [8]. Right: Current work.

For further comparison, the average value of the lift coefficient was investigated for *Re*=60. The average lift coefficient was calculated over a complete periodic cycle and was compared to the previous work of Badr et al.[8] Despite the discrepancies between the peak values in the temporal variations, the mean lift coefficients are in great agreement with the previous works. Figure 20 shows the variation of the mean lift coefficient with the rotational speed. Ingham and Tang[7] have slightly lower values for the average lift coefficient. However, this result is consistent with those from the steady solver. The difference will once again be attributed to the coarse grid size used in the previous works. All results are in qualitative agreement with concern to the relationship between the mean lift coefficient and the rotational speed. For low rotation rates, the average lift coefficient is a linear function of the rotational speed[3]. This relationship is shown in Figure 20. A linear trendline can be added to the results to determine the coefficient of determination for the data. The trendline yields a coefficient of determination of R^2=0.999, which confirms that a linear trend is a good fit.

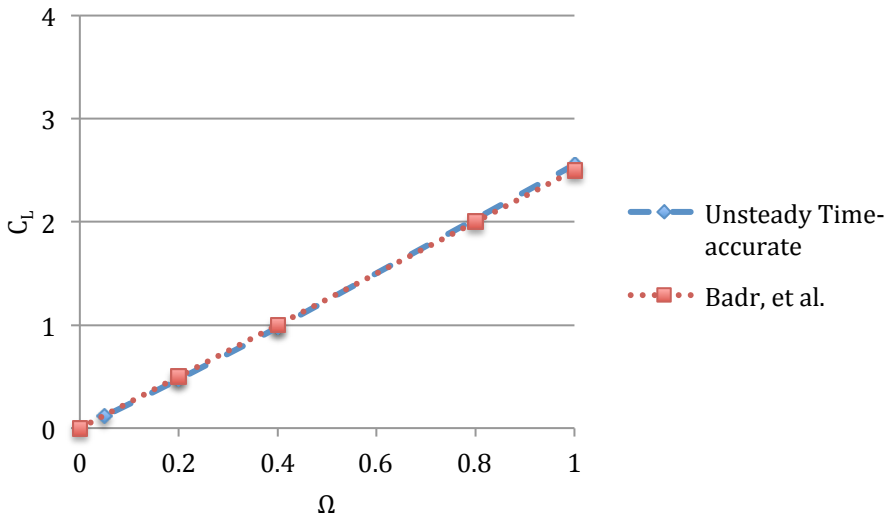

Figure 20: Variation of the mean lift coefficient with rotational speed for unsteady flow with constant rotation. *Re*=60.

As discussed previously, the flow over a cylinder for higher Reynolds numbers develops a vortex shedding pattern. Many previous investigators have studied the problem of unsteady flow past a constantly rotating cylinder[3,8,6,30]. Earlier investigations considered low rotation rates and showed that the lift coefficient eventually reaches a periodic state due to the vortex shedding[8,30]. This effect can be seen clearly in Fig. 18 and Fig. 19. Kang et al.[3] and Stojkovic et al.[6] looked at higher rotation rates. They determined that the vortex shedding occurs up to a critical rotation rate. Past this critical rotation rate, the vortex shedding is suppressed. The flow field, and subsequently the lift coefficient, tend to a steady state[3,6]. The temporal variation of the lift coefficient was investigated for *Re*=100 and *Re*=200, which can be seen in Figures 21 and 22, respectively. Kang et al.[3] determined a critical rotation rate of approximately Ω=2 for which the vortex suppression occurs. The present work agrees with this result as seen in Fig. 21. At Ω=2, the lift coefficient goes to a steady state, which indicates vortex suppression. The solutions of the flow field for Ω=2 and Ω=1 are shown in Figures 23 and 24, respectively. Mittal and Kumar[9] investigated the flow for *Re*=200. The results for the temporal lift coefficient of the present work are shown in

Fig. 22. The lift coefficients are in excellent agreement with the previous work with the exception of the higher rotational speeds. The results are slightly different for Ω=4.6, 4.7, and 5.0. The most notable difference is with Ω=5.0. Mittal and Kumar[9] found this lift coefficient to be steady past approximately 150 s. As can be seen in Fig. 22, the coefficient of lift continues to vary past this time, and still has not reached a steady value at 250 s. Fig. 22 also indicates vortex suppression for $2.07 \leq \Omega \leq 4.2$, as the lift coefficients tend towards a steady state. The suppressed flow field, which looks almost like potential flow, can be seen in Figure 25. Vortex suppression is not achieved for a rotation rate less than 2.07. This is shown in Figure 26. While the vortex shedding occurs, a pair of vortices sheds alternately from the cylinder surface. Figure 26 shows a counterclockwise rotating vortex shedding from the lower surface. Over a shedding cycle, clockwise vortices are shed from the upper surface. The vorticity solutions in Fig. 25 and Fig. 26 agree well with the previous works[9].

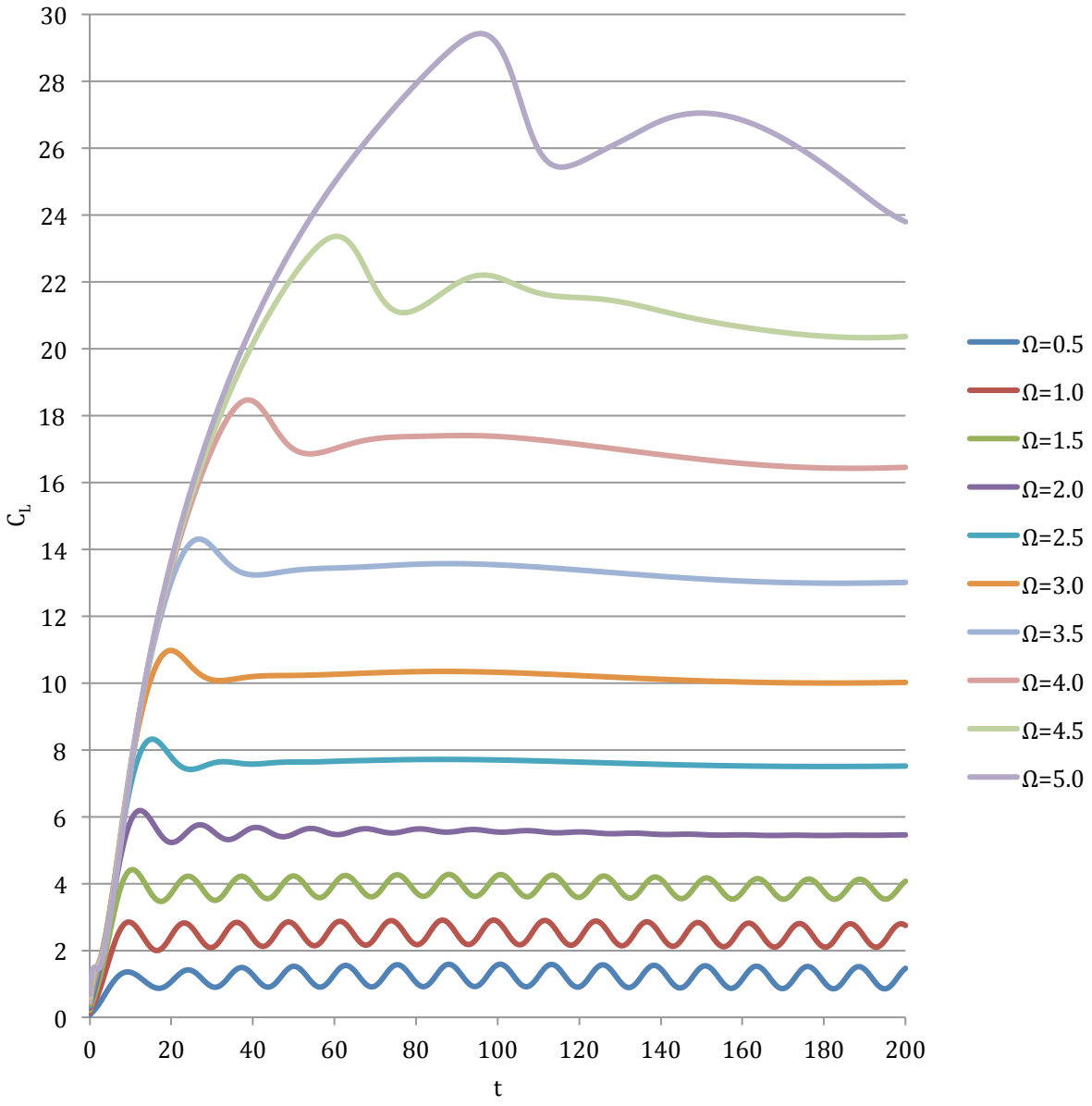

Figure 21: Temporal variation of the lift coefficient for unsteady flow with constant rotation. *Re*=100.

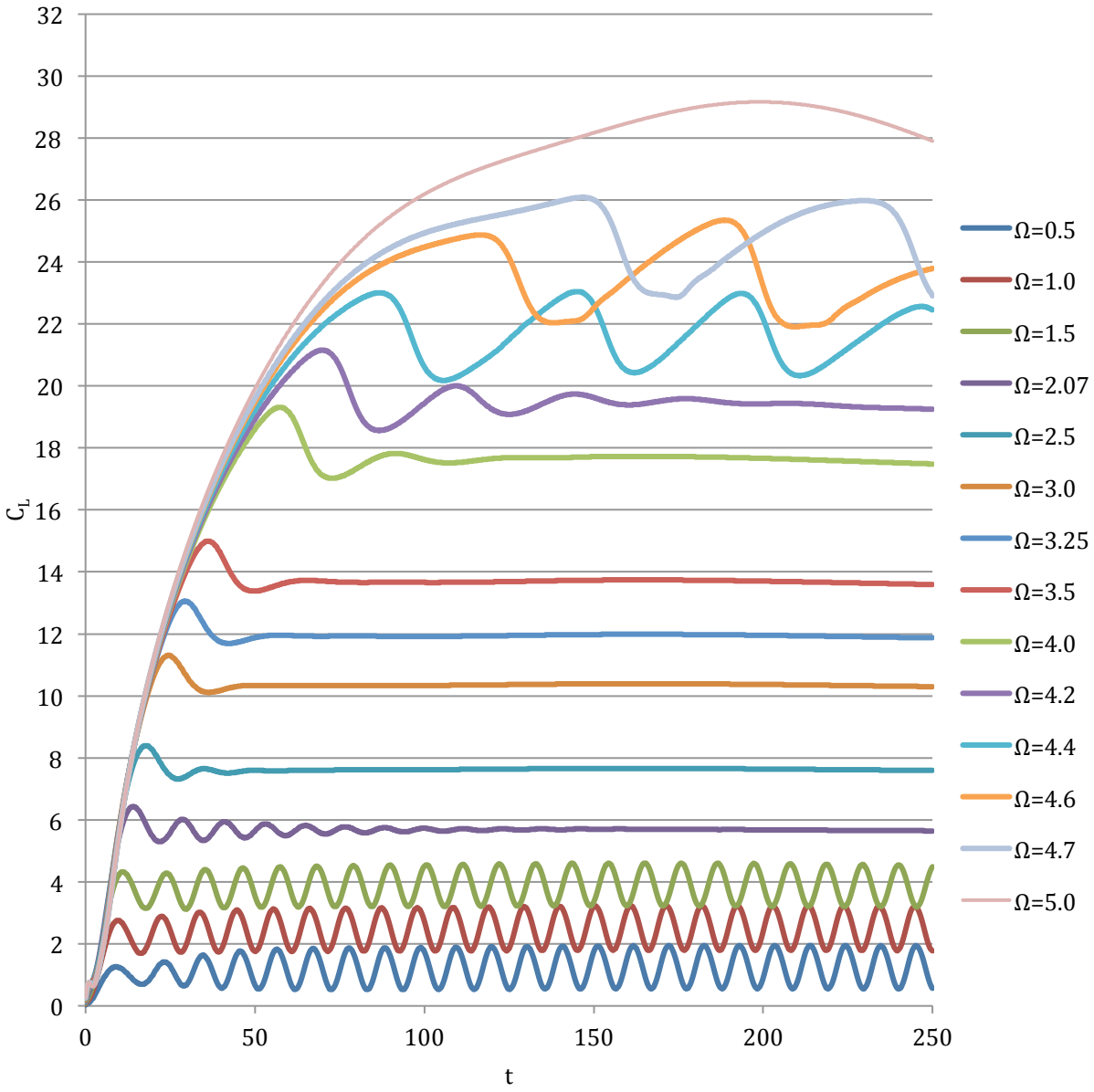

Figure 22: Temporal variation of the lift coefficient for unsteady flow with constant rotation. *Re*=200.

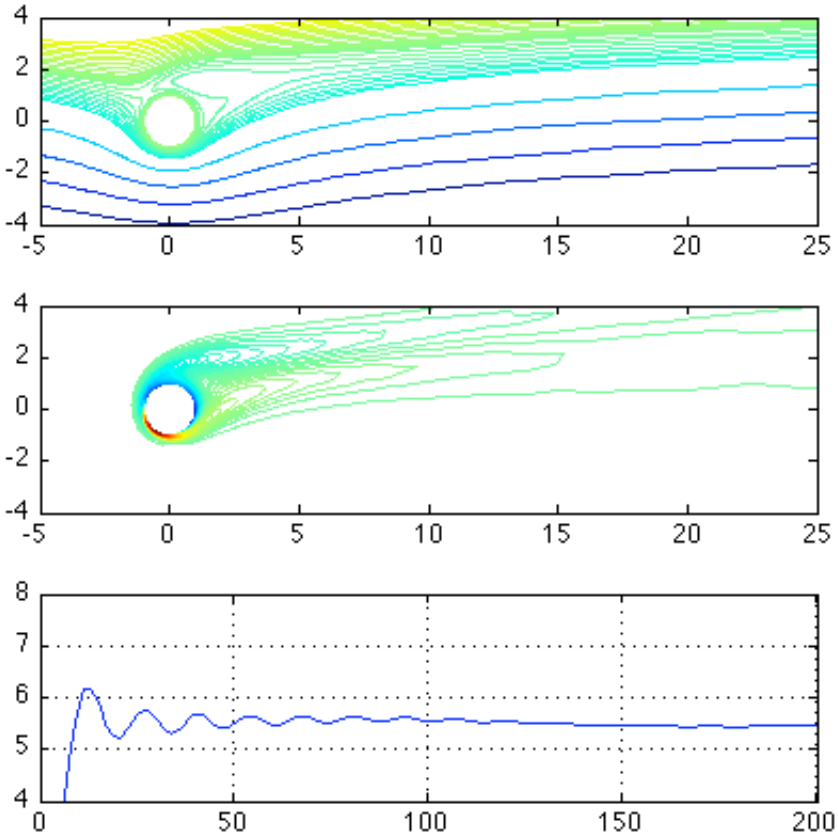

Figure 23: Vortex suppression for Re=100. Time-accurate solution for unsteady flow with a rotation rate of Ω=2. From top to bottom: streamlines, vorticity, temporal lift coefficient.

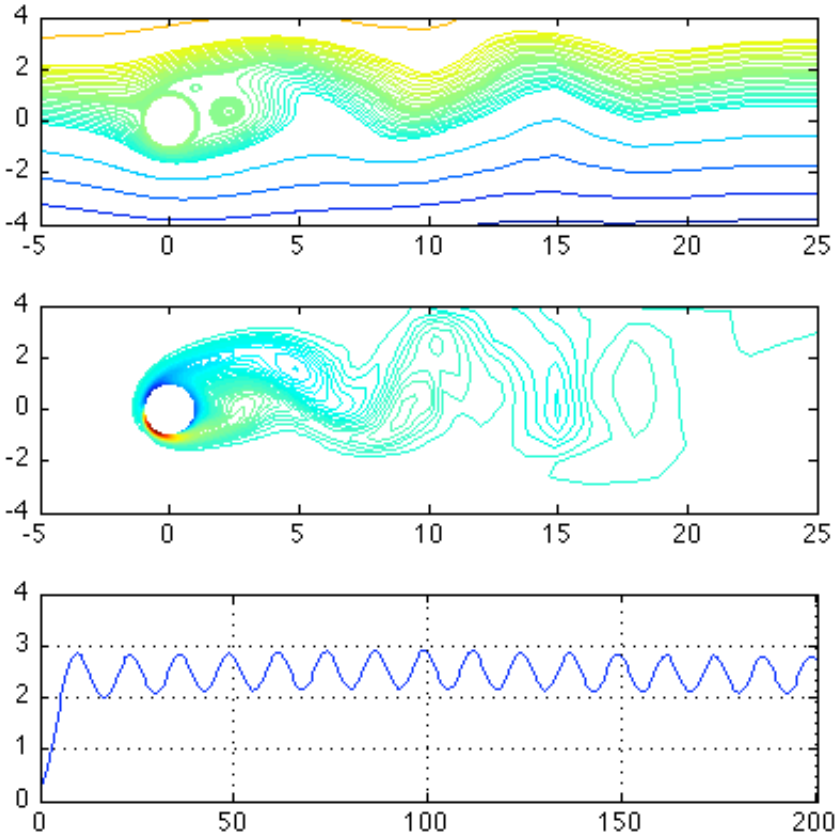

Figure 24: Time-accurate solution for Re=100 flow with a rotation rate of Ω=1. From top to bottom: streamlines, vorticity, temporal lift coefficient.

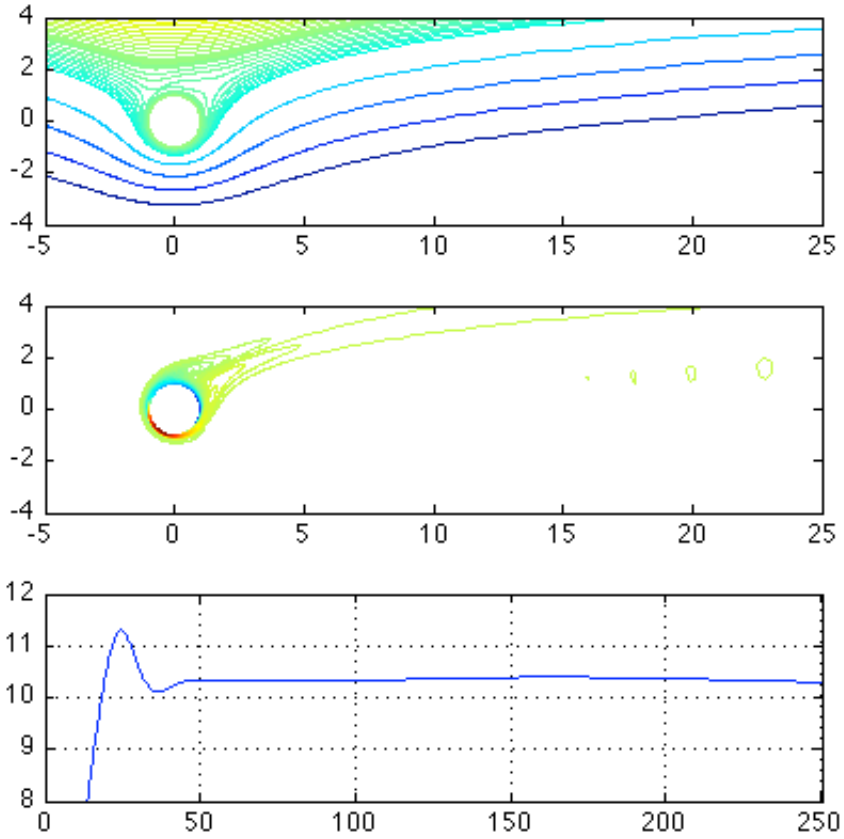

Figure 25: Vortex suppression for *Re*=200. Time-accurate solution for unsteady flow with a rotation rate of Ω=3. From top to bottom: streamlines, vorticity, temporal lift coefficient.

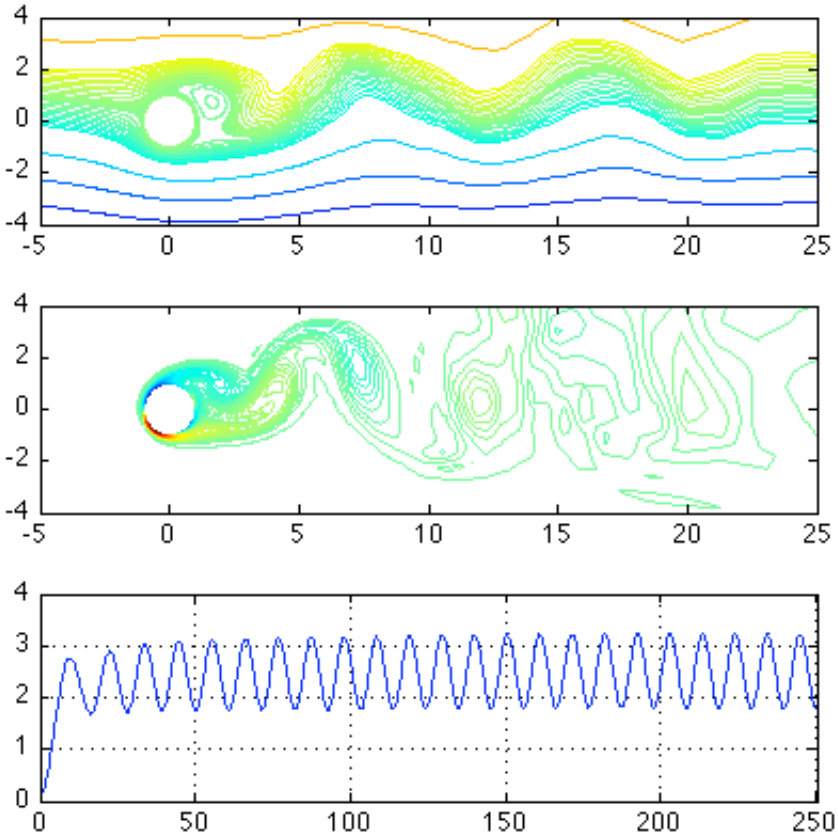

Figure 26: Time-accurate solution for *Re*=200 flow with a rotation rate of Ω=1. From top to bottom: streamlines, vorticity, temporal lift coefficient.

Behaviors of the lift and drag forces can be represented more clearly in the form of a phase diagram by plotting the lift coefficient as a function of the drag coefficient[3]. Figure 27 shows the phase diagram for Re=100. A closed loop indicates that the flow becomes fully periodic, and a singular point shows that the flow has tended to a steady state[3]. It is clear in Fig. 27 that the lift coefficient increases and the drag coefficient decreases with an increase in the rotation speed for Ω<2. This result is consistent with previous works[3]. For higher rotation rates in Fig. 27, the phase diagram resolves to singular points, and the lift coefficient continues on an increasing trend as the rotation rates increase. A second order polynomial can be fitted to the singular points in Fig. 27, which indicates that the drag coefficient varies quadratically with the lift coefficient for $2 \leq \Omega \leq 4$. The magnitudes of the lift and drag coefficients do not exactly match those of Kang et al.[3] Although they are close, the size of the loops is not as large as those of previous works. This is an indication that the amplitudes of fluctuation are larger for Kang et al.[3] Figure 28 shows the phase diagrams of the lift and drag coefficients for Re=200. The phase diagrams can be predicted by viewing the temporal lift coefficients in Fig. 21 and Fig. 22. If the lift coefficient is fully periodic by the final time for a given rotational speed, then the phase diagram will be closed. If the lift coefficient has become steady by the final time in Fig. 21 and Fig. 22, the phase diagram will result in a singular point for that rotation rate. Figures 27 and 28 are consistent with this reasoning. The results for Re=200 are in good agreement with those reported by Mittal and Kumar[9], with the exception of the higher rotation speeds. The phase diagrams of these rotation speeds do not match the previous work because of the differences between the lift coefficients. The current solver does not yield a steady lift coefficient for Ω=5.0, so the phase diagram does not resolve to a single point.

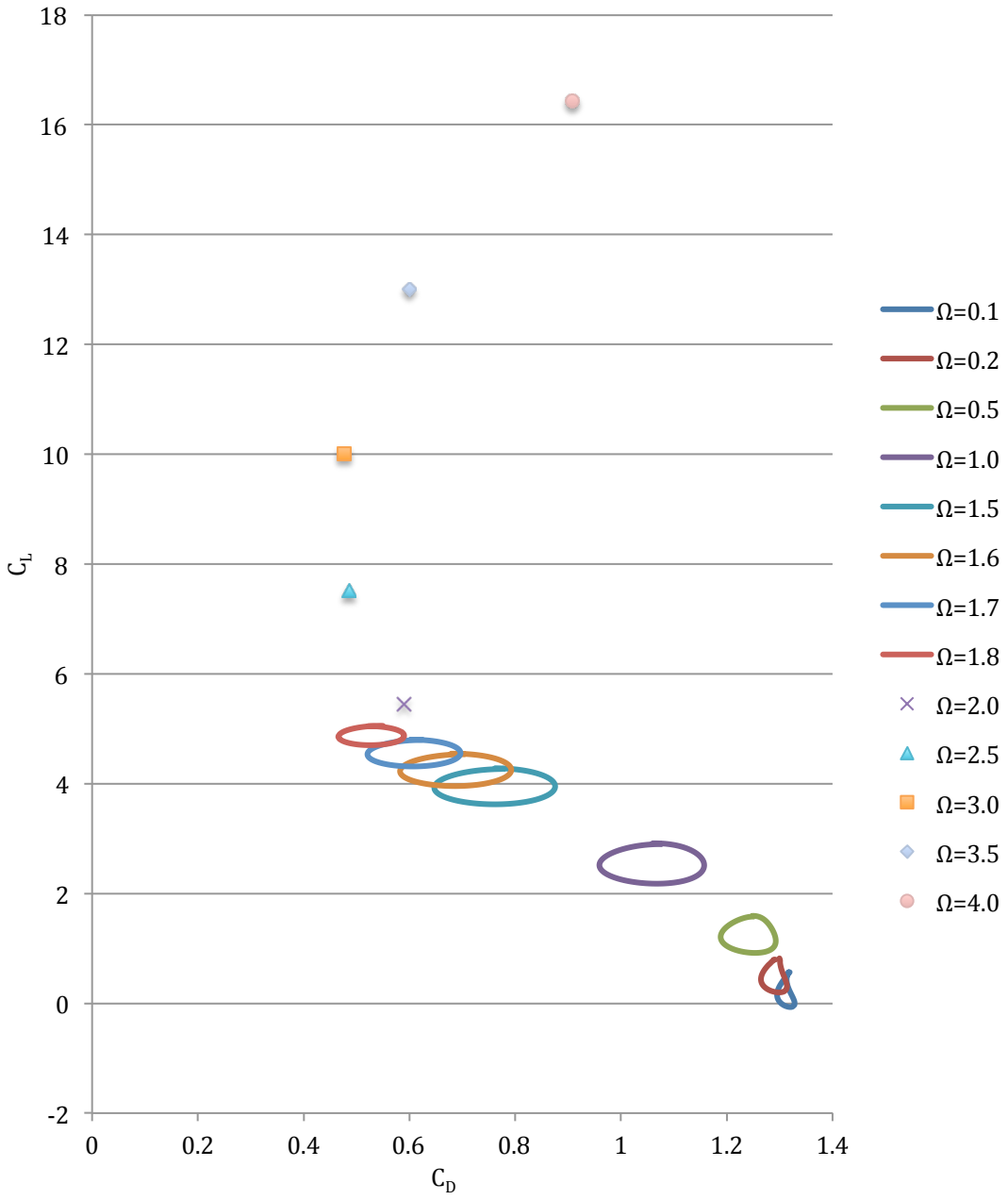

Figure 27: Phase diagram of the lift and drag coefficients for unsteady flow with various constant rotation rates. *Re*=100.

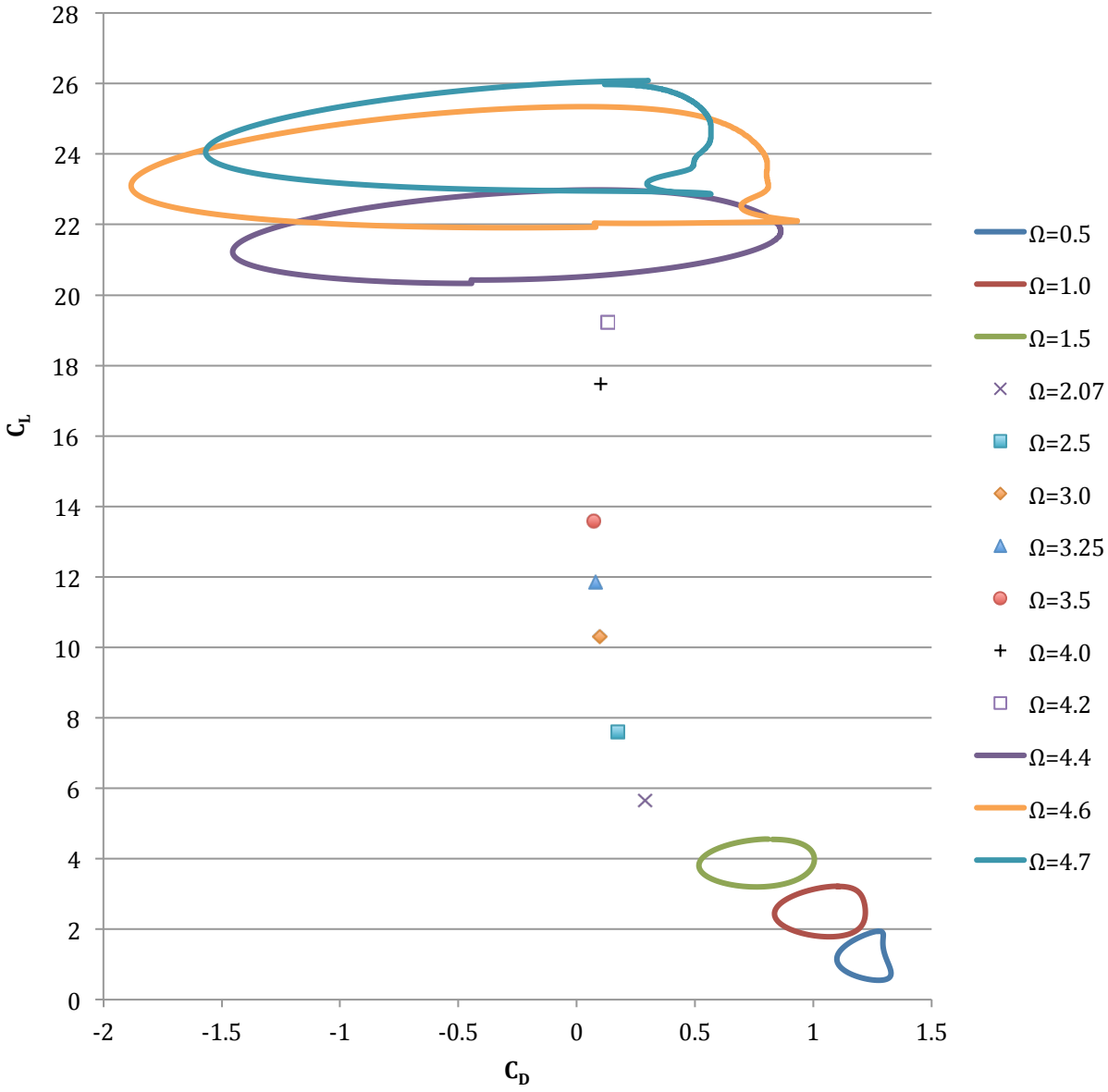

Figure 28: Phase diagram of the lift and drag coefficients for unsteady flow with various constant rotation rates. *Re*=200.

In addition to vortex suppression, lift enhancement and drag reduction are key goals for the flow over a rotating cylinder. Researchers have studied the lift enhancement gained from rotation for many years. It has long been known that the rotation generates a lifting force perpendicular to the flow direction[31]. This phenomenon is known as the Magnus effect. Due to the Magnus effect, relatively large lift coefficients can be found using high rotation rates[9]. In 1925, Prandtl[32] argued that the maximum circulation about a rotating cylinder was equal to the circulation at which the upstream and downstream stagnation points merge on the bottom of the cylinder. He stated that after this point the total circulation would be fixed at infinity[32,33]. Based on these arguments, Goldstein[34] suggested that the maximum lift coefficient generated by a rotating cylinder was limited to 4π. Glauert[35] proposed a solution to the rotating cylinder in uniform flow. The solution of the flow in the boundary layer was determined using a power series, and an expression for the circulation of the cylinder was obtained. Glauert's theory did not support Prandtl's predicted circulation limit, rather it indicated that the circulation would increase indefinitely with an increase in the rotational speed[35]. However, their assumed model for the flow was only valid for rotational speeds at which there was no flow separation[9]. Tokumaru and Dimotakis[33] also investigated the mean lift coefficient for a rotating cylinder. Their results showed that it was possible to exceed the theoretical limit; the highest rotation rate investigated led to a lift coefficient roughly 20% higher than 4π. Mittal and Kumar[9] investigated the flow over a circular cylinder for Re=200. They obtained large values of the lift coefficient for high rotation rates[9]. The results from the present study agree with these investigators. The mean lift coefficient for Re=100 and Re=200 flow are shown in Figure 29. It is clear from this figure that the lift coefficient exceeds 4π for higher rotation rates. This figure also reveals the general lift enhancement from the Magnus effect. The lift coefficient increases from the stationary value for any rotation rate investigated in the present work. The mean coefficients of lift follow the results of Kang et al.[3], who found that the lift coefficient varied linearly for $\Omega \leq 2$. Stojkovic et al.[6] investigated the effects of higher rotation rates on the flow over a rotating cylinder. They found that the linear relationship between the rotation speed and the lift coefficient does not hold for higher

rotation rates. Additionally, they saw that an increasing Reynolds number leads to an increasing lift coefficient for these higher rotational speeds[6]. The present work agrees with these results as well. Figure 29 shows the linear relationship between the mean lift coefficient and the rotation rate for $\Omega \leq 2$. Past this point, the coefficient of lift no longer follows the linear trend. Additionally, higher lift coefficients are obtained for Re=200 at the higher rotational speeds. The circular cylinder in constant rotation also experiences drag reduction. Figure 30 presents the mean drag coefficient for Re=100 and Re=200. The curves qualitatively match those of previous works[3,9]. Figure 30 indicates a drag reduction below the stationary value for all investigated rotation rates for the higher Reynolds number. However, for higher rotation speeds with Re=100, the drag coefficient increases beyond that of the stationary cylinder. Fig. 29 and Fig. 30 reveal a relationship between the goals of drag reduction and lift enhancement for a cylinder in constant rotation. There are no apparent trade-offs for the higher Reynolds number case. For all of the rotation rates investigated, drag reduction and lift enhancement occur concurrently for Re=200 flow. On the other hand, there seems to be a trade-off for Re=100 past a particular rotation rate. Lift enhancement and drag reduction occur simultaneously for $\Omega \leq 2$. However, there is an increase in the mean drag coefficient for $\Omega > 2$, while the lift coefficient continues to increase. Thus, there is a trade-off for these higher rotation rates. It is possible to achieve a lift enhancement for $\Omega > 2$, but this positive effect is combatted by a sharp increase in the drag coefficient.

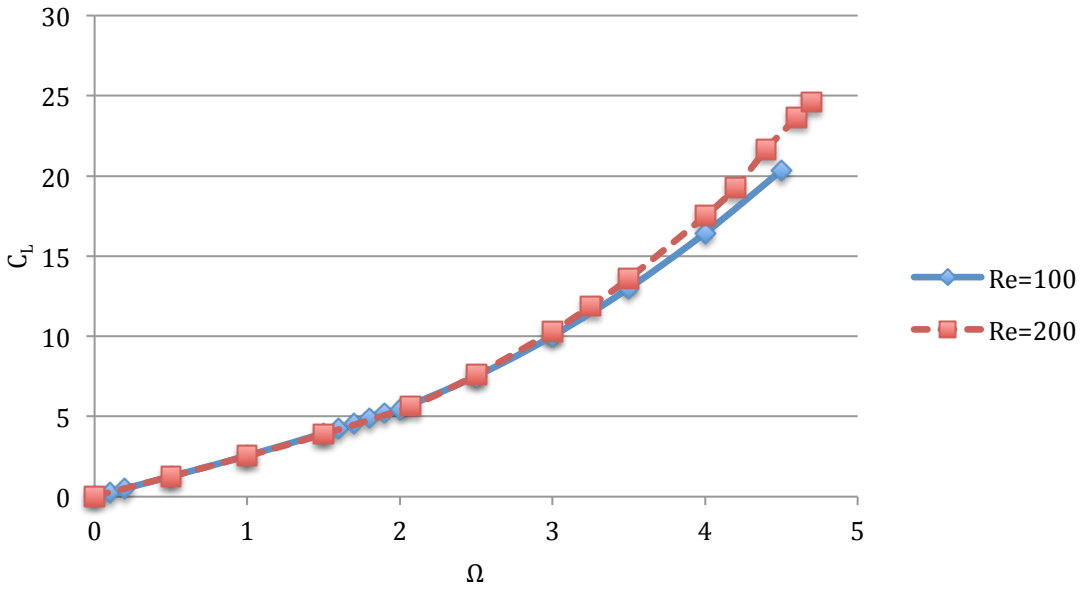

Figure 29: Effect of the rotational speed on the mean lift coefficient for a cylinder in constant rotation.

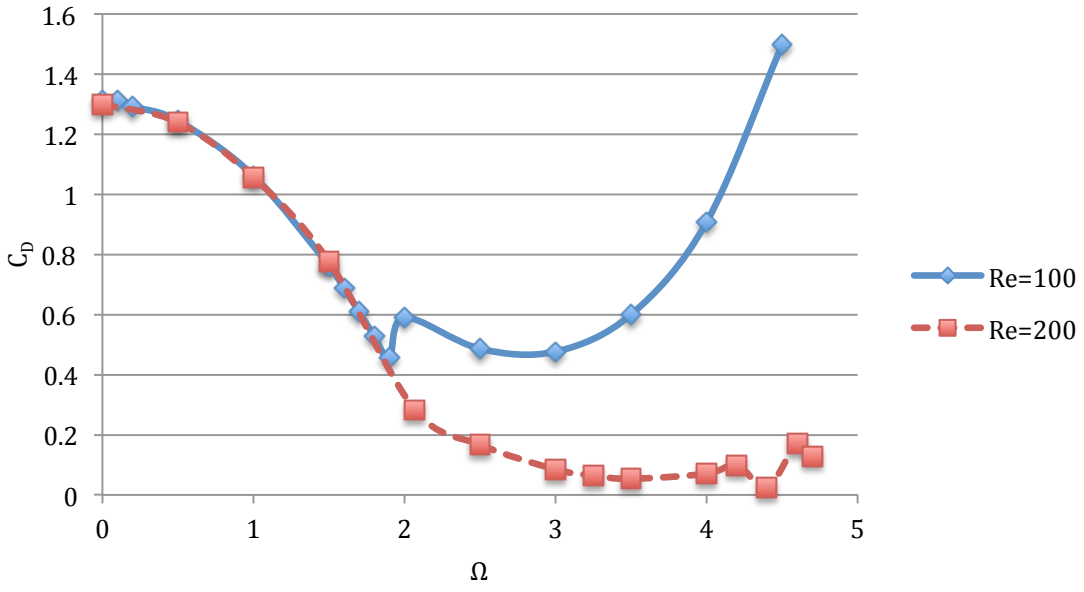

Figure 30: Effect of the rotational speed on the mean drag coefficient for a cylinder in constant rotation.

Previous works have also investigated the Strouhal number for unsteady flow with constant rotational speeds. The Strouhal number (St) can be used as a measure of the vortex shedding frequency[8]. The current work resulted in St≈0.14 and ≈0.16, respectively, for *Re*=60 and 100, which is consistent with other works[3,8]. Figure 31 shows the variation of the Strouhal number with the rotational speed. The results for *Re*=100 match those of Kang et al.[3] They suggest that the rotation of a cylinder does not significantly affect the Strouhal number in the range beneath a critical rotational speed, Ω_L. Their results showed that the Strouhal number stays nearly constant at low rotation speeds and decreases slightly as Ω approaches Ω_L. This is consistent with Badr et al.[8], who assumed that the Strouhal number is independent of the rotation speed. The trend for *Re*=60 for the time-accurate solver does not match the previous results. Instead of staying nearly constant then decreasing, the Strouhal number increases slightly with the rotation speed and then levels off to a constant. Regardless of the trend, the magnitude of Strouhal numbers are still close to those of earlier works[3,8].

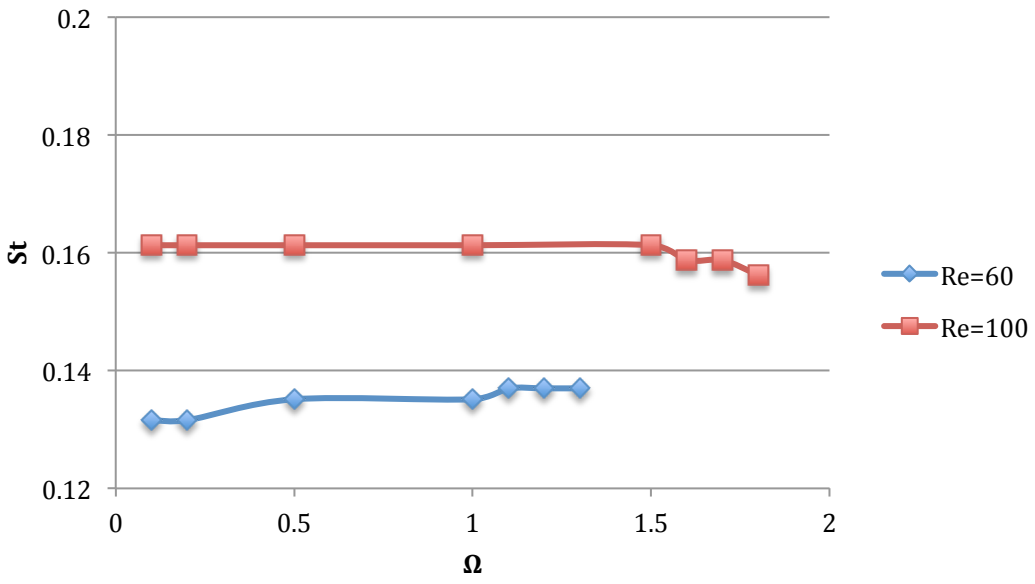

Figure 31: Variation of the Strouhal number with rotational speed.

The rotational speed has an effect on the distribution of the surface vorticity as well as the force coefficients. Figures 32 and 33 show the surface vorticity distribution with various rotation speeds for Re=60 and Re=100, respectively. As can be seen in Fig. 32 and Fig. 33, the surface vorticity is equal at θ=0° and θ=360°. The periodic boundary condition discussed in Section 3.1.3 forces this condition. In addition to this, the peak values of the vorticity on the lower (180°<θ<360°) surface increases with increasing rotation speed for both Reynolds numbers, but no such defined trend is seen for the upper surface (0°<θ<180°). Figures 32 and 33 also show that the peak values for the upper surface are higher than those on the lower surface. Note that previous works have also reached the same conclusions. Tang and Ingham[30] present the same figures for steady flow over a constantly rotating cylinder. The results from the time-accurate solver are in great agreement for Re=60. However, there are a few discrepancies for the Re=100 case. The trend is off near the periodic cut, especially for Ω=0.1. These results were taken after t=100s. It is likely that a longer amount of time was needed to develop the correct trend for the higher Reynolds number. The difference is likely not attributed to the variation of the mesh sizes. Previous works[30] have shown that the results for the surface vorticity distribution are nearly mesh independent for $\Omega \leq 1$. Kang et al.[3] presented the mean vorticities around the cylinder surface for various rotational speeds. Current results follow their trend, but the magnitudes disagree greatly. This is probably due to the fact that Kang et al.[3] used a different relation to calculate the surface vorticity than the boundary condition used in this study (see Section 3.1.3). Additionally, Fig. 32 and Fig. 33 only represent the surface vorticity at t=100s rather than the mean surface vorticity for the entire process. Fig. 32 and Fig. 33 show a negative and positive peak values at at $\theta \approx 130°$ and $\theta \approx 230°$, respectively. Additionally, a comparison between the figures reveals a higher surface vorticity for increasing Reynolds numbers. These trends are consistent with previous works[3].

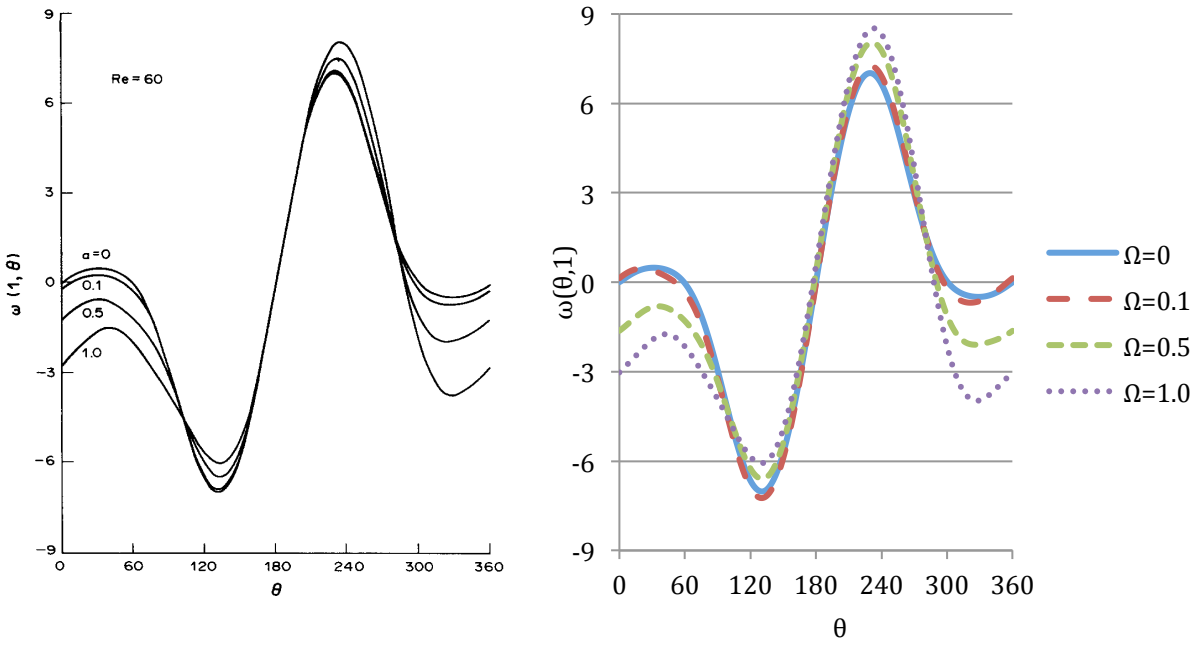

Figure 32: Effect of rotation speed on the surface vorticity distribution at *t*=100s. *Re*=60. Left: Fig. 5, Ref. [30]. Right: Current work.

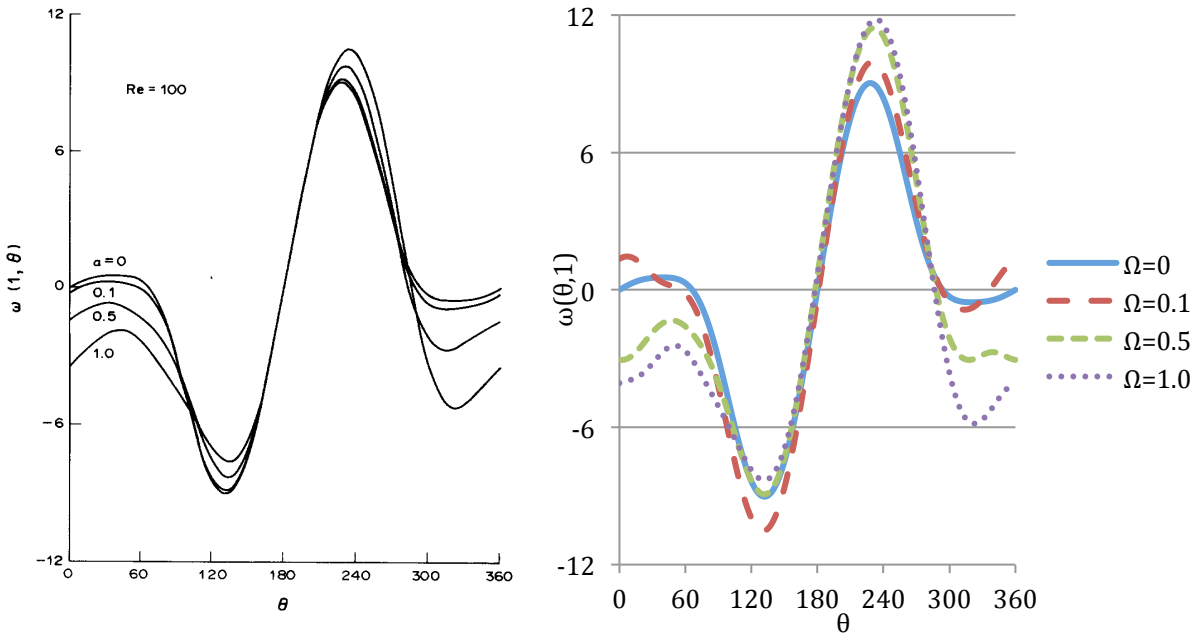

Figure 33: Effect of rotation speed on the surface vorticity distribution at *t*=100s. *Re*=100. Left: Fig. 6, Ref. [30]. Right: Current work.

The effect of the rotation speed on the surface vorticity distribution for Re=200 is shown in Figure 34. The general trend is similar to that for the lower Reynolds numbers (see Fig. 32 and Fig. 33). The magnitude of the peak value for the upper surface is greater than that of the lower surface. The peak positive value occurs in roughly the same location for all the rotation rates investigated. In contrast, the peak negative value varies with the rotational speed. These results are generally in good agreement with previous works[9]. The biggest discrepancies come from the lower rotation speeds, especially for Ω=0.5. The surface vorticity for this rotation speed should be lower than that of a stationary cylinder at the periodic cuts (θ=0°=360°). For Ω=1.5, the surface vorticity appears to level off until approximately 50°; it should gradually increase here instead. Lastly, the peak values vary slightly from the previous works. The differences are likely attributed to the time step selected for the plot. The previous works plotted the surface vorticity for steady-state solutions, whereas Figure 34 is the surface vorticity at the final time from the solver. Taking into account that the lower rotation rates are fully periodic by 250 s, it is likely that an average surface distribution over a complete period would have yielded even better results for these speeds.

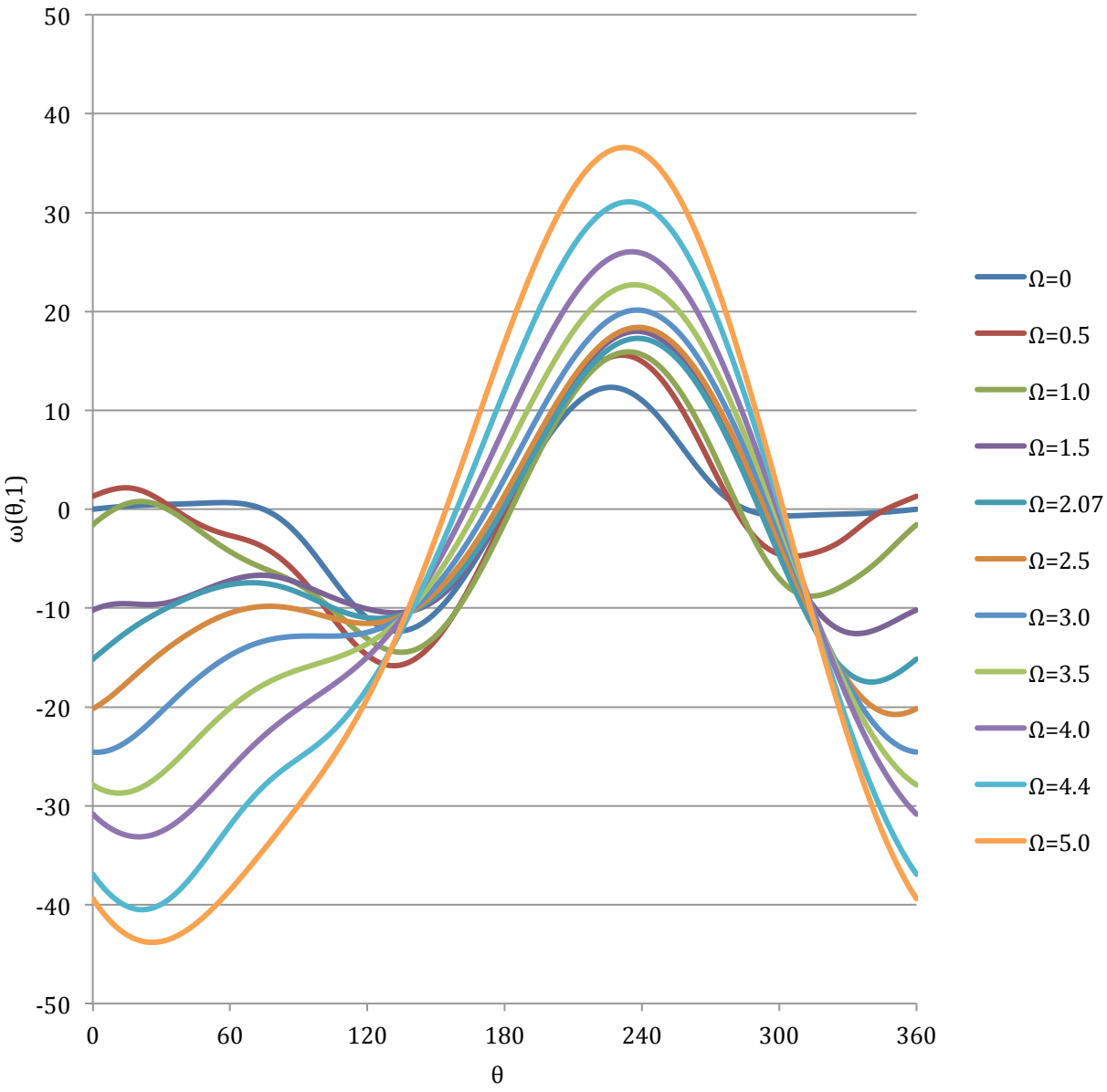

Figure 34: Effect of rotation speed on the surface vorticity distribution at *t*=250s. *Re*=200.

Periodic Rotation

Flow past a rotationally oscillating cylinder has grasped interest in the literature where the focus was to control the vortex shedding in the bluff body wake. Among the many control methods mentioned in Ch.1, rotary oscillation "may effectively modify the wake structure under some resonant circumstances built from the interactions between the rotary oscillation and natural vortex shedding"[4]. The flow around a rotationally oscillating cylinder is controlled by two forcing parameters: the maximum rotational speed and the forcing oscillation frequency. These are given in Eq. (89) below.

$$\Omega = \frac{\dot{\theta}_{max} d}{2u_\infty}$$
$$St_d = \frac{f_f d}{u_\infty} \tag{89}$$

In this work, the cylinder is forced into oscillatory rotation according to the following relation

$$u_{rot}(t) = \Omega \sin(2\pi St_d t) \tag{90}$$

The flow behind the rotationally oscillating cylinder can be categorized into two regions depending on its rotational speed and forcing frequency. These two categories are known as the lock-on and non lock-on regions. The flow is in the lock-on region if the vortex shedding matches the forcing frequency; if this does not occur, the flow is non lock-on[4]. Choi, et al.[4] performed an in depth investigation of the effect of these parameters on the two regions. Their work can be reviewed in Ref. [4]. The flow regimes determined by Choi et al.[4] were used as a guide for the many periodic rotation cases considered in this work. However, there were some discrepancies, and the lock-on and non lock-on regions for the rotationally oscillating cylinder according to the present solvers are shown in Figure 35. This flow regime was determined using both the time-accurate and the harmonic balance solvers. As seen in Figure 35, the non lock-on regime for the present work occurred for

slightly lower Strouhal numbers. The few discrepancies can likely be attributed to differences in mesh size and applied boundary conditions. Once again, the flow is considered to be in the lock-on region if the vortex-shedding frequency matches up with the forcing frequency during the simulation. If the frequencies do not match, then the flow is considered to be in the non lock-on region. This can be determined by inspection of the temporal lift coefficient. If the lift coefficient is periodic with only one frequency, then the flow is lock-on. If there is clearly more than one frequency displayed in the temporal lift coefficient, then the flow is non lock-on. This is clear in Figures 36 and 37, where Fig. 36 shows a lock-on case and Fig. 37 presents a non lock-on case. The flow region can also be determined with the use of a Fast Fourier Transform (FFT) on the temporal lift coefficient. As one can see in Figures 38 and 39, this transformation reveals the frequencies in the lift coefficient. Figure 38 shows the FFT for the lock-on case presented in Fig. 36. There is only one spike in the frequency, which indicates that the shedding frequency has matched the forcing frequency of the cylinder (St_d). In contrast, the FFT for the non lock-on case (see Fig. 37) is shown in Figure 39. The transform reveals two peaks in the lift coefficient for this non lock-on case. As the frequencies have not locked-on, one peak matches the forcing frequency (St_d); the other reveals the vortex shedding frequency.

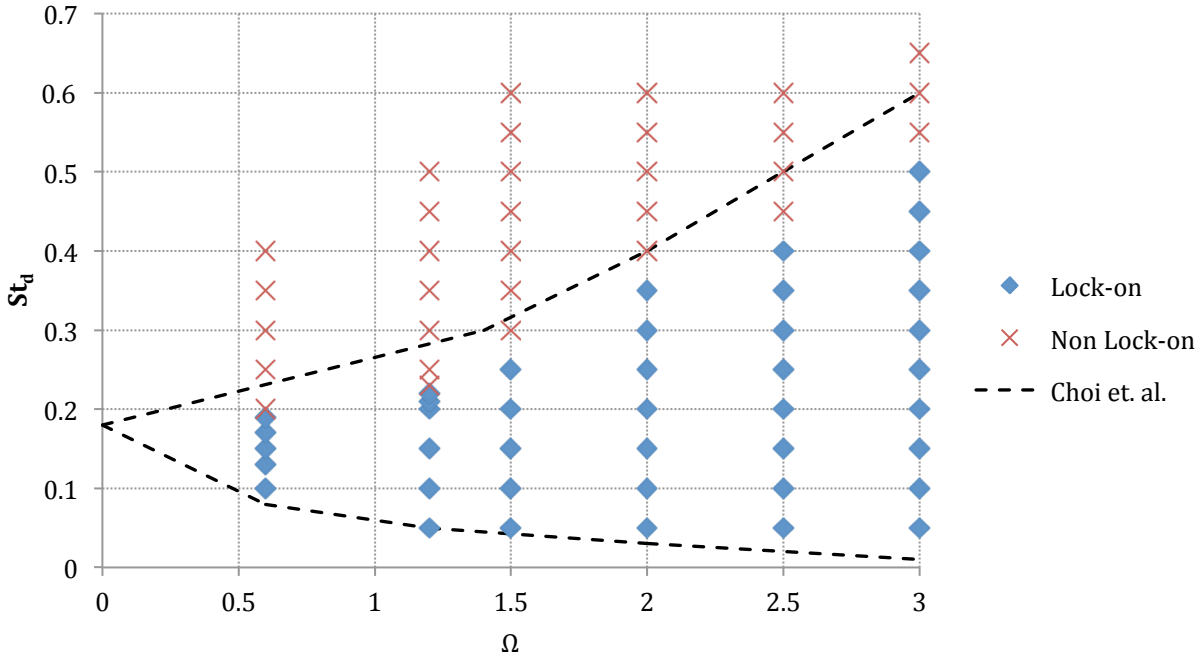

Figure 35: Present results for the flow regime of a rotationally oscillating cylinder. The dashed line represents the delineation between the lock-on and non lock-on regions from previous works[4].

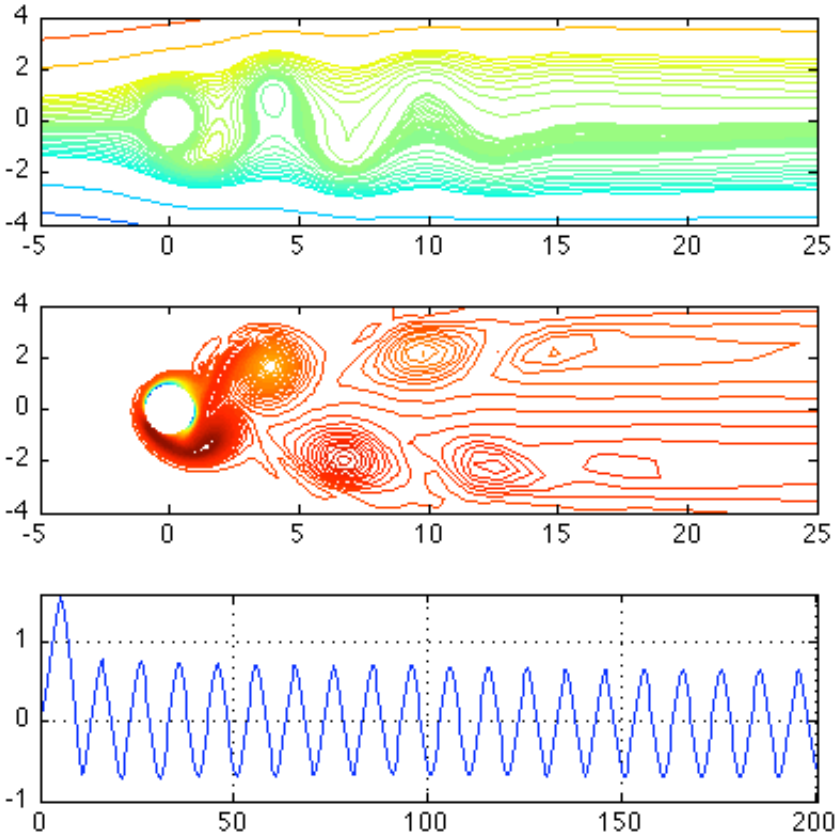

Figure 36: Time-accurate solution for a rotationally oscillating cylinder in the lock-on region. Re=100, Ω=1.5, St_d=0.2. From top to bottom: streamlines, vorticity, temporal lift coefficient.

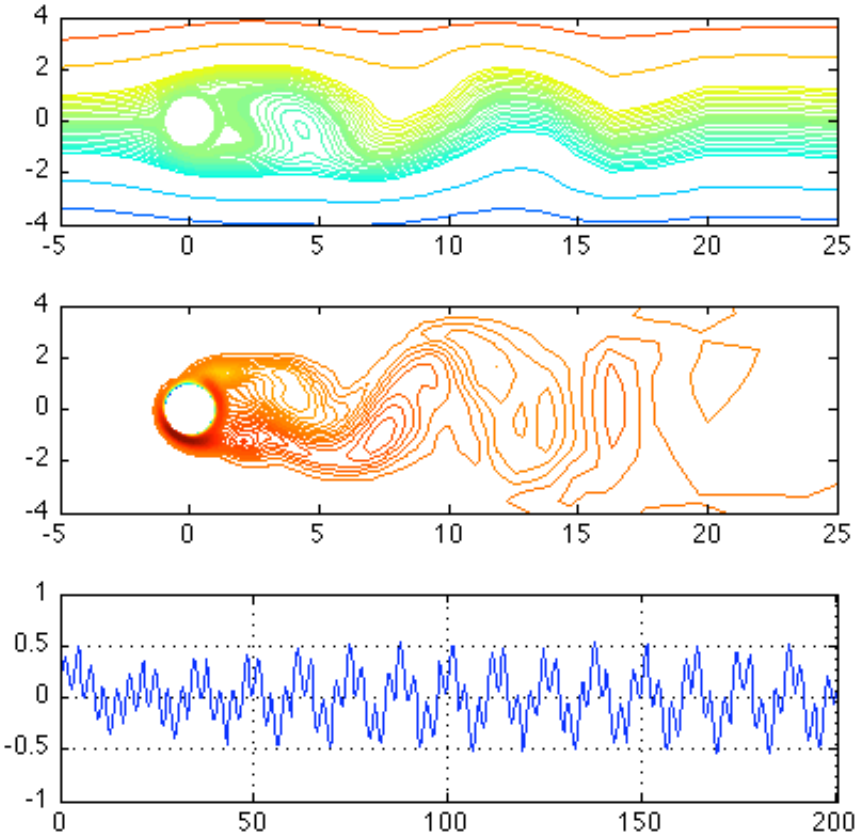

Figure 37: Time-accurate solution for a rotationally oscillating cylinder in the non lock-on region. Re=100, Ω=1.5, St_d=0.6. From top to bottom: streamlines, vorticity, temporal lift coefficient.

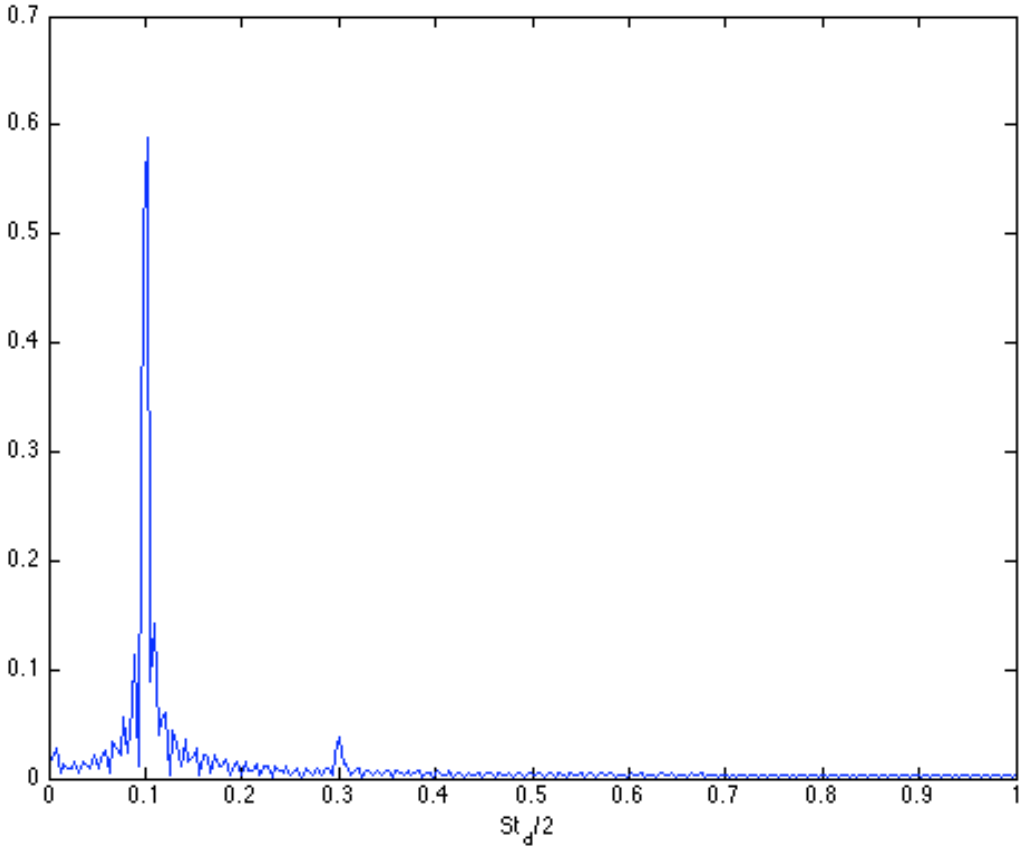

Figure 38: Fast Fourier Transform of the temporal lift coefficient in the lock-on region. Re=100, Ω=1.5, St_d=0.2.

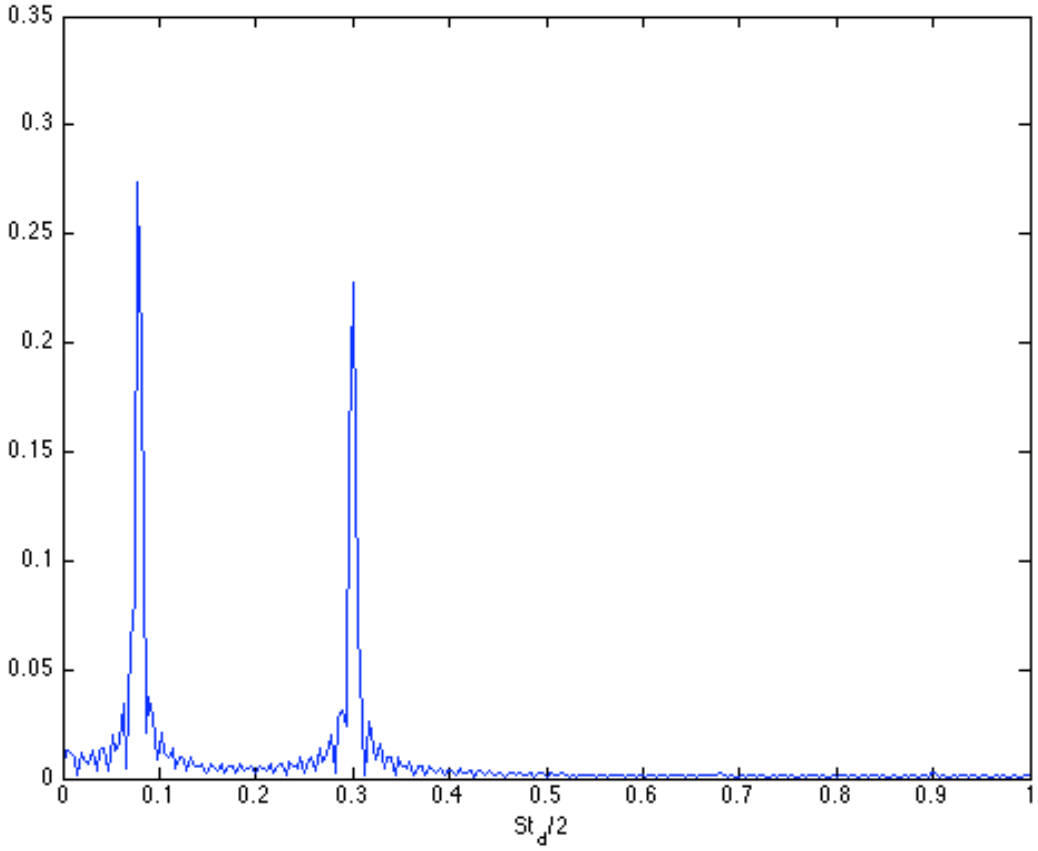

Figure 39: Fast Fourier Transform of the temporal lift coefficient in the non lock-on region. Re=100, Ω=1.5, St_d=0.6.

4.2.2 Harmonic Balance Method

As discussed in Section 3.2.2, the harmonic balance method is especially useful for temporally periodic flows. Rather than marching through a specified amount of time steps, the harmonic balance method involves the solution of the flow field at sub-time levels. The temporal periodicity of the flow is hence used to gather snapshots of the flow at different sub-time levels over a single period. The harmonic balance method as described in Section 3.2.2 only converges when there is one fundamental frequency in the problem. Because of

this constraint, the harmonic balance solver was only used to consider rotationally oscillating cylinders in the lock-on region as prescribed by Fig. 35. Thus, the forcing parameters and applied periodic rotation are the same as those discussed in Section 4.2.1 (see Eq. (89) and Eq. (90)). The results from the harmonic balance solver can be directly compared to lock-on solutions from the time-accurate solver in Section 4.2.1. Figures 40, 41, and 42 show the streamlines, vorticity contours, and force coefficients of a harmonic balance solution, respectively. The figures show seven sub-time levels, which are equally spaced over one oscillation period. The discrete points in Fig. 42 represent the harmonic balance solution for the force coefficients for each sub-time level, while the line is an interpolated curve between the sub-time levels. Equation 76 is used for this interpolation (see Section 3.2.2). The same periodic case for the time-accurate solver was shown in Figure 36. The lift coefficients from the harmonic balance solution are compared to the time-accurate solver in Figure 43. This figure shows that the solutions from the two solvers are in good agreement. However, the computational cost varies greatly between the time-accurate solver and the harmonic balance approach. Previous investigators determined that the harmonic balance method scaled computational cost nearly linearly with the number of sub-time levels used in the solution[15,17,18]. If inner iterations are used to drive down the residual in the time-accurate solver, then the code becomes very computationally expensive. The runtimes for this solver are overnight versus three hours for the harmonic balance method.

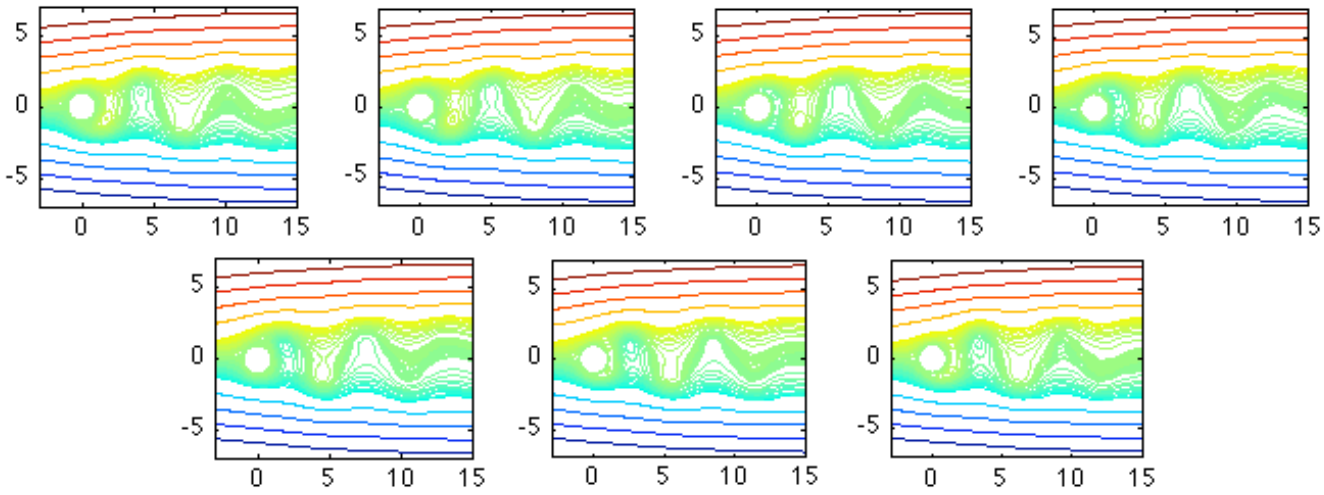

Figure 40: Streamlines of the harmonic balance solution in the lock-on region for 7 sub-time levels. Re=100, Ω=1.5, St_d=0.2.

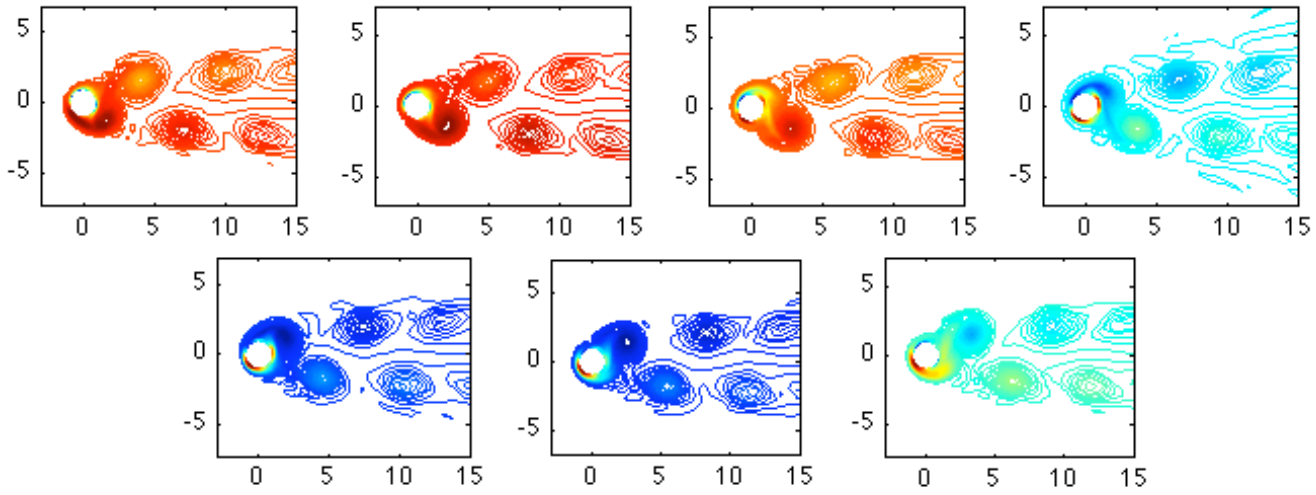

Figure 41: Vorticity contours of the harmonic balance solution in the lock-on region for 7 sub-time levels. Re=100, Ω=1.5, St_d=0.2.

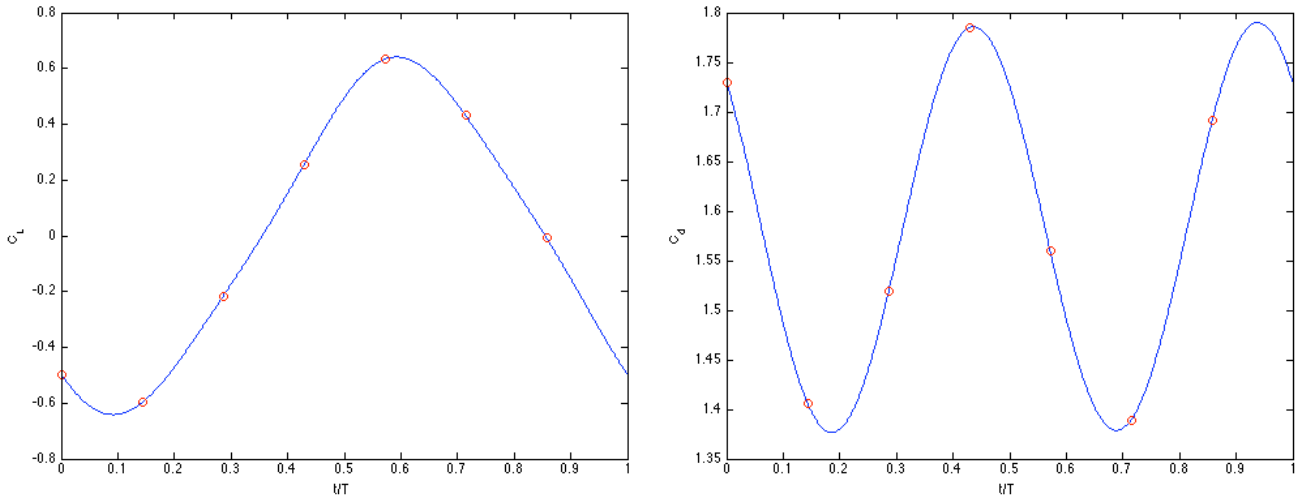

Figure 42: Force coefficients of the harmonic balance solution in the lock-on region for 7 sub-time levels. Left: Lift coefficient. Right: Drag coefficient. Re=100, Ω=1.5, St_d=0.2.

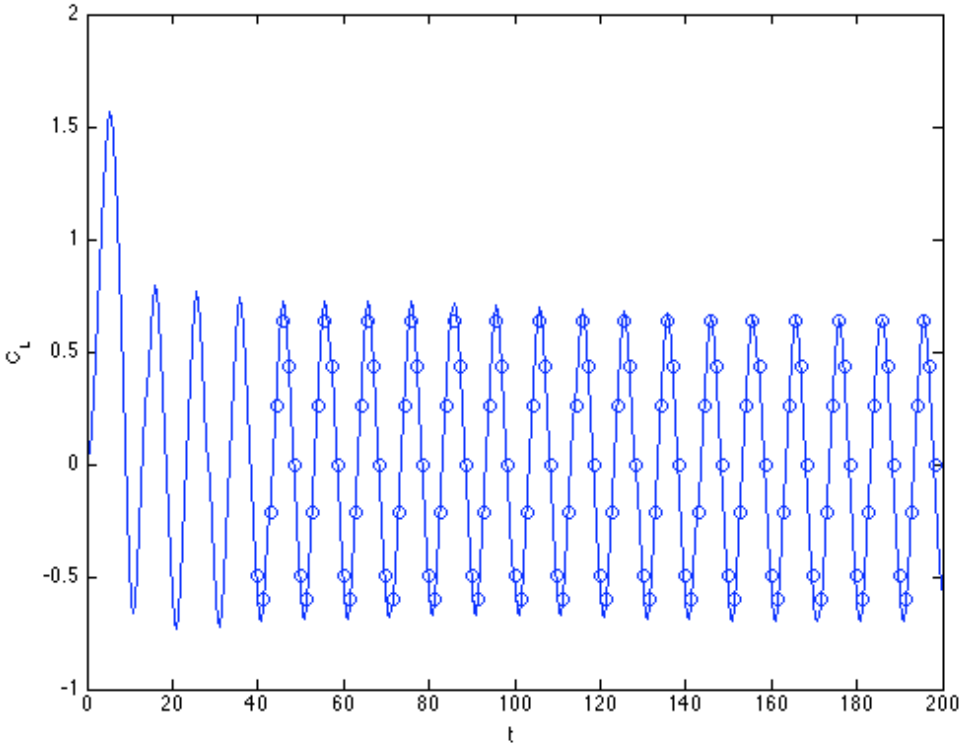

Figure 43: The coefficient of lift from the harmonic balance solver ('o') compared to the temporal lift coefficient from the time-accurate solution ('-'). Re=100, Ω=1.5, St_d=0.2.

Many previous investigators have studied the effects of periodic rotation on the force coefficients of the cylinder. Protas and Wesfried[36] investigated the mean drag coefficient as a function of the Strouhal number for *Re*=150. They did not see a drag reduction beneath that of the uncontrolled flow, and thus posed the theoretical question of whether this feat was possible. When looking at previous works, it becomes clear that drag reduction beneath the stationary value is possible and has been observed in the past[4,11,12,13,37]. Choi et al.[4] found that the drag forces reach a local minimum near the boundary between the lock-on and non lock-on regions. Cheng et al.[13] saw a drag reduction below that of the stationary cylinder for a flow of *Re*=200. Tokumaru and Dimotakis[11] performed experiments to investigate the effects of forced rotary oscillations for flow at a Reynolds number of 15,000. They saw a decrease in the drag coefficient by a factor of 6 compared to the unforced case. Shiels and Leonard[12] performed computational simulations to verify previous experimental results. They suggested that a forced oscillatory control is most efficient at higher Reynolds numbers. A slight drag reduction beneath the stationary value was achieved in this work even though lower Reynolds numbers were used. The harmonic balance solver was validated against the experimental results of Thiria, Goujon-Durand, and Wesfried[37], who showed a drag reduction beneath the stationary value for *Re*=150. Thiria et al.[37] used two non-dimensional forcing parameters: the forcing amplitude (A) and the frequency ratio f_f/f_0. The natural frequency of vortex shedding (f_0) was given as 0.98 Hz for *Re*=150. The Strouhal number and rotational speed are the two parameters used in the harmonic balance solver. The forcing frequency was determined with a specific ratio, and the corresponding Strouhal number was determined using Eq. (89). The maximum rotational speed (Ω) was chosen to match the forcing amplitude (A) in the previous work. In these cases, the rotation of the cylinder was imposed by

$$u_{rot} = \Omega \cos(2\pi St_d t) \tag{91}$$

Figure 44 shows the normalized mean drag coefficients for various frequency ratios plotted with the results of Thiria et al.[37], where C_{D0} is the mean drag coefficient of the stationary

cylinder. For the most part, the drag ratios match the experimental results. The largest discrepancies occur at f_f/f_0=0.8, 5.0. In these instances, the computational results do not fall within the error bars set by Thiria et al.[37] It is possible that the harmonic balance solver does not completely resolve the complexity of the flow field at these ratios. Despite the discrepancies in the results, it is clear that drag reduction is accomplished for *Re*=150. For frequency ratios greater than 2, the coefficient of drag is reduced beneath that of the stationary value. It should also be noted that, in contrast to the experimental results, the harmonic balance solver does not find a local minimum around f_f/f_0≈3.5. This fact will be re-visited in Section 4.3.2. The vorticity contours from the harmonic balance solver can be compared to the flow visualizations of Thiria et al.[37] Figures 45 and 46 show this comparison for f_f/f_0=1.5 for two harmonic balance sub-time levels near the half-period. In both cases, the vortices are being shed alternatively off the cylinder. Figures 47 and 48 show the flow visualizations for a higher frequency ratio. Figure 47 shows the vorticity contour for the first harmonic balance sub-time level, while Fig. 48 shows a sub-time level near the half-period. The vorticity contours are very graphically similar to the experimental results at this frequency ratio.

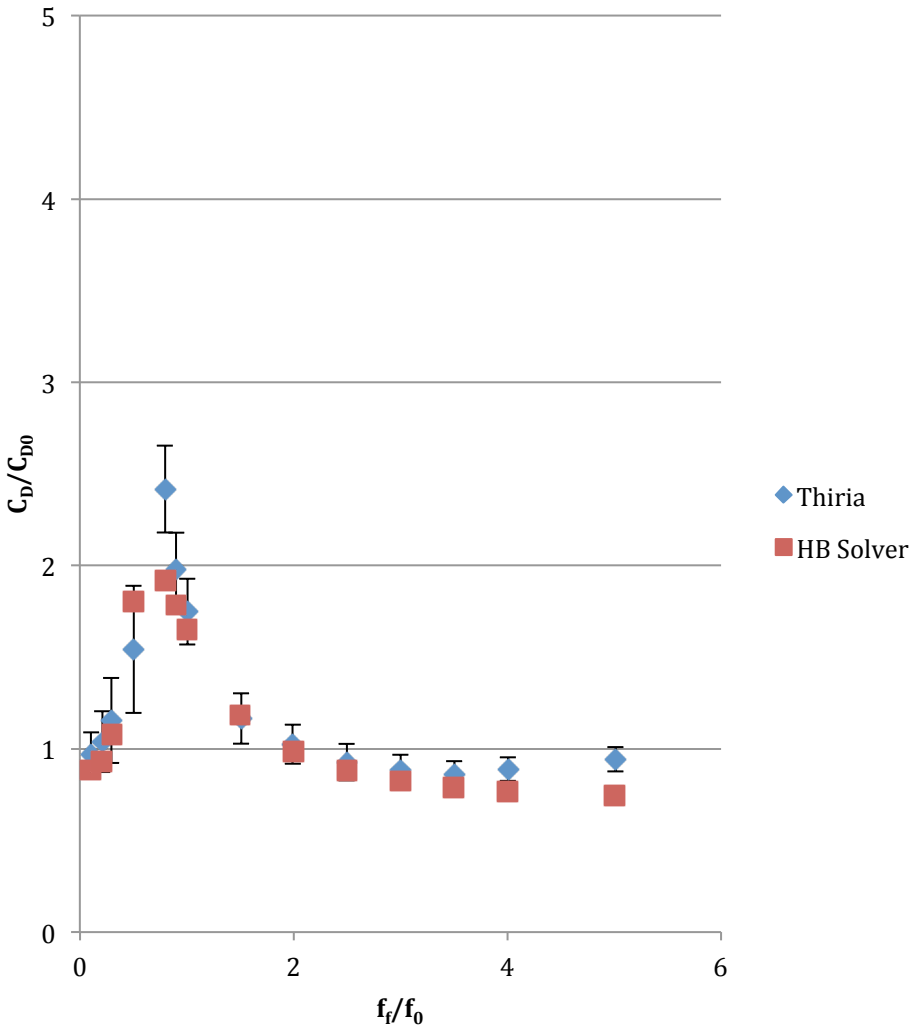

Figure 44: Validation of harmonic balance solver with experimental results of Thiria et al.[37] Re=150. Ω=2.

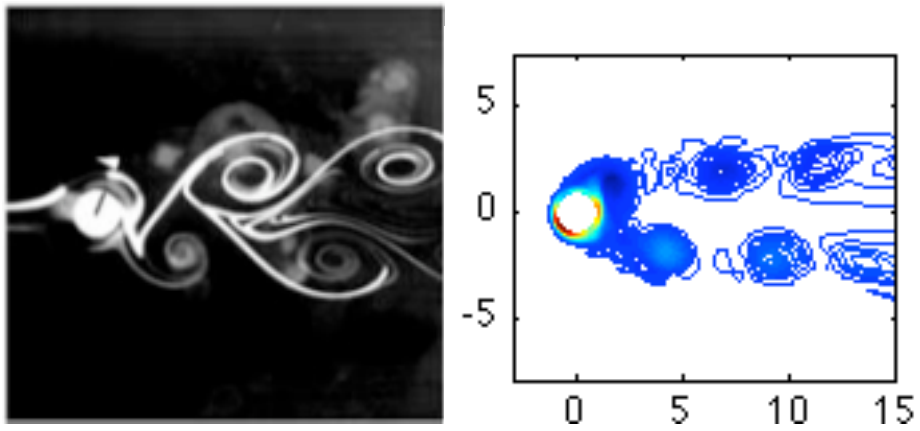

Figure 45: Comparison of unsteady flow field for Re=150. Ω=2, f_f/f_0=1.5. Left: Experimental results[37] at $t=T/2$. Right: Harmonic balance solver at $t=4T/7$.

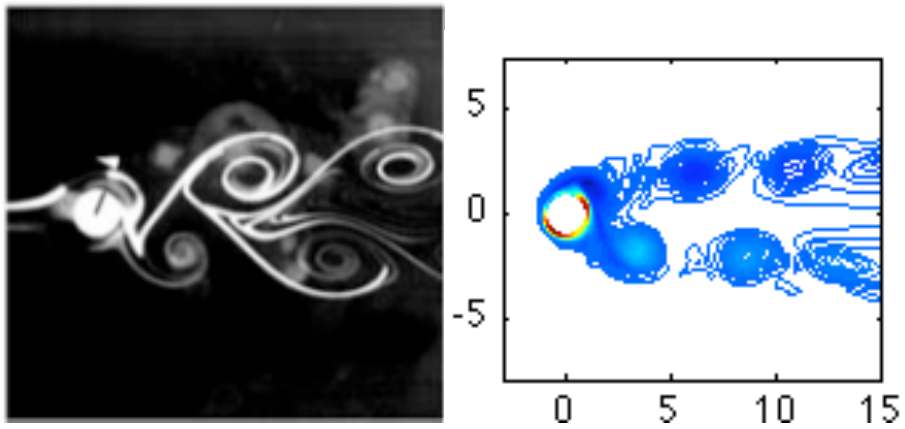

Figure 46: Comparison of unsteady flow field for Re=150. Ω=2, f_f/f_0=1.5. Left: Experimental results[37] at $t=T/2$. Right: Harmonic balance solver at $t=3T/7$.

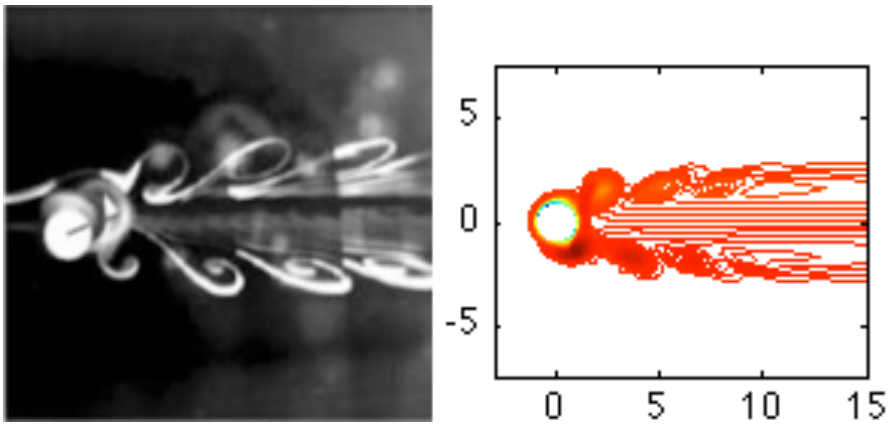

Figure 47: Comparison of unsteady flow field for Re=150. Ω=2, f_f/f_0=3.0. Left: Experimental results[37] at $t=T/6$. Right: Harmonic balance solver at $t=T/7$.

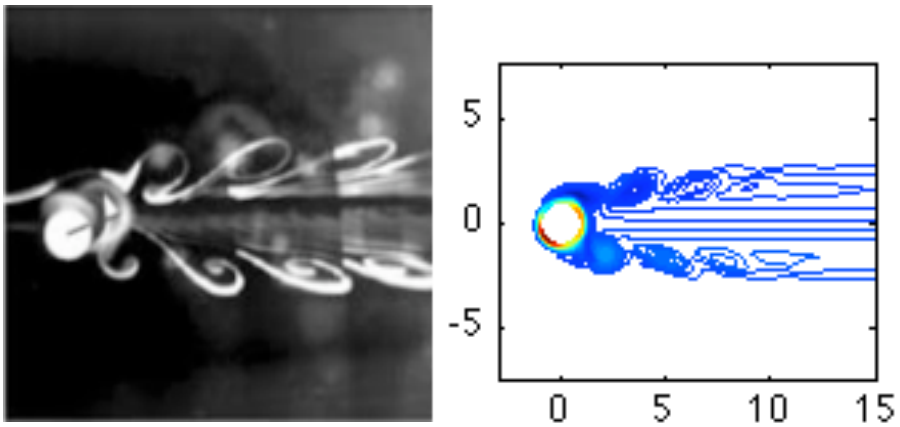

Figure 48: Comparison of unsteady flow field for Re=150. Ω=2, f_f/f_0=3.0. Left: Experimental results[37] at $t=T/2$. Right: Harmonic balance solver at $t=4T/7$.

The relationship between the mean drag coefficient and the Strouhal number was investigated for *Re*=100 at various rotational speeds. During this investigation, a sweep of the forcing frequencies (St_d) was performed for chosen rotational speeds (Ω). Because these runs were performed using the harmonic balance method, only frequencies from the lock-on region were considered (see Fig. 35). The Strouhal number was normalized with the natural vortex shedding frequency (St_0) for *Re*=100 flow, while the mean coefficient of drag was normalized with the stationary value determined from the harmonic balance solver. In this stationary case, the rotational speed was set to zero and the Strouhal number was set to the natural vortex shedding frequency. The cylinder was rotated for the first 20 iterations to trigger the vortex shedding. Once the cylinder was stationary, the vortices locked on to the natural vortex shedding frequency, and the stationary mean drag coefficient was determined from the harmonic balance solution. These drag coefficient results are shown in Figure 49. Only a slight drag reduction beneath the stationary value was observed for Re=100 at the higher rotation rates.

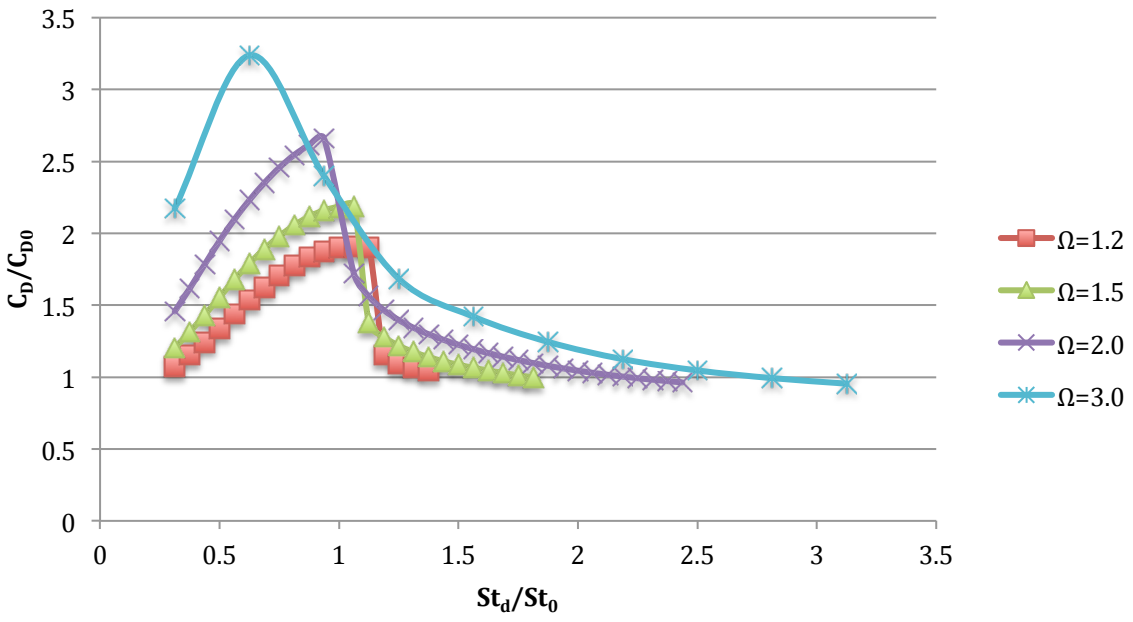

Figure 49: Effect of the forcing frequency on the mean drag coefficient in the lock-on region for *Re*=100.

Previous works analyzed the relationship between the mean drag coefficient and the forcing frequency for a cylinder in rotary oscillation[4,13]. Choi et al.[4] saw a maximum in the mean drag coefficient near $St_d \approx St_0$ and a sharp decrease in the force coefficient with an increasing forcing frequency. The results in Figure 49 agree with this trend. The maximum value occurs in the vicinity of $St_d/St_0 \approx 1$ for the lower rotation rates. Fig. 49 also shows that the maximum occurs at lower forcing frequencies for higher rotation rates. As the rotational speed increases, the maximum value not only increases in magnitude but also occurs closer to the lower boundary of the lock-on region. Past the peak drag coefficient, there is a sharp decrease with increasing forcing frequencies towards the upper boundary of the lock-on region. These trends in Fig. 49 agree with the previous works[4,13]. Choi et al.[4] also observed a local minimum in the mean drag coefficient near the boundary between the lock-on and non lock-on regions. Past this local minimum, they observed a gradual increase in the force coefficient with increasing forcing frequencies in the non lock-on region. This effect was investigated in the present work with the time-accurate solver. The harmonic balance solver was used to investigate the mean drag coefficient in the lock-on region. Once the upper boundary of the region was reached, the time-accurate solver was used to investigate the mean drag coefficient in the non lock-on region. Figure 50 shows the relationship between the mean drag coefficient and the forcing frequency across the lock-on region boundary. For this rotational speed, the minimum occurs in the non lock-on region. The drag coefficient gradually increases with increasing forcing frequencies past the local minimum.

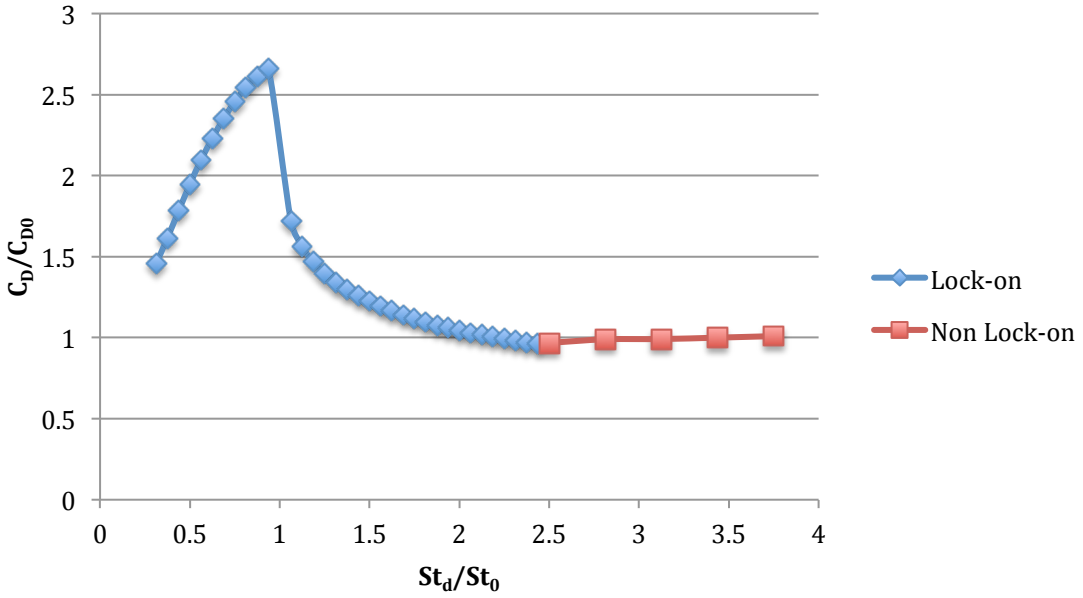

Figure 50: Effect of the forcing frequency on the mean drag coefficient across the lock-on region boundary. *Re*=100, Ω=2.0.

Previous investigators have discussed the distribution of the lift coefficient amplitude, for various rotation rates[14,38]. Baek and Sung[14] investigated the flow over a rotationally oscillating cylinder of *Re*=110, while Lu[38] examined the flow for *Re*=300. Both works found that the maximum lift coefficient for a cylinder in periodic rotation was greater than that of the stationary case. Lu[38] found that the peak lift coefficient corresponds approximately to the natural shedding frequency. However, Baek and Sung[14] saw that the maximum lift coefficient occurred at slightly lower frequencies as the rotational speed was increased. Figure 51 shows the distribution of the maximum lift coefficient in the lock-on region for various rotational speeds. The previous works only investigated the maximum lift coefficient for lower Strouhal numbers. The harmonic balance results qualitatively match the previous works for the lower frequencies. The results agree with the work of Baek and Sung[14] as the peak values occur at lower Strouhal numbers for increasing rotational speeds. Additionally, the maximum lift coefficients increase as the rotation rate

is increased. The harmonic balance results indicate a sharp decrease in the maximum lift coefficient near $St_d/St_0 \approx 1$. Following this sharp decrease, the peak coefficient tends towards the stationary value as the Strouhal number increases. The peak coefficient gets closer to the stationary maximum lift for higher rotation rates. In all cases, Fig. 51 indicates a clear lift enhancement over the stationary value for lower forcing frequencies.

Figures 49 and 51 reveal a trade-off when considering the goals of lift enhancement and drag reduction for a rotationally oscillating cylinder. If the ultimate goal is lift enhancement, then drag reduction beneath the stationary value will not be achieved. According to Figure 51, the best frequencies to achieve lift enhancement would be those below $St_d/St_0 \approx 1$. However, drag reduction beneath the stationary value does not occur below this frequency ratio (see Fig. 49). The opposite is true for the goal of drag reduction. The drag reduction is greatest at the boundary between the lock-on and non lock-on regions. Unfortunately, this is also where the lift enhancement is the lowest.

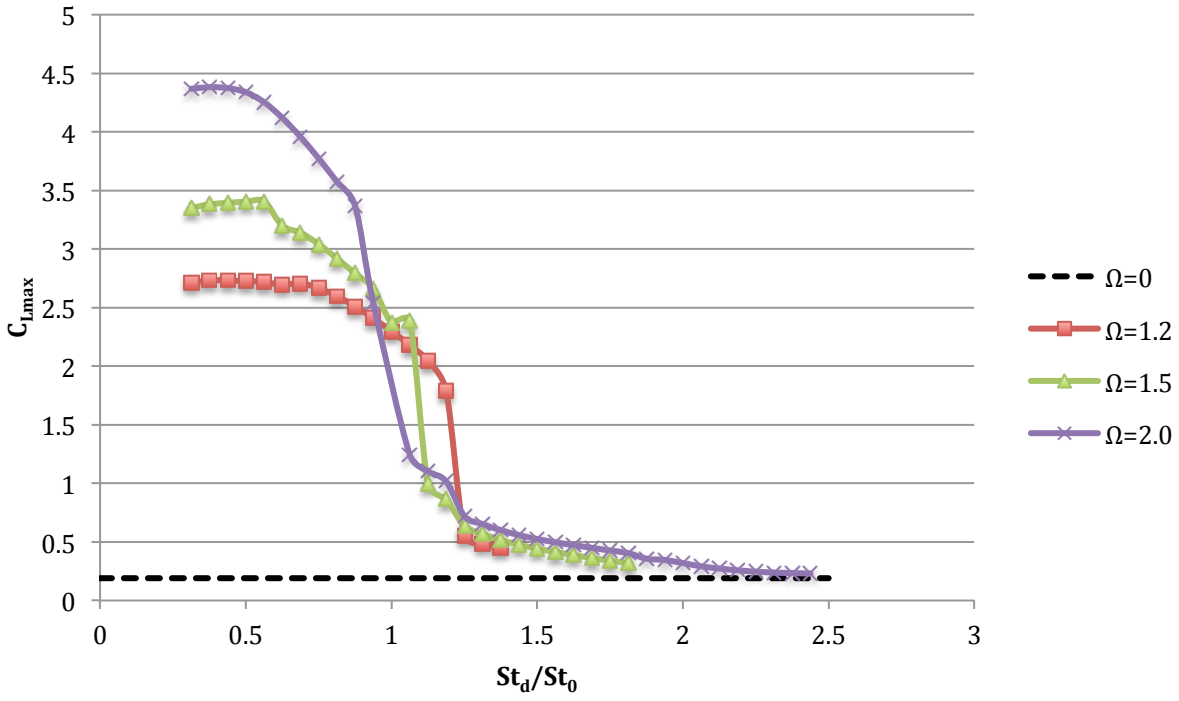

Figure 51: Distribution of the maximum lift coefficient in the lock-on region for *Re*=100.

4.3 Sensitivity Analysis

A finite difference sensitivity analysis was conducted with the harmonic balance solver for a periodically oscillating cylinder in this work. The mean coefficient of drag was chosen as the objective function, and the Strouhal number was the investigated design variable. The goal was to use finite difference sensitivity analysis to determine a value of the Strouhal number, which resulted in a reduced mean drag coefficient. The sensitivity analysis was performed with two iterative techniques: Newton's method and the Steepest Descent approach. The general process for the sensitivity analysis was discussed in Section 3.3. For both of these iterative techniques, an initial Strouhal number was chosen, and the drag coefficients and the sensitivity information were determined through a harmonic balance solution. The iterative solution should continue until the drag coefficient is minimized. However, neither approach converged to a minimum drag coefficient with the harmonic balance solver.

4.3.1 Newton's Method

Tables 3 and 4 show the results of the sensitivity analysis using Newton's method. For each case analyzed, the drag coefficient continued to decrease for increasing forcing frequencies until the Strouhal number was in the non lock-on region. As discussed in Section 4.2.2, the harmonic balance solver cannot converge for a flow field with multiple frequencies. Thus, the sensitivity analysis was approaching a minimum. However, it eventually led to a Strouhal number in the non lock-on region at which point the harmonic balance solver diverges. The relationship between the mean drag coefficient and the Strouhal number was investigated for Re=100 at various rotational speeds in Section 4.2.2. During the investigation, a sweep of the Strouhal numbers was performed for chosen rotational speeds. Figures 52 and 53 show the Newton's method sensitivity results imposed on the sweeps for the two rotational rates considered. Figures 52 and 53 also show the relationship between the mean drag coefficient and the forcing frequency across

the boundary of the lock-on and non lock-on regions as seen in Section 4.2.1. It was determined that a minimum drag coefficient occurs near the boundary between these regions or in the non lock-on region. The hope was that the sensitivity analysis would converge to a minimum near the boundary but not make the jump into the non lock-on region. Relaxation was used to try to attain this. However, the results show that the non lock-on region was reached for both cases investigated. Although the Newton's method implementation was not converging to the minimum mean drag coefficient, the accuracy of the analysis was checked visually by imposing the calculated slope onto the sweeps performed in Section 4.2.2. Figure 54 shows the slope from the first iteration of the sensitivity analysis imposed on the sweep of the mean drag coefficient for Ω=1.2. This visual investigation shows agreement between the sensitivity analysis and the sweep information.

Table 3: Sensitivity analysis using Newton's method with relaxation. Input parameters: Ω=1.2, St_d=0.2, R=0.4.

i	$St_d(i)$	$C_D(i)$	$C_D'(i)$	$C_D''(i)$	$St_d(i+1)$
1	0.2000000	1.4066794	-5.8254735	-9128708.9	0.1999997
2	0.1999997	1.4062244	-5.8255056	125.740209	0.2185316
3	0.2185316	1.3387919	-2.8308257	57.8213166	0.2381148
4	0.2381148	1.2914174	-2.0789944	30.7721514	0.2651392

Table 4: Sensitivity analysis using Newton's method with relaxation. Input parameters: Ω=3.0, St_d=0.5, R=0.4.

i	$St_d(i)$	$C_D(i)$	$C_D'(i)$	$C_D''(i)$	$St_d(i+1)$
1	0.5000000	1.2217191	2.6025389	605965.71	0.4999982
2	0.4999982	1.2217913	2.6962855	-833828.27	0.4999995
3	0.4999995	1.2217905	2.6257032	-820994.65	0.5000008
4	0.5000008	1.2217819	-1.0735970	72485.06	0.5000067
5	0.5000067	1.2217777	-1.0882703	75426.62	0.5000125
6	0.5000125	1.2217736	-0.7111327	5.8167559	0.5489149
7	0.5489149	1.1868311	-0.6433922	3.3617930	0.6254683

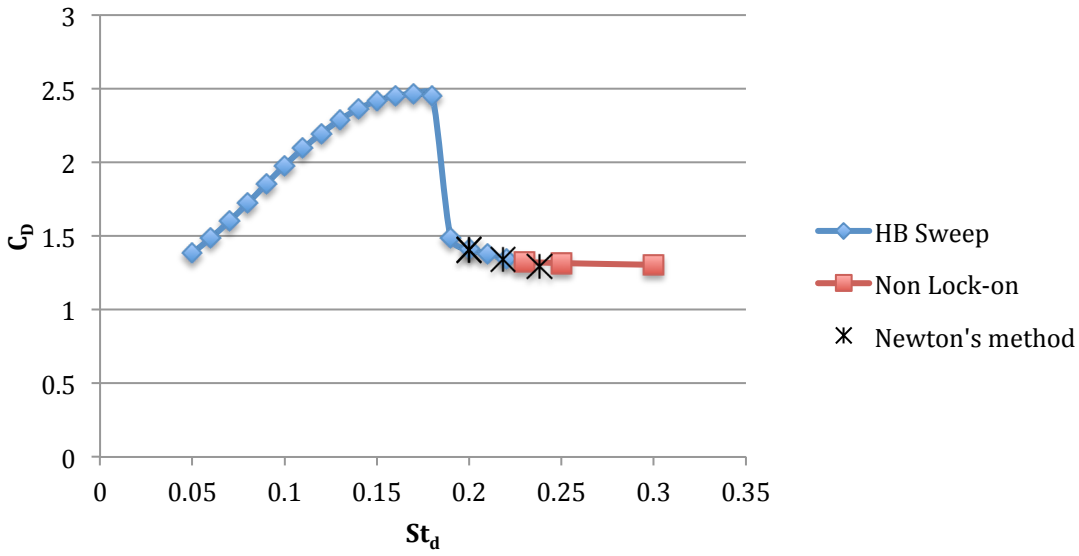

Figure 52: Comparison of Newton's method sensitivity analysis to frequency sweep. Re=100, Ω=1.2.

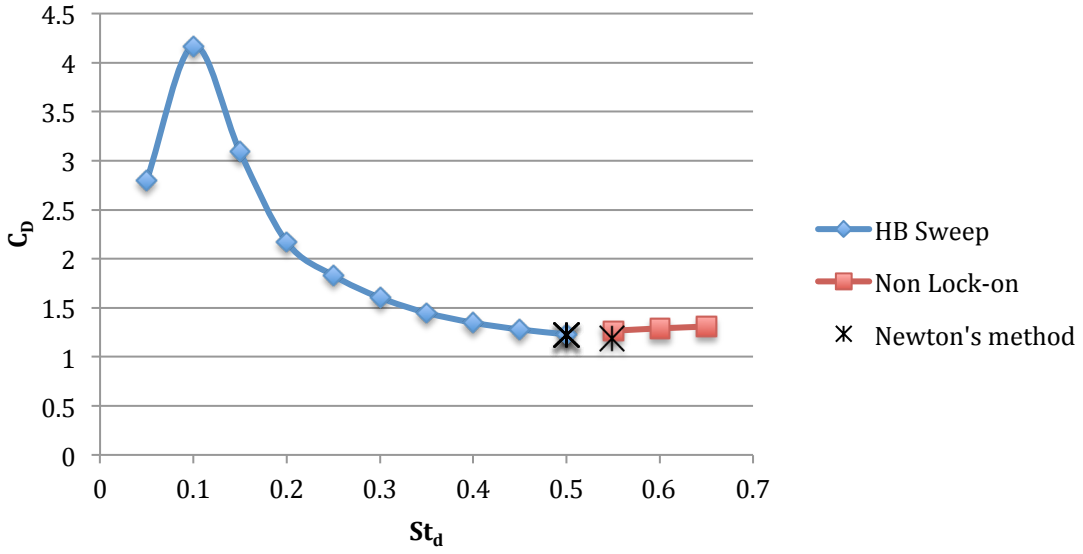

Figure 53: Comparison of Newton's method sensitivity analysis to frequency sweep. *Re*=100, Ω=3.0.

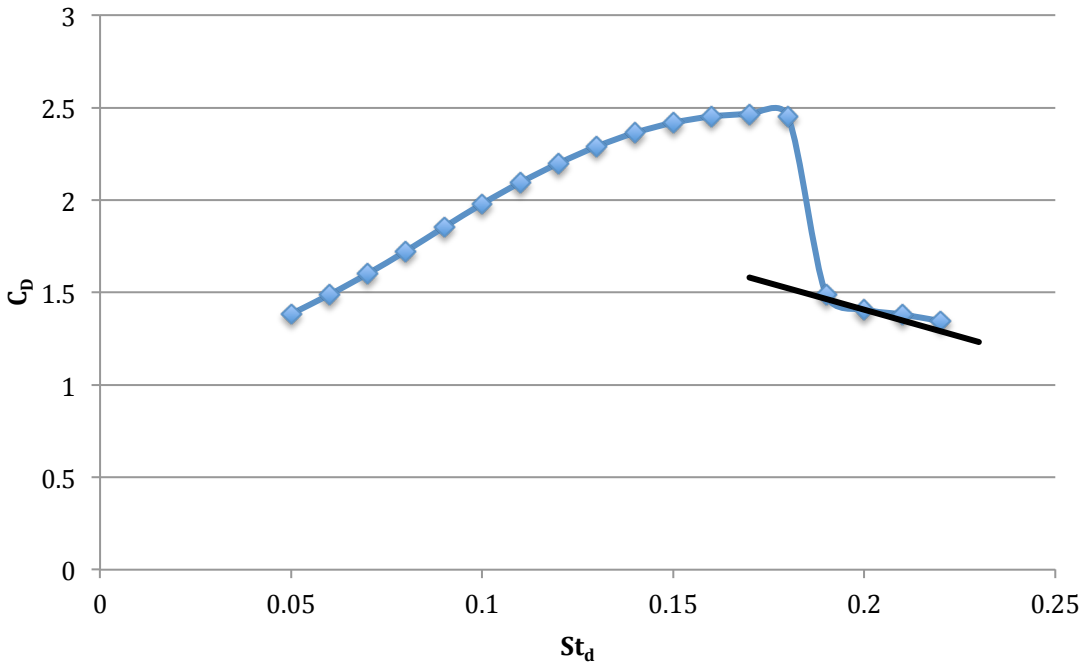

Figure 54: Slope from the first Newton's method iteration imposed on a sweep of mean drag coefficients in the lock-on region for Ω=1.2. (See Table 3).

4.3.2 Steepest Descent Approach

Tables 5 and 6 show the results of the sensitivity analysis using the Steepest Descent approach. Note the smaller relaxation values used for this approach as compared to those used in Section 4.3.1. The relaxation factor is necessary for this technique, and the solution is very sensitive to the selection of this value. A smaller relaxation factor will slow down the convergence, but a large relaxation factor will cause the solution to diverge. Tables 5 and 6 reveal the same trend as those in Section 4.3.1. Once again, the mean drag coefficient decreases with increasing Strouhal number, and there is a jump into the non lock-on region where the harmonic balance solution does not converge. This jump occurs very quickly for the lower rotation rate seen in Table 5. Table 6 shows that it takes many more iterations before the jump occurs for the higher rotation rate. Figures 55 and 56 show the Steepest Descent optimization results imposed on the sweeps for the two rotational rates considered. The jump into the non lock-on region is shown clearly in these figures.

The harmonic balance solver was validated using the experimental results of Thiria et al.[37] (See Section 4.2.2). These results are re-visited for a sensitivity analysis with the steepest descent approach. The Strouhal number was still used as the design variable, and the frequency ratios were determined using Eq. (89). Two sensitivity analysis runs were performed with different input frequency ratios. The first run took approximately three days to perform 8 iterations, while the second run took approximately half the time to perform 4 iterations. Figure 57 shows these results imposed on the experimental results of Thiria et al.[37] Fig. 57 reveals the accuracy of the sensitivity analysis. However, it was noted in Section 4.2.2 that the harmonic balance solver did not result in a local minimum near $f_f/f_0 \approx 3.5$. The mean drag coefficient continued to decrease for higher frequency ratios (see Fig. 44). This is consistent with the sensitivity results for $Re=100$.

Table 5: Sensitivity analysis using Steepest Descent with relaxation. Input parameters: Ω=1.2, St_d=0.2, R=0.01.

i	$St_d(i)$	$C_D(i)$	$C_D'(i)$	$St_d(i+1)$
1	0.2000000	1.4066794	1.1798754	0.1882012
2	0.1882012	1.4908582	-4.3371748	0.2315729
3	0.2315729	1.3061828	-2.2398071	0.2539710

Table 6: Sensitivity analysis using Steepest Descent with relaxation. Input parameters: Ω=3.0, St_d=0.5, R=0.01.

i	$St_d(i)$	$C_D(i)$	$C_D'(i)$	$St_d(i+1)$
1	0.5000000	1.229717	0.5262837	0.4947371
2	0.4947371	1.2349264	-0.9113841	0.5038510
3	0.5038510	1.2268018	-0.8639971	0.5124909
4	0.5124909	1.2199779	-0.8082558	0.5205735
5	0.5205735	1.2138357	-0.7688445	0.5282619
6	0.5282619	1.2082243	-0.7355727	0.5356177
7	0.5356177	1.2030528	-0.7064294	0.5426820
8	0.5426820	1.1982559	-0.6802085	0.5494840
9	0.5494840	1.1938244	-0.6563166	0.5560472

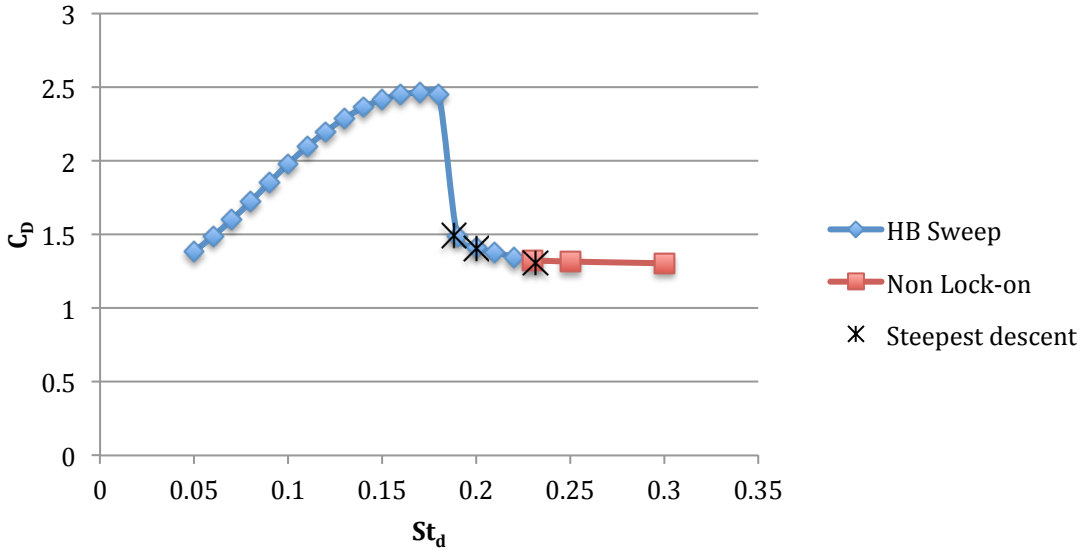

Figure 55: Comparison of Steepest Descent sensitivity analysis to frequency sweep. *Re*=100, *Ω*=1.2.

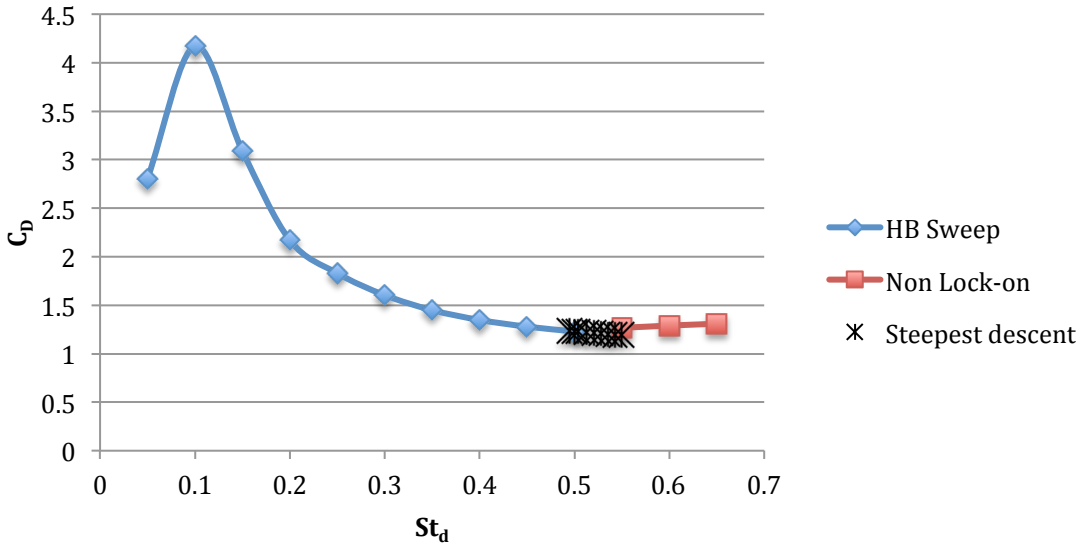

Figure 56: Comparison of Steepest Descent sensitivity analysis to frequency sweep. *Re*=100, *Ω*=3.0.

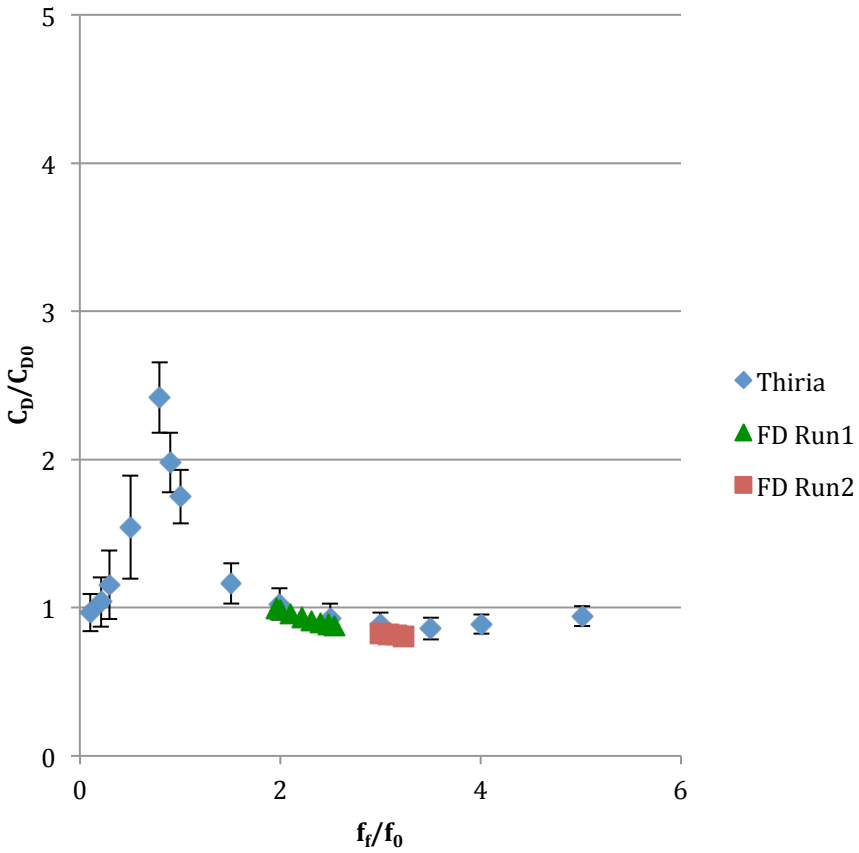

Figure 57: Comparison of Steepest Descent sensitivity analysis to the experimental results of Thiria et al.[37] *Re*=150. Ω=2.

The results from both iterative techniques reveal a limitation for sensitivity analysis using the harmonic balance solver. The drag coefficient values decrease with each successive iteration, but after some time the harmonic balance method is no longer useful. The harmonic balance solver is obviously limited to the lock-on region. On the other hand, it runs significantly faster than the time-accurate solver when it is valid. This sensitivity analysis took anywhere from overnight to multiple days, depending on the mesh size. Whereas a time-accurate solution would take at least a week as compared to a couple days.

Chapter 5: Conclusion

The flow over a circular cylinder was considered in this work. Both steady and unsteady flow were analyzed in which the cylinder was either stationary, in constant rotation or in periodic rotation. Three flow solvers were developed in this study including a steady solver, an unsteady time-accurate solver, and an unsteady harmonic balance solver. In all cases, the physical domain was transformed to a computational domain such that far-field conditions could be directly applied to the boundary. The transformed Navier-Stokes equations were solved using an implicit method, which lead to a nonlinear, coupled system of discrete governing equations. This nonlinear system was solved using Newton's method.

Even though steady solutions are not physical for $Re \geq 47$, their results provided good initial solutions for the unsteady flow solvers. Thus, the steady flow over a stationary cylinder was analyzed for higher Reynolds numbers. The solution of the steady cylinder revealed results that were consistent with the expectations of a stationary cylinder in steady flow. For each case investigated, two symmetric vortices were attached to the cylinder. The vortices grew in size as the Reynolds number was increased. The steady flow over a cylinder in constant rotation was also considered. This work revealed a linear relationship between the lift coefficient and the rotational parameter for low rotation rates.

The majority of this work was focused on the unsteady flow over a circular cylinder. Here, rotation was used as an active control for the unsteady flow with the goals of achieving lift enhancement, drag reduction, and the suppression of vortex shedding. The time-accurate solver was first used to investigate the flow over a cylinder in constant rotation. The temporal lift coefficient was investigated for multiple Reynolds numbers with a wide range of rotation rates. This force coefficient eventually became fully periodic for rotation rates beneath a critical value due to vortex shedding. The flow field arrived at a steady state for moderate rotation rates, and eventually returned to a periodic state for much higher rotation speeds. These results revealed a desirable characteristic for the flow over a cylinder in constant rotation. When the temporal lift coefficient reached a steady state, the vortex shedding was completely suppressed. This confirms that rotation can be

successfully used as an active control for the unsteady flow over a cylinder. Relatively large mean lift coefficients were also achieved for a cylinder in constant rotation via the Magnus effect. The present work saw an increase in the mean lift coefficient for increasing rotational speeds. Investigation of the mean drag coefficient revealed a drag reduction beneath the stationary value for all rotation rates considered for Re=200. However, the mean drag coefficient decreased with increasing rotation speeds up to a critical rotation rate for a Reynolds number of 100. Past this point, the mean drag coefficient increased beyond that of the stationary cylinder. This revealed a relationship between the goals of drag reduction and lift enhancement. There were no apparent trade-offs for the higher Reynolds number; in that case, the lift enhancement and drag reduction occurred concurrently for all rotation rates investigated. However, there was a trade-off for Re=100 past the critical rotation rate. Drag reduction and lift enhancement occurred simultaneously for rotation rates below the critical value. Past this value, both force coefficients increased with increasing rotational speeds. It is possible to achieve lift enhancement for rotation rates past the critical value, but this positive effect will be opposed by an increase in the drag coefficient.

The flow over a rotationally oscillating cylinder was also studied in this work. This temporally periodic flow was analyzed using both the time-accurate and the harmonic balance solver. The flow regime for a periodically rotating cylinder can be characterized into two regions: the lock-on region and the non lock-on region. The flow is considered to be in the lock-on region if the vortex-shedding frequency matches the imposed forcing frequency. If the frequencies do not align, then the flow is determined to be non-lock on. The two unsteady solvers were used to determine the flow regime for the rotationally oscillating cylinder, which slightly differed from previous works. A Fast Fourier Transform was performed on the temporal lift coefficient to reveal the frequencies of the flow field. The transform of a lock-on case resulted in only one frequency peak, while the non lock-on case revealed two distinct peaks. These two peaks corresponded to the vortex shedding frequency and the forcing frequency, which have not locked-on to each other. The harmonic balance method used in this work only converges for temporally periodic flows

with one fundamental frequency. Therefore, the harmonic balance solver was used to investigate rotationally oscillating cylinders in the lock-on region. The mean drag and lift coefficients were investigated with the objective of finding drag reduction and lift enhancement beyond that of the stationary value. Drag reduction was achieved for Re=150. While only a slight drag reduction was recorded for Re=100 for certain rotation rates. The minimum mean drag coefficient occurred either near the boundary of the lock-on region or in the non lock-on region. This limited the capabilities of determining a minimum average drag coefficient with the use of the harmonic balance solver. The distribution of the maximum lift coefficient was also considered. The results revealed an increase in the maximum lift coefficient with an increase in the rotation rate. As the forcing frequency was increased, a sharp decrease was noted near the natural vortex shedding frequency; the maximum lift coefficient continued to decrease past this point. This investigation into the force coefficients revealed a clear trade-off for the lift enhancement and drag reduction for a rotationally oscillating cylinder. The best frequencies for lift enhancement were those beneath the natural vortex shedding frequency. However, drag reduction beneath the stationary value was not observed for those frequencies. On the other hand, the drag reduction was greatest at the boundary between the lock-on and non lock-on regions, which corresponds with the lowest maximum lift coefficient.

Lastly, a finite difference sensitivity analysis was performed for the periodic case using the harmonic balance solver. In this work, the drag coefficient was chosen as the objective function, and the Strouhal number was the designated design variable. The goal was to use the sensitivity analysis to determine a value of the Strouhal number that yielded a minimum mean drag coefficient. The sensitivity analysis was performed with two iterative methods, but neither method converged to a minimum drag coefficient with the harmonic balance solver. While the sensitivity analysis was approaching a minimum, it eventually lead to a Strouhal number in the non lock-on region at which point the harmonic balance solver was no longer useful. The limitations were clear for the harmonic balance solver. However, it ran significantly faster than the time-accurate solver when it was valid.

A similar sensitivity analysis with the time-accurate solver may have minimized the drag coefficient, but it would have taken a notably longer time to do so.

List of References

[1]White, F. M., *Fluid Mechanics*, 6th ed., McGraw-Hill, Boston, 2008.

[2]White, F. M., *Viscous Fluid Flow*, 3rd ed., McGraw-Hill, Boston, 2006.

[3]Kang, S., Choi, H., and Lee, S., "Laminar flow past a rotating circular cylinder," *Physics of Fluids*, Vol. 11, No. 11, 1999, pp. 3312-3321.

[4]Choi, S., Choi, H., and Kang, S., "Characteristics of flow over a rotationally oscillating cylinder in low Reynolds number," *Physics of Fluids*, Vol. 14, No. 8, 2002, pp. 2767-2777.

[5]Homescu, C., Navon, I. M., and Li, Z., "Suppression of vortex shedding for flow around a circular cylinder using optimal control," *International Journal for Numerical Methods in Fluids*, Vol. 38, 2002, pp. 43-69.

[6]Stojkovic, D., Breuer, M., and Durst, F., "Effect of high rotation rates on the laminar flow around a circular cylinder," *Physics of Fluids*, Vol. 14, No. 9, 2002, pp. 3160-3178.

[7]Ingham, D. B., and Tang, T., "A Numerical Investigation into the Steady Flow Past a Rotating Circular Cylinder at Low and Intermediate Reynolds Numbers," *Journal of Computational Physics*, Vol. 87, 1990, pp. 91-107.

[8]Badr, H. M., Dennis, S. C. R., and Young, P. J. S., "Steady and Unsteady Flow Past a Rotating Circular Cylinder at Low Reynolds Numbers," *Computers & Fluids*, Vol. 17, No. 4, 1989, pp. 579-609.

[9]Mittal, S., and Kumar, B., "Flow past a rotating cylinder," *Journal of Fluid Mechanics*, Vol. 476, 2003, pp. 303-334.

[10]Taneda, S., "Visual Observations of the Flow past a Circular Cylinder Performing a Rotatory Oscillation," *Journal of the Physical Society of Japan*, Vol. 45, No. 3, 1978, pp. 1038-1043.

[11]Tokumaru, P. T., and Dimotakis, P. E., "Rotary oscillation control of a cylinder wake," *Journal of Fluid Mechanics*, Vol. 224, 1991, pp. 77-90.

[12]Shiels, D., and Leonard, A., "Investigation of a drag reduction on a circular cylinder in rotary oscillation," *Journal of Fluid Mechanics*, Vol. 431, 2001, pp. 297-322.

[13]Cheng, M., Liu, G. R., and Lam, K. Y., "Numerical simulation of flow past a rotationally oscillating cylinder," *Computers & Fluids*, Vol. 30, 2001, pp. 365-392.

[14]Baek, S. and Sung, H. J., "Numerical simulation of the flow behind a rotary oscillating circular cylinder," *Physics of Fluids*, Vol. 10, No. 4, 1998, pp. 869-876.

[15]Ekici, K., and Hall, K. C., "Nonlinear Analysis of Unsteady Flows in Multistage Turbomachines Using the Harmonic Balance Technique," *44th AIAA Aerospace Sciences Meeting and Exhibit, Reno, NV, January 2006,* AIAA Paper 2006-422, 2006.

[16]Hall, K.C., Thomas, J.P., and Clark, W.S., "Computation of Unsteady Nonlinear Flows in Cascades Using a Harmonic Balance Technique," *AIAA Journal*, Vol. 40, No. 5, 2002, pp. 879-886.

[17]Ekici, K., and Beran, P., "Adjoint Sensitivity Analysis of Low-speed Flows Using an Efficient Harmonic Balance Technique," *42nd AIAA Fluid Dynamics Conference and Exhibit, New Orleans, LA, June 2012,* AIAA Paper 2012-2697, 2012.

[18]Huang, H., and Ekici, K., "A Harmonic Balance Method for the Analysis of Unsteady Flows in Cascades," *47th AIAA/ASME/SAE/ASEE Joint Propulsion Conference & Exhibit, San Diego, CA, July-August 2011*, AIAA Paper 2011-5752, 2011.

[19]Hoffman, J. D., *Numerical Methods for Engineers and Scientists*, 2nd ed., Marcel Dekker, Inc., New York, 2001.

[20]Fornberg, B., "Steady Viscous Flow Past a Circular Cylinder up to Reynolds Number 600," *Journal of Computational Physics*, Vol. 61, 1985, pp. 297-320.

[21]Fornberg, B., "A numerical study of steady viscous flow past a circular cylinder," *Journal of Fluid Mechanics*, Vol. 98, No. 4, 1980, pp.819-855.

[22]Filon, L. N. G., "The Forces on a Cylinder in a Stream of Viscous Fluid," *Proceedings of the Royal Society A*, Vol. 113, No. 763, 1926, pp. 7-27.

[23]Ekici, K., Hall, K. C., and Dowell, E. H., "Computationally Fast Harmonic Balance Methods for Unsteady Aerodynamic Predictions of Helicopter Rotors," *Journal of Computational Physics*, Vol. 227, No. 12, 2008, pp. 6206-6225.

[24]Beran, P., Stanford, B., and Kurdi, M., "Sensitivity Analysis for Optimization of Dynamic Systems with Reduced Order Modeling," *48th AIAA Aerospace Sciences Meeting Including the New Horizons Forum and Aerospace Exposition, Orlando, FL, January 2010,* AIAA Paper 2010-1503, 2010.

[25]Woodgate, M. A., and Barakos, G. N., "Implicit Computational Fluid Dynamics Methods for Fast Analysis of Rotor Flows," *AIAA Journal*, Vol. 50, No. 6, 2012, pp. 1217-1244.

[26]Thomas, J. P., Custer, C. H., Dowell, E. H., and Hall, K. C., "Unsteady Flow Computation Using a Harmonic Balance Approach Implemented about the OVERFLOW 2 Flow Solver," *19th AIAA Computational Fluid Dynamics Conference, San Antonio, TX, June 2009,* AIAA Paper 2009-4270, 2009.

[27]Müller, J. D., and Cusdin, P., "On the performance of discrete adjoint CFD codes using automatic differentiation," *International Journal for Numerical Methods in Fluids*, Vol. 47, 2005, pp. 939-945.

[28]Kirsch, U. "Efficient sensitivity analysis for structural optimization," *Computer Methods in Applied Mechanics and Engineering*, Vol. 117, 1994, pp. 143-156.

[29]Figliola, R. S., and Beasley, D. E., *Theory and Design for Mechanical Measurements*, 4th ed., Wiley, Hoboken, NJ, 2006.

[30]Tang, T., and Ingham, D. B., "On Steady Flow Past a Rotating Circular Cylinder at Reynolds Numbers 60 and 100," *Computers & Fluids*, Vol. 19, No. 2, 1991, pp. 217-230.

[31]Seifert, J., "A review of the Magnus effect in aeronautics," *Progress in Aerospace Sciences*, Vol. 55, 2012, pp. 17-45.

[32]Prandtl, L., "Application of the 'Magnus Effect' to the wind propulsion of ships," *Naturwissenschaften*, Vol. 13, 1925.

[33]Tokumaru, P. T., and Dimotakis, P. E., "The lift of a cylinder executing rotary motions in a uniform flow," *Journal of Fluid Mechanics*, Vol. 225, 1993, pp. 1-10.

[34]Goldstein, S., *Modern developments in fluid dynamics*, Oxford Press, London, 1938.

[35]Glauert, M.B., "The flow past a rapidly rotating circular cylinder," *Proceedings of the Royal Society of London. Series A, Mathematical and Physical Sciences*, Vol. 242, No. 1228, 1957, pp. 108-115.

[36]Protas, B., and Wedfried, J. E., "Drag force in the open-loop control of the cylinder wake in the laminar regime," *Physics of Fluids*, Vol. 14, No. 2, 2002, pp. 810-826.

[37]Thiria, B., Goujon-Durand, S., and Wesfried, J. E., "The wake of a cylinder performing rotary oscillations," *Jounral of Fluid Mechanics*, Vol. 560, 2006, pp. 123-147.

[38]Lu, X., "Numerical Study of the Flow Behind a Rotary Oscillating Circular Cylinder," *International Journal of Computational Fluid Dynamics*, Vol. 16, No. 1, 2002, pp. 65-82.

Vita

Emily Buckman earned a Bachelor's of Science degree in Aerospace Engineering from the University of Tennessee, Knoxville in May 2011. In this year, she was awarded the Herman Morris Scholarship as the top Aerospace student in the graduating class and graduated with Summa Cum Laude honors. She also earned a position in the Volkswagen Distinguished Scholars Program, in which she completed combustion research at Oak Ridge National Laboratory in the summer of 2011. She went on to earn a Master's of Science degree in Aerospace Engineering at the University of Tennessee, Knoxville. While earning this degree, she worked under the direction of Dr. Kivanc Ekici and completed diverse research at Wright Patterson Air Force Base and Oak Ridge National Laboratory. Emily worked as a Graduate Teaching Assistant at the University of Tennessee, Knoxville, where she found an interest in mentoring undergraduate students and was given the opportunity to instruct a course during the summer of 2013. Emily was married to Mr. John Clark in May 2013. She will continue her graduate education with the pursuit of a Ph.D. in Energy Science and Engineering as a Bredesen Center Fellow at the University of Tennessee, Knoxville.